A Multimodal Adaptive Optical Microscope For *In Vivo* Imaging from Molecules to Organisms

Tian-Ming Fu[1a†], Gaoxiang Liu[2†], Daniel E. Milkie[1†], Xiongtao Ruan[2†], Frederik Görlitz[2], Yu Shi[3b], Valentina Ferro[2], Nikita S. Divekar[2], Wei Wang[4], Harrison M. York[5], Velat Kilic[1], Matthew Mueller[1,2], Yajie Liang[6], Timothy A. Daugird[7e], Maria J. Gacha-Garay[8], Kathryn A. Larkin[8], Rebecca C. Adikes[8c], Nathaniel Harrison[2], Cyna Shirazinejad[2,9], Samara Williams[2], Jamison L. Nourse[10], Shu-Hsien Sheu[1d], Liang Gao[1], Tongchao Li[11f], Chandrani Mondal[16], Kemal Achour[2], Wilmene Hercule[2], Daniel Stabley[12], Kevin Emmerich[13,14], Peng Dong[1g], David Drubin[2], Zhe J. Liu[1], David Clapham[1], Jeff S. Mumm[13,14], Minoru Koyama[15], Alison Killilea[2], Jose Javier Bravo-Cordero[16], C. Dirk Keene[17], Liqun Luo[11], Tom Kirchhausen[18,19,20], Medha M. Pathak[10,21], Senthil Arumugam[5,22], James K. Nunez[2], Ruixuan Gao[4,23], David Q. Matus[8i], Benjamin L. Martin[8], Ian A. Swinburne[2], Eric Betzig[1,2,24]*, Wesley R. Legant[3,7]*, Srigokul Upadhyayula[2,25,26]*

† These authors contributed equally
* Corresponding authors: betzige@janelia.hhmi.org, legantw@email.unc.edu, sup@berkeley.edu

1 Janelia Research Campus, Howard Hughes Medical Institute, Ashburn, VA, 20147, USA
2 Department of Molecular and Cell Biology, University of California, Berkeley, Berkeley, CA, 94720, USA
3 Lampe Joint Department of Biomedical Engineering, University of North Carolina at Chapel Hill, Chapel Hill, NC, USA
4 Department of Chemistry, University of Illinois Chicago; Chicago, IL 60607, USA
5 Monash Biomedicine Discovery Institute, Faculty of Medicine, Nursing and Health Sciences, Monash University, Clayton/Melbourne, VIC, 3800, Australia
6 Department of Diagnostic Radiology and Nuclear Medicine, University of Maryland School of Medicine, Baltimore, MD 21201, USA
7 Department of Pharmacology, University of North Carolina at Chapel Hill, Chapel Hill, NC, USA
8 Department of Biochemistry and Cell Biology, Stony Brook University, Stony Brook, NY, 11794-5215, USA
9 Biophysics Graduate Group, University of California, Berkeley, Berkeley, CA, USA
10 Department of Physiology and Biophysics, Sue and Bill Gross Stem Cell Research Center, University of California Irvine, Irvine 92697, USA
11 Department of Biology, Howard Hughes Medical Institute, Stanford University, Stanford, United States
12 Neuroimaging Laboratory, Department of Developmental Neurobiology, St. Jude Children's Research Hospital, 262 Danny Thomas Place, Memphis, TN, 38105, USA
13 Wilmer Eye Institute and the Department of Ophthalmology, Johns Hopkins University School of Medicine, Baltimore, MD 21287, USA
14 McKusick-Nathans Institute and the Department of Genetic Medicine, Johns Hopkins University School of Medicine, Baltimore, MD 21287, USA
15 University of Toronto, Department of Cell and Systems Biology, Scarborough, Ontario, Canada
16 Department of Medicine, Division of Hematology and Oncology, The Tisch Cancer Institute, Icahn School of Medicine at Mount Sinai, New York, NY 10029, USA
17 University of Washington BioRepository and Integrated Neuropathology (BRaIN) lab, Harborview Medical Center, Seattle, WA, USA
18 Program in Cellular and Molecular Medicine, Boston Children's Hospital, Boston, MA 02115
19 Department of Pediatrics, Harvard Medical School, Boston, MA 02115
20 Department of Cell Biology, Harvard Medical School, Boston, MA 02115

21 Department of Biomedical Engineering, and Center for Complex Systems Biology, University of California, Irvine, CA 92697 University of California, Irvine, Irvine 92697, USA
22 European Molecular Laboratory Australia, Monash University, Clayton/ Melbourne, VIC 3800, Australia
23 Department of Biological Sciences, University of Illinois Chicago, Chicago, IL 60607, USA
24 Department of Physics, Howard Hughes Medical Institute, Helen Wills Neuroscience Institute, University of California, Berkeley, Berkeley, CA 94720, USA.
25 Molecular Biophysics and Integrated Bioimaging Division, Lawrence Berkeley National Laboratory, Berkeley, CA 94720, USA
26 Chan Zuckerberg Biohub, San Francisco, CA 94158, USA

a Present address: Department of Electrical and Computer Engineering, and Omenn Darling Bioengineering Institute, Princeton University, Princeton, NJ, USA
b Present address: Department of Physics and Astronomy, Western University, London, Ontario, Canada
c Present address: Department of Biology, Siena College, Loudonville NY, USA
d Present address: Chan Zuckerberg Imaging Institute, Redwood City, CA 94065, USA
e Present address: Department of Genetics, University of North Carolina at Chapel Hill, Chapel Hill, NC, USA
f Present address: Liangzhu Laboratory, MOE Frontier Science Center for Brain Science and Brain-machine Integration, State Key Laboratory of Brain-machine Intelligence, Zhejiang University, Hangzhou, China
g Present address: Institute of Biomedical and Health Engineering, Shenzhen Institutes of Advanced Technology, Chinese Academy of Sciences, Shenzhen, China
h Present address: Institute of Biomedical and Health Engineering, Shenzhen Institutes of Advanced Technology, Chinese Academy of Sciences, Shenzhen, China
i Present address: Department of Molecular and Cell Biology, University of California, Berkeley, Berkeley, CA, US

Abstract:
Understanding biological systems requires observing features and processes across vast spatial and temporal scales, spanning nanometers to centimeters and milliseconds to days, often using multiple imaging modalities within complex native microenvironments. Yet, achieving this comprehensive view is challenging because microscopes optimized for specific tasks typically lack versatility due to inherent optical and sample handling trade-offs, and frequently suffer performance degradation from sample-induced optical aberrations in multicellular contexts. Here, we present MOSAIC, a reconfigurable microscope that integrates multiple advanced imaging techniques including light-sheet, label-free, super-resolution, and multi-photon, all equipped with adaptive optics. MOSAIC enables non-invasive imaging of subcellular dynamics in both cultured cells and live multicellular organisms, nanoscale mapping of molecular architectures across millimeter-scale expanded tissues, and structural/functional neural imaging within live mice. MOSAIC facilitates correlative studies across biological scales within the same specimen, providing an integrated platform for broad biological investigation.

Main:

Light microscopy has shaped our view of how life works since scientists first began observing cells through a lens – revealing processes from single molecule kinetics to *in toto* organismal development in model systems ranging from cultured cell lines to organoids, *C. elegans*, *Drosophila*, zebrafish, and mice. Historically, this diversity drove the development of distinct microscope modalities, including widefield, confocal, light sheet, and two-photon microscopy, each optimized to meet specific needs[1,2]. Super-resolution variants[3,4] of these have further expanded the range and power of optical microscopy.

However, optimization for one modality or one class of samples invariably comes with constraints that compromise the study of other systems. These constraints encompass not only optical characteristics such as field-of-view (FOV) and resolution, but also practical considerations such as sample mounting and environmental control. For example, high numerical aperture (NA) objectives optimize spatial resolution, but sacrifice FOV and working distance. Light sheet microscopes enable low-phototoxicity volumetric imaging, but can require non-traditional mounting arrangements or complex relay optics in inverted systems[5]. Two-photon point scanning increases imaging depth, but often sacrifices speed and broad multicolor capabilitiy[6,7]. As such, a modern imaging core or well-equipped microscopy lab often supports several different instruments tailored to different tasks, multiplying cost and operational complexity. Furthermore, nearly all commercial microscopes that are the backbone of imaging cores ignore the “elephant in the room” that is sample-induced optical aberrations that quickly compromise performance in multicellular applications.

To address these issues, we developed the Multimodal Optical Scope with Adaptive Imaging Correction (MOSAIC), a single microscope that reconfigures on demand to different imaging modalities, each optimized for a different class of specimens. We demonstrate MOSAIC across a broad range of biological systems and spatiotemporal scales, including single molecule tracking in live adherent cells, organelle remodeling in both isolated cells and developing organisms, quantifying neural activity at single spine resolution in the cortex of live mice, and mapping neuronal ultrastructure across millimeters of cleared tissue. Collectively, these applications highlight MOSAIC’s ability to switch seamlessly between oblique transmitted light illumination for label-free contrast, widefield epifluorescence imaging, 3D structured illumination microscopy (SIM), lattice light sheet microscopy (LLSM), LLS-SIM, image scanning microscopy (ISM), and two-photon point scanning microscopy for *in vivo* imaging. Notably, all modes can apply adaptive optical (AO) direct wavefront sensing[8] correction to counter sample-induced aberrations and ensure optimal performance at depth. By reusing the same hardware and software across modes, MOSAIC reduces the overall cost and minimizes the spatial footprint relative to acquiring multiple separate instruments. It also enables quantitative comparisons of different imaging methods on the same biological sample and opens new doors for adaptive imaging protocols that demand dynamically switching between modalities.

Results:

Microscope design and characterization

MOSAIC was conceptualized as an evolution of the LLSM design incorporating two-channel AO correction (AOLLSM)[9]. The original instrument used a 0.65 NA excitation lens and 1.1 NA detection lens along with a 0.8 NA epifluorescence objective to view the sample from below. While this arrangement optimized 3D spatial resolution, it also placed severe constraints on working distance and specimen geometries, typically limiting samples to a 5 mm diameter coverslip positioned between the objectives. For MOSAIC, we opted for 0.6 NA excitation, a 1.0 NA detection, and a coverslip-corrected 1.0 NA inverted epifluorescence objective (Fig. S1a). While entailing a modest reduction in resolution, these choices increase the effective working distance between the light sheet objectives and the coverslip from near zero to 330 μm (Fig. S1a), thereby accommodating 25-mm diameter coverslips for specimen mounting with an unobstructed scan range across its entire area. The two 1.0 NA detection objectives enable high-resolution, millimeter-scale FOV investigations across a variety of imaging modes (Fig. S1b-e, Fig. S2, S3, S4). All three objectives and the specimen are housed within an environmental chamber with full control over temperature, perfusion, and CO_2. A fourth objective, also of 1.0 NA, resides in an upright station within MOSAIC for two-photon imaging of larger specimens such as live mice (Fig S1f).

To maximize the excitation power needed for large FOV and fast light sheet imaging, MOSAIC uses a Powell / cylindrical lens combination (Fig. S2a), concentrating laser power onto the long, narrow region of the spatial light modulator (SLM) to which the LLS pattern is written. Any combination of seven visible lasers can be used simultaneously, since we first split their post-Powell lens overlapping light sheets with a stack of parallel dichroic mirrors into seven independent parallel stripes on the SLM (Fig. S5a). This facilitates independent phase pattern control of light sheet tip, tilt, and AO correction for each laser. After reflection off the SLM, the seven colors return through the same dichroic stack, recombining into an overlapped, colinear multicolor beam (Fig. S5a,b) that reflects off a sample-conjugate resonant galvo (to reduce sample-induced shadowing artifacts[9]) and two pupil conjugate galvos (for LLS axial alignment and lateral dither) before entering the excitation objective (Fig. S2a). The resulting volumetric FOV (without tiling) for LLSM increases from 100 × ~30 × 100 μm^3 in the prior implementation to 200 × ~30 × 20,000 μm^3 in MOSAIC, and the imaging speed is more than doubled by the focused excitation and the use of two cameras (Fig. S2b, S6b) for simultaneous two-color imaging.

AOLLSM requires a substantial investment in hardware (e.g., objectives, lasers, galvos, SLM, deformable mirror (DM), control electronics, sample stages, and cameras). MOSAIC extracts maximal value from this investment by repurposing these components as needed for multiple imaging modes, all with AO correction: LLSM and LLS-SIM (Fig. S2a,b, Fig. S6b), oblique transmitted light illumination (Fig. S2c, Fig. S6c), widefield and 3D structured illumination microscopy (Fig. S2d, Fig. S6d), image scanning microscopy (Fig. S3a, Fig S6e), two-photon Bessel beam light sheet (Fig. S3c, Fig S7a,b), two-photon point scanning microscopy (Fig. S4a, Fig. S7d, in both inverted and upright configurations), and point scanning photostimulation (Fig. S4b, Fig. S7f). Optical toggles (Fig. S5c) reconfigure the light path between modes in 2-5 sec or reconfigure the imaging cameras as wavefront sensors during wavefront measurement. The entire instrument, including lasers, fits within a 1 × 1 × 1 m^3 volume, promoting alignment stability

(Movie S1). Pre-centered mirrors and lenses with no adjustment (Fig. S5d) simplify assembly and alignment of MOSAIC by eliminating unnecessary degrees of freedom, further contributing to stability. Characterizations of the optical path as well as the experimentally measured point spread function (PSF), and optical transfer function (OTF) for each mode are provided in Figures S2, S3, S4, and S8.

Long-term multimodal imaging of cultured cell growth over vast fields of view

Even clonal populations of cultured cells exhibit considerable structural and functional heterogeneity[10]. A more comprehensive understanding of such cells requires mapping their phenotypic diversity by imaging many cells over multiple rounds of division within a single experiment. Using MOSAIC and the non-invasiveness of LLSM, we volumetrically imaged a ~1 mm × 0.75 mm field of LLC-PK1 cells stably expressing markers for the endoplasmic reticulum (ER) and nucleus at ~260 x 260 x 431 nm nominal resolution every 90 sec over ~24 hrs (984 time points, Fig. 1a,b, Movie S2). The entire 49 TB data set, which contains ~1.5 million nuclear image volumes (Fig. S9a), was acquired at a sustained rate of 4 TB/hr and processed by PetaKit5D[11].

Movie S2 shows that the cellular population plateaued upon reached confluency ~12 hours from initial imaging (Fig. S9b), after which patches of cells exhibited occasional tissue-like behaviors such as epithelial detachment (Fig. 1a, xzMIP, white box inset) and reattachment. While the great majority of mitotic events followed the archetypal pattern (Fig. 1b, middle), we also identified atypical events such as a dividing cell with a large apical ER extrusion (Fig. 1b, left), and an example of tripolar mitosis. Such divisions have been observed previously[11,12], but MOSAIC offers a more detailed 4D view of this process, and its non-invasiveness enabled us to study the daughter cells through to their ultimate apoptosis (Fig. 1B, right, cyan arrows). As seen in this example, the vast spatiotemporal range covered by MOSAIC (<10 ms to 24 hrs and 260 nm to 1 mm, or 10^7 in time and 10^8 in volume) enables quantitative measurement of normal phenotypic distributions of structure and dynamics across large cellular populations as well as identification and detailed investigation of potentially important outliers from such distributions.

To provide global cellular context complementary to the protein-specificity of fluorescence, MOSAIC incorporates label-free oblique illumination (OI). Uniform laser illumination of the sample-conjugate SLM creates point excitation at the rear pupil of the excitation objective. Steering this point successively inward from the pupil edge creates widefield illumination intersecting the specimen at an angle relative to the collection cone of the inverted objective (Fig. S1c, Fig. S10a,b) that initially enters, then is tangent to, and finally misses the cone - conditions that produce brightfield, DIC-mimicking oblique, or darkfield images, respectively (Fig. S10c). Imaging speed and FOV is only camera-limited, producing 2D movies over ~200 x 200 μm^2 at up to 100 Hz, ideal for monitoring highly dynamic events like membrane ruffling and host-pathogen interactions (Fig. 1c, Movie S3A). Tiled acquisition enables studies over even larger FOVs, such as the migration and mitosis of cultured U2OS cells over a 1.218 × 0.975 mm^2 at 1 Hz for ~17 mins (1,000 time points, Fig. 1d, Movie S3B). Global contrast over such broad areas provides simple assessment of overall sample health and identification of specific events for further investigation by other imaging modalities.

Multimodal observation and optogenetic perturbation

MOSAIC permits interleaved LLSM and OI imaging in the same acquisition sequence, providing correlative 3D fluorescence and 2D label-free data from the same specimen (Fig. S11, S12, Movie S4). At the single cell level, we used this correlative approach to reveal 3D mitochondrial remodeling via LLSM at 56 sec intervals over 2 hrs in the context of more rapid changes in the plasma membrane and shape of a hTERT-RPE1 cell (Fig. S11, Movie S4A). Over a much larger FOV, we captured unlabeled intracellular events together with the 4D dynamics of the ER and Golgi apparatus for 2000 time points at 16.3 sec intervals (9 hrs total) through two color LLSM (Fig. S12, Movie S4B).

MOSAIC also incorporates point scanned excitation through any of its three objectives for targeted optogenetic stimulation of the specimen (Fig. S4b). To demonstrate, we induced localized actin polymerization, membrane ruffling, and macropinosome engulfment[13–16] in hTERT-RPE1 cells transiently expressing photoactivatable Rac1 (PA-Rac1 mCherry)[17] by raster-scanning 445 nm light through the inverted objective over a region of interest for 30 sec per frame (Fig. S13a,b, Movie S5). Interleaving photoactivation with OI imaging allowed us to observe the induced subcellular dynamics within each activated region (Fig S13c).

Multimodal live cell super-resolution microscopy

MOSAIC incorporates several forms of super-resolution (SR) microscopy to cover the tradeoffs between resolution, speed, and phototoxicity: single molecule tracking (SPT) and localization microscopy (SMLM); image scanning microscopy (ISM); and structured illumination microscopy (SIM). To demonstrate, we first combined LLSM with SPT and measured the kinetics of SOX2 transcription factor molecules labeled with PA-JF646 across a field nuclei of mouse embryonic stem cells at a median precision of 24.6 ± 4.3 nm and speed of 50 Hz (Fig. 2a). Trajectory analysis and fitting to an anomalous diffusion model yielded a distribution well described by a two-component Gaussian mixture model with diffusion coefficients and relative populations between the “DNA bound” and “freely diffusing“ states consistent with previous findings[18].

Trading resolution for speed and non-invasiveness, MOSAIC can combine LLSM and SIM, extending resolution in the laterally structured direction of the light sheet from 260 nm to ~180 nm (Fig. S8)[19]. With this modality we imaged the 4D dynamics of the ER and Golgi in cultured hTERT-RPE1 cells over a 50 x 188 x 10 μm^3 FOV every 10 seconds or 11 x 188 x 10 μm^3 FOV every 2 seconds for 1,500 timepoints with minimal photobleaching. The speed, resolution, and duration of this imaging allowed us to observe the continuous extension and retraction of individual ER tubules, an ER tunnel passing through the cell nucleus, and the intercalation and migration of fragmented Golgi compartments within the 3D ER network (Figs. 2b, S14, and Movie S6).

For live imaging with 2x resolution extension in all three dimensions, MOSAIC offers widefield 3D SIM through the inverted objective. We first demonstrated this mode by imaging mitochondrial and Golgi 4D dynamics in hTERT-RPE1 cells across a 160 x 100 x 10 μm^3 FOV at 57 sec intervals for 70 time points (Fig 2c, Movie S7A, Fig. S15). To achieve both faster and longer imaging, we then reduced the number of raw images in 3D SIM reconstruction from 15 in three directions to 10 in two directions and used computational denoising[20] (Fig S16) to maintain accurate

reconstructions at lower SNR. This enabled prolonged (10.7 hr) observation of mitochondrial events such as fission, fusion, active transport, and clustering, for 1200 time points at 32 sec intervals (Fig. S17a, Movie S7b) across a mixed field of quiescent, mitotic (Fig. S17b), and migrating (Fig. S17c) cells.

While the inclusion of SPT, LLS-SIM, and widefield 3D SIM gives the user flexibility to choose among the tradeoffs in live SR imaging (e.g., Movie S8, part 1), MOSAIC also allows them to be used in concert or with other modes in interleaved form. To demonstrate, we imaged a dividing hTERT-RPE1 cell labeled for mitochondria and Golgi. Every 3 minutes, we acquired 1,000 OI images, 20 LLSM volumes, and 1 volume each of LLS-SIM and 3D-SIM (Fig 2e, Movie S8, part 2). This correlative protocol captures different perspectives of the same event across multiple spatial and temporal scales.

Structural 3D SR imaging over large fields of view

The stability, large FOV, and 25 mm xy scan range of MOSAIC, coupled to GPU-accelerated analysis pipelines such as PetaKit5D, facilitate 3D rapid SR structural imaging over large volumes. Applied to two-color 3D LLSM-PAINT[21], we simultaneously imaged the nuclear envelope (specifically, Lamin A/C) and the mitochondrial outer membrane (TOMM20) with DNA probes[22] conjugated to Cy3B and ATTO655 respectively, at median localization precisions of 16 and 23 nm laterally and 136 and 178 nm vertically, over a 180 x 200 x 17 μm^3 volume (Fig. 3a, Movie S9). The volume was sufficiently large to catch the unusual morphology of a mitochondrion extending through a tubular invagination of the nuclear envelope (Fig. 3a, right).

Much larger samples, including tissues, can be imaged in 3D at lower but still nanoscale, resolution with expansion microscopy (ExM)[23]. Using LLSM [24], we imaged immunostained myelin sheaths (myelin basic protein (MBP)) and axons (neurofilament-200 (NF-200)) at 4x expansion across a 2000 x 2400 x 100 μm^3 section (pre-expansion) of human hippocampal brain tissue excised from a 90-year-old Alzheimer's disease (AD) patient (Fig. 3b-f, Movie S10). The aforementioned innovations of the combined MOSAIC / PetaKit5D platform allowed us to capture this 37 TB data set in 8.3 hrs, approaching the peak acquisition speed of modern sCMOS cameras. The data revealed numerous examples of aging pathologies (Fig. 3c-f) such as clusters of dystrophic neurites, characterized by significant localized "ballooning" of the myelin sheath[25], resembling previous observations in aged macaques[26]. These varicosities exhibited distended neurofilaments, potentially representing axons delaminated from the surrounding myelin, which in turn appeared torn or shredded (Fig. 3d). In another region, we observed large punctate clusters of NF-200 consistent with Wallerian-like axonal degeneration (Fig. 3e)[27]. These may represent residual debris after immune-provoked phagocytosis of axons by microglia or oligodendrocyte precursor cells (Fig. 3f)[28–30]. Notably, the large physical separation between these two pathologies emphasizes the value of rapidly imaging mm-scale swathes of tissue to comprehensively explore the diverse morphologies hidden within them.

Adaptive optical LLSM in living organisms

The cellular phenotypes we observe are the result of gene expression, which is regulated in part by external environmental cues. Therefore, we can only fully trust the physiological relevance of

our observations when we image cells natively embedded within the organism in which they evolved. The challenge then is that sample-induced optical aberrations varying in space and time across the organism degrade image resolution and signal. In MOSAIC, we correct these with direct wavefront sensing adaptive optics (AO)[8].

AO as applied to LLSM[9] requires independent correction for the orthogonal excitation and detection pathways. However, once implemented, it delivers high resolution 4D movies of dynamic subcellular processes in transparent organisms such as zebrafish embryos (Fig. 4). For example, over a FOV sufficiently small that a single pair of excitation and detection corrections suffices (i.e., a single isoplanatic patch), MOSAIC AO-LLSM provided detailed views of human breast cancer cell (MDA-MB-231) interacting with the zebrafish vasculature with full recovery of all spatial frequencies within the diffraction limit (Fig. 4a). Imaging over 90-minutes, we observed the free flow or slow migration of multiple cancer cells along the vasculature (Fig. 4b, cells labeled 1, 2, 3) as well as an extravasation event (Fig 4b, white arrow), where an MDA-MB-231 begins to breach the vessel wall (Fig. 4b, blue arrow), leading to a tear in the vasculature itself (Fig. 4b, red arrow).

To cover FOVs larger than a single isoplanatic patch, tiling is required, with independent AO corrections applied in each tile. To demonstrate, we studied post-amputation tail fin regeneration in a zebrafish 48 hours post fertilization (hpf) larva over a 216 x 272 x 37 μm^3 volume extending back from the wound (comprising 4 tiles) at 3 min intervals for 12.5 hrs (250 time points, Fig. 4c, Movie S11). This revealed a wide array of subcellular events, including secretion of microvesicles by cells proximal to the wound (Fig. 4d, arrows in yellow box), dynamic remodeling of anchoring fibrils connecting the epidermal basement membrane to the dermal layers (Fig. 4d, arrows in magenta box), mesenchymal cell fusion (plasma membrane followed by nuclear fusion, Fig. 4d, arrows in gray box), and transient erythrocyte trapping within the remodeling vasculature (Fig. 4d, arrows in green box).

AOLLSM also enables quantitative ratiometric biosensor imaging *in vivo*. We performed three-color imaging in the tailbud of a zebrafish embryo 18 hpf expressing markers for membrane, histones, and a cyclin-dependent kinase (CDK) activity sensor[31] (comprising 4 tiles, Fig. 4e, Movie S12). The cytoplasmic-to-nuclear ratio of the sensor quantitatively reports cell cycle state, increasing as cells progress through interphase from G1/S into G2. Our analysis revealed spatial variations in cell cycle state across the tailbud, consistent with previous studies using either FUCCI[32] or a CDK activity sensor imaged by spinning disk confocal microscopy[31]. Cells near the periphery exhibited higher ratios indicative of a higher fraction in G2; (yellow to red cells, Fig. 4e right, Movie S12), relative to those in the interior (blue to green cells, Fig. 4e, right).

Notably, AOLLSM can also be applied to other living multicellular systems, as we demonstrate for *Drosophila* (Fig. S18a), *C. elegans* (Fig. S18b), and human brain organoids (Fig. S18c, Movie S13).

Live adaptive optical SR imaging in zebrafish

Modern SR reconstruction algorithms often assume a diffraction-limited, spatially invariant PSF[33,34], which is distorted by tissue-induced aberrations. These aberrations also quickly attenuate higher spatial frequencies in the OTF to below the noise floor, rendering them useless for resolution extension and further contributing to reconstruction artifacts. AO in such cases is essential.

To demonstrate, we applied AO to LLS-SIM and imaged both cell membranes and mitochondria in the eye of a zebrafish embryo 14 hpf. Applying a 3 x 1 x 2 pattern of tiles to account for variations in the aberration across the eye, we recovered the high modulation contrast from the LLS pattern (Fig. 5a) needed for accurate SIM reconstruction of membrane contours and densely packed mitochondria (Fig. 5b, Fig. S19, Movie S14a) with resolution extension in the patterned direction (upper inset, Fig. 5b). Next, we used AO-LLS-SIM with frame-by-frame denoising to compensate for photobleaching (Fig. S20), and visualized subcellular mitochondrial dynamics in the zebrafish brain 14 hpf for 60 time points at 93 sec intervals (Movie S14b). The high resolution of AO-LLS-SIM allowed us to accurately segment all mitochondria throughout the image volume (Fig. S21) and study relationships between their morphologies and the volumes of the cells in which they exist (Fig. 5c, d), including how they partition between daughter cells during division (Fig. 5e, Movie S14b).

For sufficiently large or oddly shaped specimens, or those having localized regions of large scattering or absorption, it can be difficult to find an orientation and position where the dual objectives of LLSM can both have optical access to the region of interest (Fig. S1b). In such cases, single objective epi illumination can sometimes provide a workable alternative (Fig. S1d). In particular, image scanning microscopy (ISM) with line illumination combines the benefits of rapid volumetric imaging with resolution superior to confocal microscopy in the scan direction (Fig. S22, Movie S15), albeit with far faster photobleaching and poorer axial resolution than LLSM. For imaging in multicellular organisms like zebrafish, AO is needed to recover the high resolution offered by ISM (Fig. 5f, Movie S16). AO-ISM imaging from the dorsal side of a 7 days post fertilization (dpf) zebrafish over 354 × 332 x 16.3 μm^3 with 4 x 3 x 1 AO corrective tiles (Fig. 5 g) allowed us to capture developmental changes such as cell migration within a pair of laterally symmetric neuromast organs (Fig. 5h, i) for 12 time points over 6 hrs (Movie S16) across a broad region encompassing the hindbrain, eyes, and spine.

Adaptive optical two-photon imaging in living tissue

The long excitation wavelength of two-photon microscopy (TPM) enables high resolution fluorescence microscopy at depths in scattering media inaccessible to the linear excitation methods presented above. However, since the same relationship of increasing sample-induced aberration at greater depth still applies (e.g., Fig. 6b, right column), AO can be even more important for TPM.

MOSAIC offers two modes of AO-TPM. For acute brain slices, two-photon scanned Bessel beam light sheet microscopy offers high speed and high axial resolution[35]. However, because both the excitation and detection axes are tilted with respect to the surface of the slice (Fig. S1b), both wavefronts are increasingly sheared with increasing depth within the slice (Fig. S23, left panel).

AO is therefore needed to recover diffraction limited performance (Fig. S23 middle and right panels).

For cortical imaging in live mice, MOSAIC includes an upright station for point scanning TPM (Fig. S1f, Fig. S24a, b). Here, AO is needed to compensate for aberrations introduced by the cortical window as well as the brain itself. Applying unique AO corrections every 25 µm to a depth of 400 µm (16 total corrections, Fig. 6b) over a 100 x 100 FOV (Fig. 6a), we recovered single spine resolution throughout the volume (Fig. 6c, Movie S17) in a mouse expressing cytosolic Thy1-YFP-H in a sparse subset of neurons. In another mouse sparsely expressing GCaMP7s, we imaged neural activity 40 µm deep in dendrites at single spine resolution at 16 frames/sec for 125 sec over a 200 x 200 μm^2 FOV. AO correction improved SNR of the transients (Fig. 6e, Movie S18), leading to the detection of more calcium events in dendritic spines.

The MOSAIC upright AO-TPE subsystem includes a 16 kHz resonant galvo and twin multi-pixel photon counting detectors for two-color imaging of fast events. For example, injecting TexasRed dye into the vasculature of a live Thy1-YFP-H expressing mouse allowed us to visualize the vascular network over a 500 x 500 x 100 µm volume in the context of the surrounding dendritic branches (Fig. 6f-h, Movie S19), and to follow the flow of individual erythrocytes in capillaries at 250 Hz over an 83 x 12.8 μm^2 FOV (Fig. S24d, Movie S20).

Discussion:

MOSAIC was conceived as a platform to combine in a single instrument many of the most popular forms of optical microscopy developed during its 21st century renaissance, thereby: a) greatly decreasing capital and operating costs while increasing utilization rates compared to a stable of similarly performative single-purpose microscopes; b) enabling correlative imaging of dynamic living systems thanks to fast *in situ* mode switching; and c) extending the use space of these modern methods to living multicellular systems, thanks to the incorporation of adaptive optics. As demonstrated by the results shown here, by these metrics it has succeeded.

That being said, MOSAIC is a complex instrument. Documentation alone is nearly 1000 pages of slides and notes. Despite the shared components and pre-aligned optics, the instrument remains optomechanically complex, and simultaneous alignment of all modes (essential to rapidly and easily switch between them) requires exceptional skill and patience. Even learning to operate an assembled MOSAIC across all modes requires a significant investment in time and training. Fortunately, although an imaging core may require the full gamut of functionality to service diverse research projects, the modes are not interdependent. Thus, individual research groups can commission only the subset of them that are catered toward their specific applications.

To date, more than a dozen groups are using MOSAIC, where it has already contributed to a number of technological studies[11,36–40] and biological investigations[41–48]. However, these underscore yet another challenge: the high resolution and high imaging speed of which MOSAIC is capable, applied for long durations across the large specimens which MOSAIC is also equipped to handle, means data, and lots of it: up to 4 TB/hr (Movie S2) and 30-100 TB per dataset (Movies S2, S10). With PetaKit5D, the data at this rate can be processed in real time on a high-

performance distributed computing platform capable of ~15 TFLOPS. However, the resulting post-processed 3D and 4D data at this scale are often too vast, too complex, and too diverse for the human mind to comprehend. A multimodal machine-learning 4D foundation model represents a possible step forward to clear this latest hurdle, and its development lies at the core of our current research[49]. MOSAIC plays a key role in generating the vast training data we need for this purpose.

References

1. Wu, Y. & Shroff, H. Multiscale fluorescence imaging of living samples. *Histochem. Cell Biol.* **158**, 301–323 (2022).
2. Balasubramanian, H., Hobson, C. M., Chew, T.-L. & Aaron, J. S. Imagining the future of optical microscopy: everything, everywhere, all at once. *Commun. Biol.* **6**, 1–12 (2023).
3. Schermelleh, L. *et al.* Super-resolution microscopy demystified. *Nat. Cell Biol.* **21**, 72–84 (2019).
4. Sahl, S. J., Hell, S. W. & Jakobs, S. Fluorescence nanoscopy in cell biology. *Nat. Rev. Mol. Cell Biol.* **18**, 685–701 (2017).
5. Stelzer, E. H. K. *et al.* Light sheet fluorescence microscopy. *Nat. Rev. Methods Primer* **1**, 1–25 (2021).
6. Wu, J., Ji, N. & Tsia, K. K. Speed scaling in multiphoton fluorescence microscopy. *Nat. PHOTONICS* **15**, 800–812 (2021).
7. Xu, C., Nedergaard, M., Fowell, D. J., Friedl, P. & Ji, N. Multiphoton fluorescence microscopy for *in vivo* imaging. *Cell* **187**, 4458–4487 (2024).
8. Wang, K. *et al.* Rapid adaptive optical recovery of optimal resolution over large volumes. *Nat. METHODS* **11**, 625-+ (2014).
9. Liu, T.-L. *et al.* Observing the cell in its native state: Imaging subcellular dynamics in multicellular organisms. *SCIENCE* **360**, eaaq1392 (2018).
10. Zhu, Q. *et al.* Single cell multi-omics reveal intra-cell-line heterogeneity across human cancer cell lines. *Nat. Commun.* **14**, 8170 (2023).

11. Ruan, X. *et al.* Image processing tools for petabyte-scale light sheet microscopy data. *Nat. Methods* **21**, 2342–2352 (2024).
12. Tse, H. T. K., Weaver, W. M. & Di Carlo, D. Increased Asymmetric and Multi-Daughter Cell Division in Mechanically Confined Microenvironments. *PLoS ONE* **7**, e38986 (2012).
13. Ridley, A., Paterson, H., Johnston, C., Diekmann, D. & Hall, A. The Small Gtp-Binding Protein Rac Regulates Growth-Factor Induced Membrane Ruffling. *CELL* **70**, 401–410 (1992).
14. Hoon, J.-L., Wong, W.-K. & Koh, C.-G. Functions and Regulation of Circular Dorsal Ruffles. *Mol. Cell. Biol.* **32**, 4246–4257 (2012).
15. Ikeda, Y. *et al.* Rac1 switching at the right time and location is essential for Fcγ receptor-mediated phagosome formation. *J. CELL Sci.* **130**, 2530–2540 (2017).
16. Leyden, F. *et al.* Rac1 activation can generate untemplated, lamellar membrane ruffles. *BMC Biol.* **19**, (2021).
17. Wu, Y. I. *et al.* A genetically encoded photoactivatable Rac controls the motility of living cells. *NATURE* **461**, 104-U111 (2009).
18. Chen, J. *et al.* Single-Molecule Dynamics of Enhanceosome Assembly in Embryonic Stem Cells. *CELL* **156**, 1274–1285 (2014).
19. Chen, B.-C. *et al.* Lattice light-sheet microscopy: Imaging molecules to embryos at high spatiotemporal resolution. *SCIENCE* **346**, 439-+ (2014).
20. Weigert, M. *et al.* Content-aware image restoration: pushing the limits of fluorescence microscopy. *Nat. Methods* **15**, 1090–1097 (2018).
21. Legant, W. R. *et al.* High-density three-dimensional localization microscopy across large volumes. *Nat. Methods* **13**, 359–365 (2016).
22. Jungmann, R. *et al.* Multiplexed 3D cellular super-resolution imaging with DNA-PAINT and Exchange-PAINT. *Nat. Methods* **11**, 313–318 (2014).

23. Chen, F., Tillberg, P. W. & Boyden, E. S. Expansion microscopy. *SCIENCE* **347**, 543–548 (2015).
24. Gao, R. *et al.* Cortical column and whole-brain imaging with molecular contrast and nanoscale resolution. *SCIENCE* **363**, 245-+ (2019).
25. Sun, Z. *et al.* Modeling late-onset Alzheimer's disease neuropathology via direct neuronal reprogramming. *SCIENCE* **385**, adl2992 (2024).
26. Feldman, M. L. & Peters, A. Ballooning of myelin sheaths in normally aged macaques. *J. Neurocytol.* **27**, 605–614 (1998).
27. Coleman, M. P. & Hoke, A. Programmed axon degeneration: from mouse to mechanism to medicine. *Nat. Rev. Neurosci.* **21**, 183–196 (2020).
28. El Hajj, H. *et al.* Ultrastructural evidence of microglial heterogeneity in Alzheimer's disease amyloid pathology. *J. NEUROINFLAMMATION* **16**, 87 (2019).
29. Tsering, W. *et al.* Preferential clustering of microglia and astrocytes around neuritic plaques during progression of Alzheimer's disease neuropathological changes. *J. Neurochem.* **169**, (2025).
30. Buchanan, J. *et al.* Oligodendrocyte precursor cells ingest axons in the mouse neocortex. *Proc. Natl. Acad. Sci.* **119**, e2202580119 (2022).
31. Adikes, R. C. *et al.* Visualizing the metazoan proliferation-quiescence decision in vivo. *eLife* **9**, e63265 (2020).
32. Bouldin, C. M., Snelson, C. D., Farr, G. H. & Kimelman, D. Restricted expression of cdc25a in the tailbud is essential for formation of the zebrafish posterior body. *GENES Dev.* **28**, 384–395 (2014).
33. Zhang, P. *et al.* Deep learning-driven adaptive optics for single-molecule localization microscopy. *Nat. Methods* **20**, 1748–1758 (2023).

34. Lin, R., Kipreos, E. T., Zhu, J., Khang, C. H. & Kner, P. Subcellular three-dimensional imaging deep through multicellular thick samples by structured illumination microscopy and adaptive optics. *Nat. Commun.* **12**, 3148 (2021).
35. Planchon, T. A. *et al.* Rapid three-dimensional isotropic imaging of living cells using Bessel beam plane illumination. *Nat. Methods* **8**, 417–423 (2011).
36. Liu, G. *et al.* Characterization, comparison, and optimization of lattice light sheets. *Sci. Adv.* **9**, eade6623 (2023).
37. Shi, Y., Daugird, T. A. & Legant, W. R. A quantitative analysis of various patterns applied in lattice light sheet microscopy. *Nat. Commun.* **13**, 4607 (2022).
38. Shi, Y. *et al.* Smart lattice light-sheet microscopy for imaging rare and complex cellular events. *Nat. Methods* **21**, 301–310 (2024).
39. Alshaabi, T. *et al.* Fourier-Based 3D Multistage Transformer for Aberration Correction in Multicellular Specimens. Preprint at https://doi.org/10.48550/arXiv.2503.12593 (2025).
40. Wang, W. *et al.* Nanoscale volumetric fluorescence imaging via photochemical sectioning. 2024.08.01.605857 Preprint at https://doi.org/10.1101/2024.08.01.605857 (2024).
41. Li, T. *et al.* Cellular bases of olfactory circuit assembly revealed by systematic time-lapse imaging. *CELL* **184**, 5107-+ (2021).
42. Wong, K. K. L. *et al.* Origin of wiring specificity in an olfactory map revealed by neuron type–specific, time-lapse imaging of dendrite targeting. *eLife* **12**, e85521 (2023).
43. Mondal, C. *et al.* A proliferative to invasive switch is mediated by srGAP1 downregulation through the activation of TGF-β2 signaling. *Cell Rep.* **40**, 111358 (2022).
44. Neahring, L. *et al.* Torques within and outside the human spindle balance twist at anaphase. *J. Cell Biol.* **223**, e202312046 (2024).
45. Daugird, T. A. *et al.* Correlative single molecule lattice light sheet imaging reveals the dynamic relationship between nucleosomes and the local chromatin environment. *Nat. Commun.* **15**, 4178 (2024).

46. Abdelfattah, A. S. *et al.* Sensitivity optimization of a rhodopsin-based fluorescent voltage indicator. *Neuron* **111**, 1547-1563.e9 (2023).

47. Emmerich, K. *et al.* Nanoparticle-based targeting of microglia improves the neural regeneration enhancing effects of immunosuppression in the zebrafish retina. *Commun. Biol.* **6**, 1–14 (2023).

48. Bertaccini, G. A. *et al.* Visualizing PIEZO1 Localization and Activity in hiPSC-Derived Single Cells and Organoids with HaloTag Technology. 2023.12.22.573117 Preprint at https://doi.org/10.1101/2023.12.22.573117 (2025).

49. Betzig, E. A Cell Observatory to reveal the subcellular foundations of life. *Nat. Methods* **22**, 646–649 (2025).

Acknowledgements:
We thank B. Mehl, H. Ma, J. Brooker (Thorlabs Imaging), and R. Correia for helpful discussions. We thank A. Sun, M. Freeman, A. Doriwala, F. Kong, C. Huynh, K. Ayaagari, S. Ganti, M. Zhou for their assistance. We thank D. Wagner and N. Shaner for the eef1a1l1 promoter and the mChilada fluorescent protein plasmid, respectively, which were used to generate reagents for this study. We thank Janelia Research Campus' support teams: Cell Culture (K. Schaefer and B. Blanco for help with cell culture), Vivarium (J. Rouchard for help with zebrafish aquatics), and Janelia Experimental Technology (B. Biddle and B. Bowers for help with machining, J. Arnold for help in designing the toggle stage mount in the detection path, and V. Goncharov for helpful discussion on two photon point scanning mode). We thank J. White for managing the Advanced Bioimaging Center's computing cluster at UC Berkeley.

Funding:
T.M.F., D.E.M., V.K., L.G., and E.B. are supported by the HHMI (awarded to E.B.). G.L., F.G., V.F., M.M., K.A. and S.U. are supported in part by the Philomathia Foundation (awarded to E.B. and S.U.). G.L. and X.R. are partially supported by the Chan Zuckerberg Biohub gift (awarded to S.U.). G.L. is supported in part by Sloan Foundation (awarded to S.U.). X.R. and S.U. are partially supported by Lawrence Berkeley National Laboratory's LDRD program 7647437 and 7721359 (awarded to S.U.). C.S. and D.G.D. are partially supported by National Institutes of Health (NIH) Grant R35GM118149 (awarded to D.G.D.). W.W. and R.G. are partially supported by the University of Illinois Chicago Startup Fund. R.C.A. was supported by NIH Grant F32GM133131. I.A.S. is partially supported by NIH Grant 1R01DC021710 (awarded to I.A.S.). F.G. is partially funded by the Feodor Lynen Research Fellowship, Humboldt Foundation. S.U. is funded by the Chan Zuckerberg Initiative Imaging Scientist program 2019-198142 and 2021-244163. N.D. is supported by CIRM training program EDUC4-12790. M.P. and J.N. are supported by NIH Grants DP2AT010376 and R01NS109810 (awarded to M.P.). T.K. was supported by the National

Institute of General Medical Sciences Maximizing Investigators' Research Award GM130386. L.L. was supported by NIH Grant R01-DC005982. K.E. was partially supported by NIH T32EY7143-22 award (to the Wilmer Eye Institute), J.S.M. was partially supported by NIH R01OD020376 award (to J.S.M.). D.Q.M. was partially supported by NIH Grant R01GM121597. B.L.M was partially supported by NIH Grant R35GM150290. J.J.B.-C was supported by R01CA244780, the Irma T. Hirschl Trust, the Emerging Leader Award from the Mark Foundation (to J.J.B.-C) and the Tisch Cancer Institute NIH Cancer Center grant P30-CA196521. C.M. received support from an NIH T32 CA078207 Training Program in Cancer Biology. S.A. is supported by EMBL Australia and DBT/Wellcome Trust Team Science Grant. W.R.L., Y.S., and T.A.D. acknowledge support from the NIH grant 1DP2GM136653 (awarded to W.R.L.). W.R.L. acknowledges additional support from the Searle Scholars program, the Beckman Young Investigator Program and the Packard Fellowship for Science and Engineering.
E.B. and LL are HHMI Investigators. S.U. is a Chan Zuckerberg Biohub – San Francisco Investigator.

Contributions:
Project Supervision: EB, WRL, SU
Microscope design, construction, and validation: TMF, GL, DEM, FG, VF, VK, LG, DS, EB, WRL, SU
Instrument control software: DEM
Biological reagents, methodology and investigation: TMF, GL, YS, NSD, WW, HMY, YL, TAD, MJG, KAL, RCA, CS, JLN, SHS, TL, CM, KA, WH, KE, PD, ZJL, JSM, DD, MK, AK, JBC, CDK, LL, TK, MMP, SA, JKN, RG, DQM, BLM, IS, WRL, SU
Analysis software: GL, DEM, XR, MM, WRL, SU
Formal analysis: GL, XR, YS, TAD, NH, WRL, SU
Data visualization, figure and movie preparation: TMF, GL, DM, TAD, XR, HMY, WRL, SU
Manuscript preparation: TMF, GL, EB, WRL, SU with input from all coauthors
Funding acquisition: DD, ZJL, DC, JM, MK, CDK, LL, TK, MMP, SA, JKN, RG, DM, BLM, IAS, EB, WRL, SU

Competing interests: Portions of the technology described herein are covered by U.S. Patent 7,894,136 issued to E.B., assigned to Lattice Light of Ashburn, VA, and licensed to Carl Zeiss Microscopy; U.S. Patents 8,711,211 and 9,477,074 issued to E.B., assigned to HHMI, and licensed to Carl Zeiss Microscopy; U.S. Patent application 13/844,405 filed by E.B. and assigned to HHMI; and U.S. Patent 9,500,846 issued to E.B. and assigned to HHMI.

Data and materials availability: All data needed to evaluate the conclusions in the paper are present in the paper or the supplementary materials. Extensive documentation for the construction of a MOSAIC microscope or our earlier lattice light-sheet microscope can be obtained by execution of a research license agreement with HHMI.

Main Figures

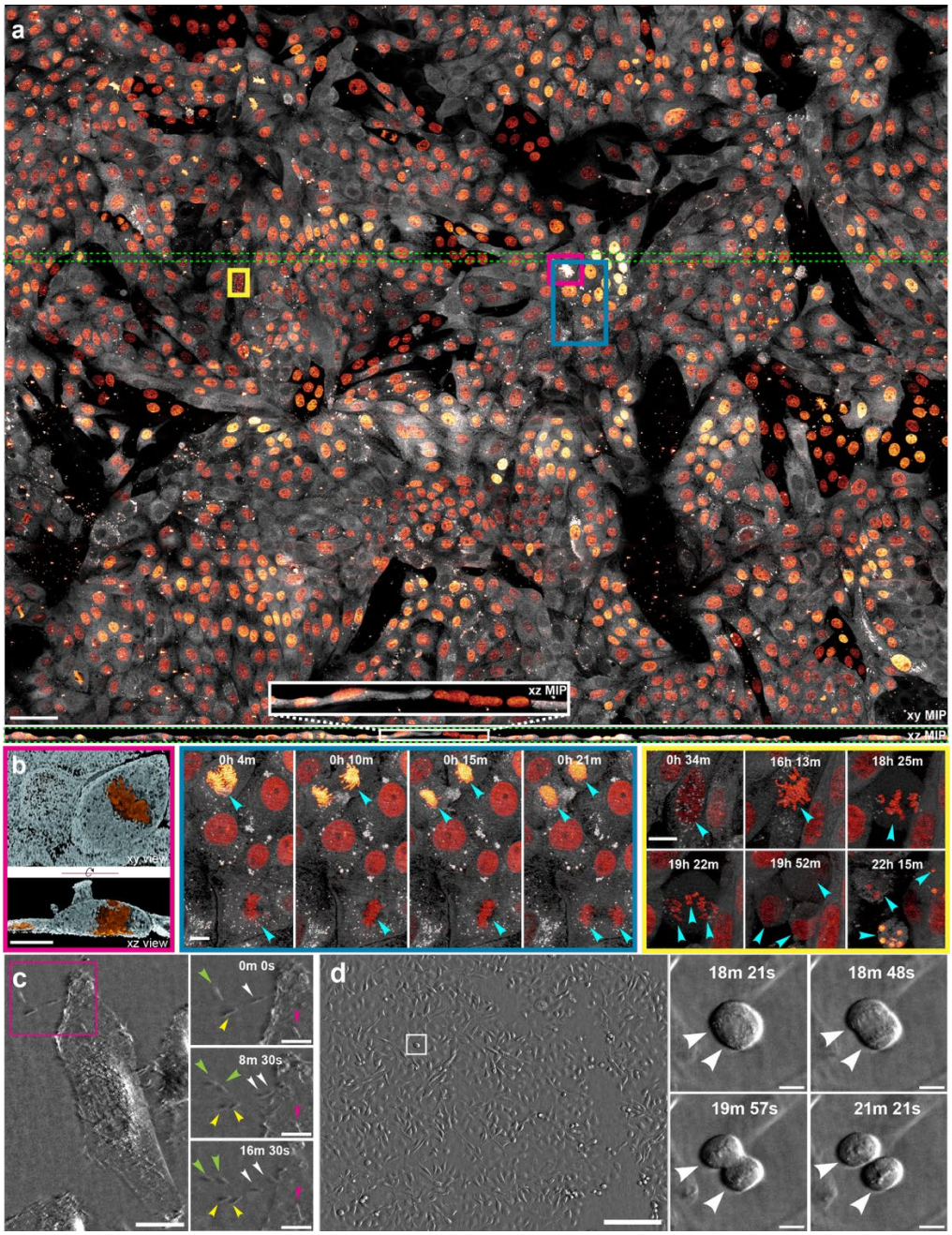

Fig. 1. Large field-of-view dynamic imaging with 3D lattice light-sheet or 2D label-free oblique illumination microscopy. (a) LLSM image from Movie S2 of LLC-PK1 cells expressing Calnexin-mEmerald (ER) and H2B-mCherry (nuclei). Maximum-intensity-projections (MIPs) show xy (top) and xz (bottom) views of the 1000 x 750 x 10 μm^3 volume. Scale bar, 50 µm. **(b)** Zoomed views of cell division events from (**a**). Left: volume rendering of a metaphase cell having a large ER protrusion; Middle: four points in nominal cell division from metaphase to telophase; Right: six points during a rare tripolar mitotic event. Scale bar, 10 µm. **(c)** Label-free OI imaging at 100 Hz (Movie S3) captures HeLa cell lamellipodial ruffling and replication of contaminating bacteria. Scale bar, 10 µm. Right: Magnified view (magenta box) of three bacterial division events (arrows). Scale bar, 2 µm. **(d)** Tiled label-free imaging over a 1218 x 975 μm^2 field of live U2OS cells at 1 Hz. Scale bar, 200 µm. Right: Zoomed view (white box) of a single dividing U2OS cell at four points, showing condensed chromosomes (arrows). Scale bar, 10 µm (right).

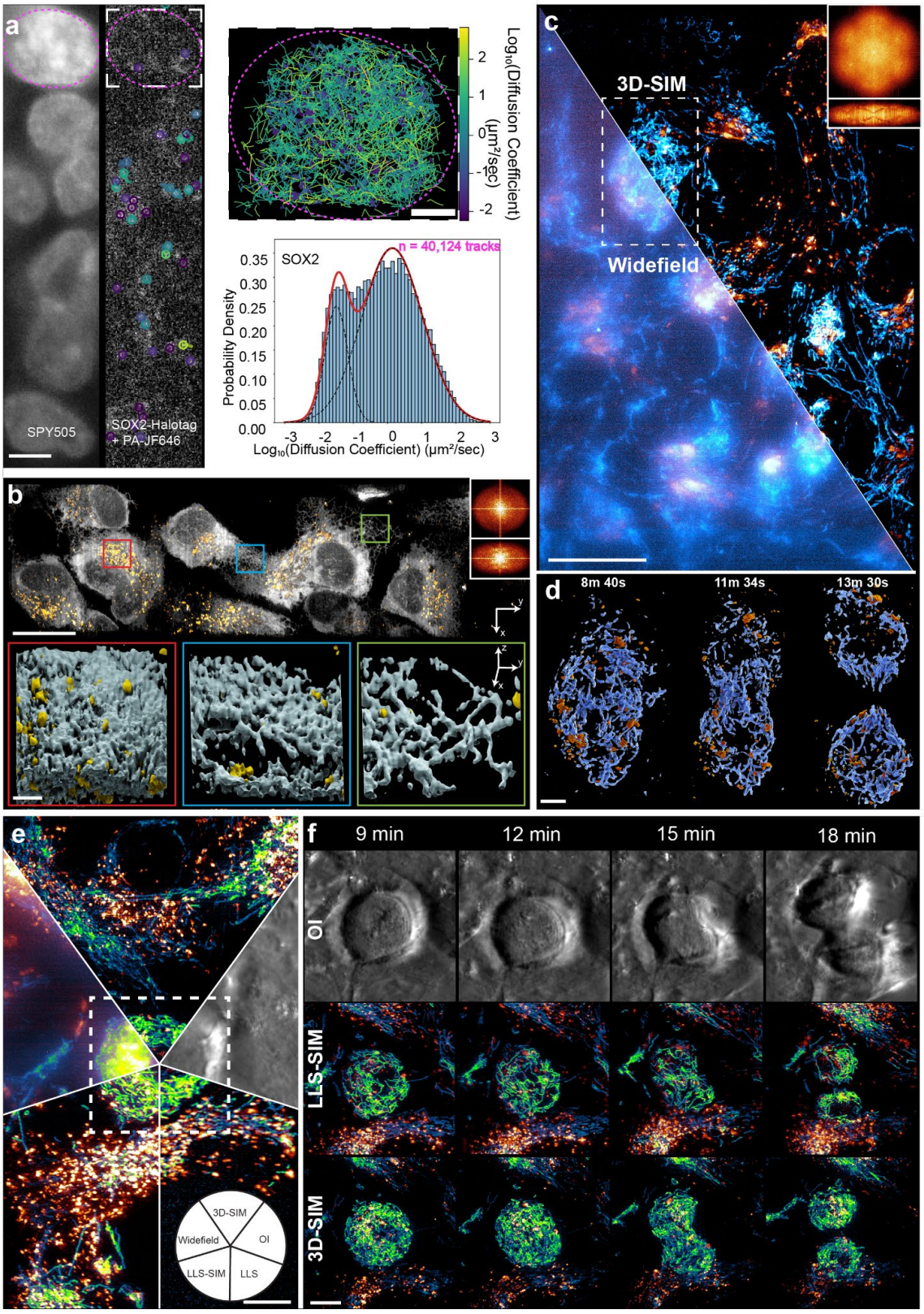

Fig. 2. **Multimodal super-resolution imaging of subcellular dynamics. (a))** Nuclear imaging (SPY 505) and single-particle tracking with LLSM, visualizing molecular trajectories and diffusion dynamics of SOX2 (HaloTag-PA-JF646) in

mESC cells at 50 Hz. Scale bar (left panel), 5 μm. Scale bar (upper right panel), 2 μm. **(b)** Top: LLS-SIM xy MIP of hTERT-RPE1 cells expressing ER (StayGold-ER, gray) and Golgi (β4Gal-HaloTag9 labeled with JFX 549, orange), from Movie S6. Insets: corresponding xy and yz OTFs. Scale bar, 25 μm. Bottom: Volume renderings from boxed regions above showing ER and Golgi organization. Scale bar, 2 μm. **(c)** Comparison of widefield and 3D-SIM imaging in hTERT-RPE1 cells with mitochondria (COX8a-StayGold, cyan) and Golgi marker (orange). Scale bar, 25 μm. Insets: 3D-SIM OTFs. **(d)** Time-lapse 3D-SIM (Movie S7) captures mitochondrial and Golgi dynamics during cell division (white box from (c)). Scale bar, 5 μm. **(e)** Correlative optical microscopy applying multiple imaging modalities (widefield, 3D-SIM, OI, LLS, and LLS-SIM) to a dividing hTERT-RPE1 cell with labeled mitochondria (blue-green) and Golgi (orange), from Movie S8. Scale bar, 10 μm **(f)** Time-lapse sequence of the correlative imaging shown in (e). Scale bar, 10 μm.

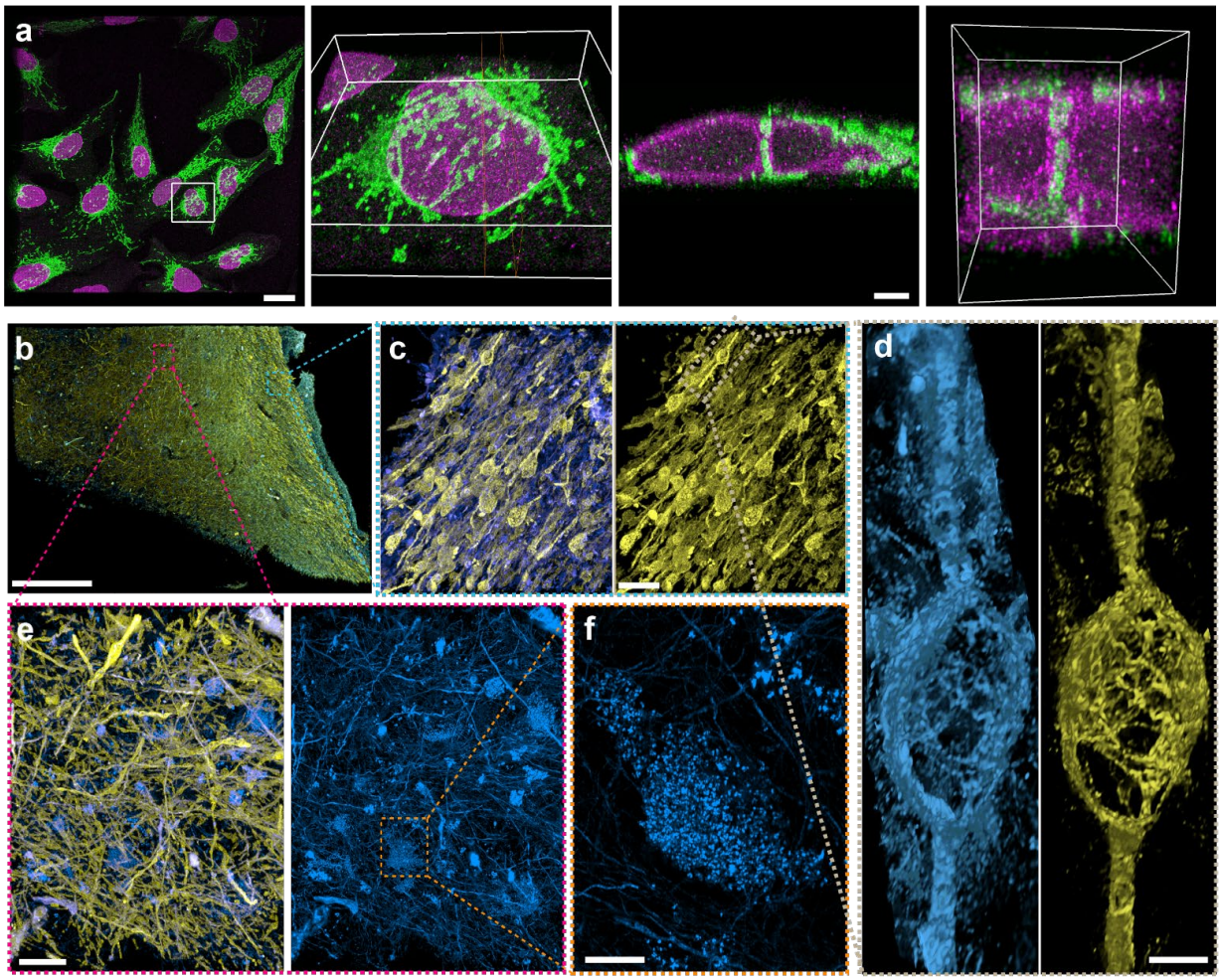

Fig. 3. Volumetric imaging with nanoscale resolution. (a) Two-color 3D DNA PAINT of the mitochondrial marker TOMM-20 and the nuclear envelope protein marker Lamin A/C in U2OS cells. Left to right: Overview MIP of a 180 x 200 x 17 μm^3 FOV (scale bar, 20 μm), zoomed 3D rendering of a single cell (boxed region, 28 x 23 x 5.4 μm^3), its xz orthoslice (scale bar, 2 μm), and the close-up of nuclear invaginations (boxed region, 4.7 x 4.5 x 5.4 μm^3). See also Movie S9. **(b)** ExLLSM MIP overview of a 2,000 x 2,375 x 98 μm^3 human hippocampal tissue section from an Alzheimer disease patient, after 4x expansion. NF-200 (blue) and MBP (yellow) label neurofilaments and myelin sheaths, respectively. Scale bar, 500 μm. **(c)** Zoomed view from (b) showing neurofilament and myelin sheath ballooning. Scale bar, 20 μm. (**d**) Nanoscale structure of axon and myelin sheath blebs. Scale bar, 2 μm. **(e)** Zoomed region from (b) highlighting clustering of NF-200 protein. Scale bar, 20 μm. **(f)** Nanoscale structure of an individual NF-200 cluster. Scale bar, 2 μm. Scale bars throughout represent pre-expansion dimensions.

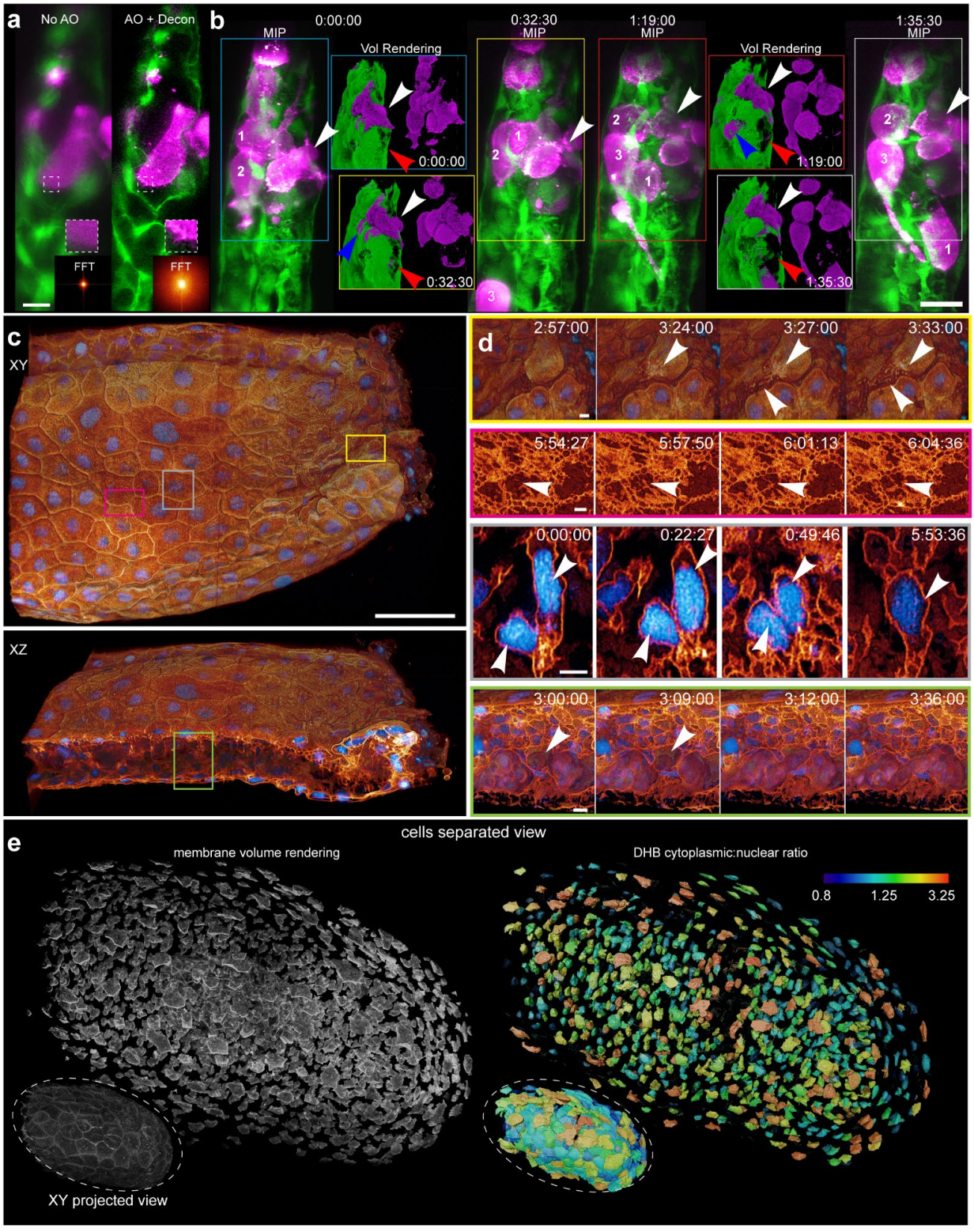

Fig. 4. Observing cellular and subcellular dynamics within zebrafish embryos. (a) Comparison of LLSM imaging in a zebrafish xenograft system (55 x 183 x 50 μm^3) showing actin-labeled MDA-MD-231 human breast cancer cells (magenta) within the zebrafish vasculature (green), both without AO (left) and with AO correction plus deconvolution

(right). Insets: corresponding FFTs (at gamma = 0.3) of the magenta channel. Scale bar, 10 μm. **(b)** Time-lapse imaging of (a) captures cancer cell dynamics and vascular damage during extravasation. Scale bar, 20 μm. **(c)** Zebrafish tail fin volume (216 x 272 x 37 μm^3) 66 hours post-amputation showing plasma membranes and nuclear histones. Scale bar, 50 μm. **(d)** Cellular and subcellular events during the initial stages of regeneration after amputation (Movie S11), showing: extracellular vesicle release from a cell adjacent to the cut site (yellow box); anchoring fibril dynamics in the epidermal basement membrane (red box); a mesenchymal cell fusion event (gray box); and a transiently trapped red blood cell during remodeling of the caudal vascular plexus (green box). Scale bar, 5 μm. **(e)** Visualization of cell cycle state across the fin, based on the cytoplasmic to nuclear fluorescence ratio of CDK biosensor DHB, in segmented and computationally separated cells (216 x 173 x 37 μm^3 pre-separation, inset). Peripheral cells have the highest fraction in G2 (Movie S12).

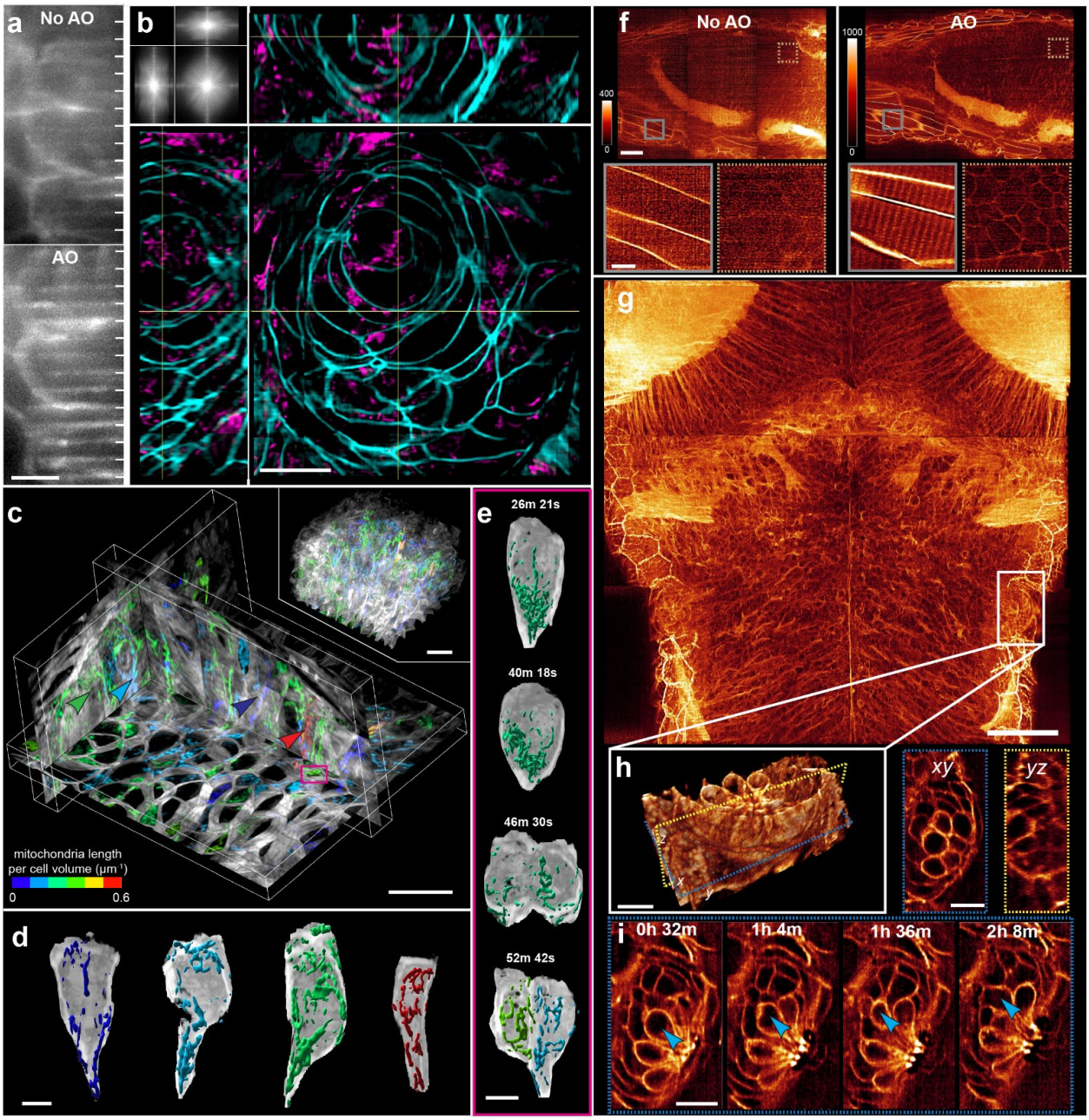

Fig. 5. Super-resolution imaging *in vivo*. (a) MIPs of raw zebrafish membrane images with LLS-SIM illumination without (top) and with AO (bottom). Ticks show the expected positions of the LLS pattern excitation maxima. Scale bar, 5 μm. **(b)** Orthoslices (180 nm thick) in xy, xz, and yz from an AO-LLS-SIM reconstruction (61 x 57 x 40 μm^3) in the eye of a 14 hpf zebrafish embryo expressing mitochondrial (magenta) and plasma membrane (cyan) markers. Scale bar, 10 μm. Top left inset: FFT of reconstructed mitochondria (Movie S14). **(c)** AO-LLS-SIM MIPs of orthogonal slabs (3 μm thick) in the hindbrain from a 56 x 56 x 40 μm^3 volume (inset) in a 14 hpf zebrafish with mitochondria in RGB colors and membrane in grey. Mitochondria in each cell are color-coded by the ratio of total mitochondrial length to cell volume. Scale bar, 10 μm. **(d)** Cutaway view of segmented mitochondria in four different segmented cells. Scale bar, 4 μm. **(e)** Cutaway view of one cell from the volume, showing mitochondrial rearrangements to the daughter cells during division. Scale bar, 4 μm. **(f)** Top: ISM MIP views before and after AO correction of a 0.324 μm xy orthogonal slab within a larger 336 x 319 x 84 μm^3 image volume spanning brain, muscle, and notochord in a membrane-labeled 7 dpf zebrafish. Scale bar, 50 μm. Bottom: Zoomed views comparing muscle and neural progenitor cells imaged by ISM with and without AO (Movie S16). **(g)** AO-ISM MIP (354 x 332 x 16.3 μm^3) of a dorsal-mounted, membrane labeled, 7 dpf zebrafish.

Scale bar, 50 µm. **(h)** Volume rendering with xy and yz orthoslices through a neuromast. Scale bar, 10 µm. **(i)** Time-lapse AO-ISM showing xy orthoslices of a migrating cell in the neuromast. Scale bar, 10 µm.

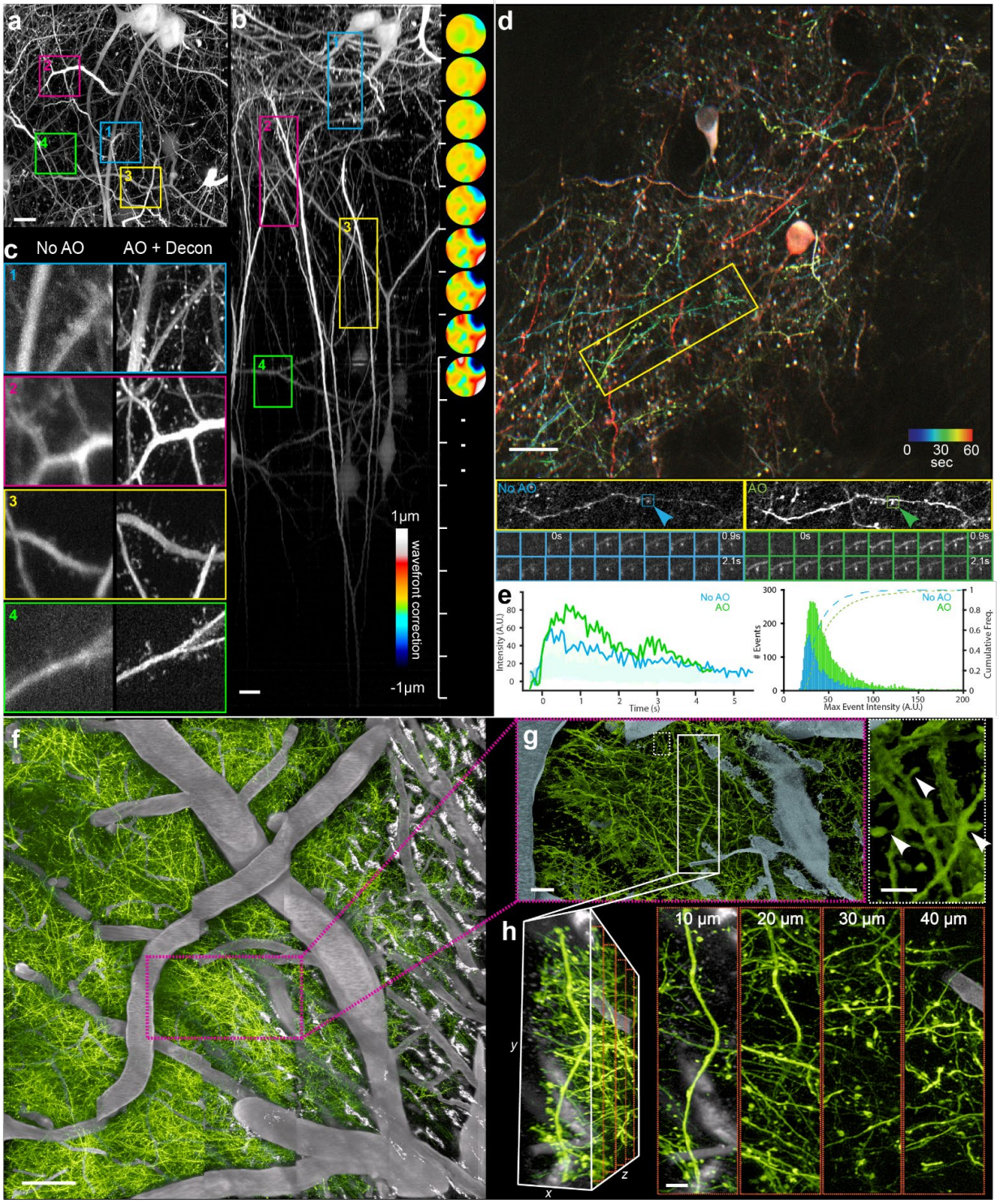

Fig. 6. ***In vivo*** **AO two-photon structural and functional imaging in the mouse cortex. (a, b)** xy (a) and xz (b) MIPS of a 100x100x400 µm³ volume starting at a depth of 60 µm in a Thy1-YFP-H mouse after AO correction and deconvolution (Movie S17). Wavefronts at right in (b) show the measured aberration at 25 µm intervals from 60 to 260 µm deep. Scale bar, 10 µm. **(c)** Zoomed xy MIPS from four color coded subvolumes as shown in (a) and (b), before AO and after AO plus deconvolution **(d)** Functional imaging of neural activity 40 µm deep in the cortex of a GCaMP7s mouse (Movie S18). Top: color-coded time projection. Scale bar, 20 µm. Middle: Single activated dendrite from the

boxed region at top, before and after AO. Bottom: Comparison of raw spikes from the indicated dendritic spine acquired sequentially without and with AO. **(e)** Left: Traces comparing measured calcium transients from the spines indicated in (d). Right: Distribution showing that AO correction yielded a ~2.7x more detectable dendritic spine calcium spikes than without AO over the same duration. **(f)** Two-color *in vivo* AO-TPM of dendrites and vasculature, the latter labeled by injection of TexasRed, over a 500 x 500 x 100 μm³ FOV (Movie S19) with 5 x 5 x 1 AO corrective tiles. Scale bar, 50 μm. **(g)** Left: Zoomed view of the boxed region in (f). Scale bar, 10 μm. Right: individual dendritic spines. Scale bar, 2 μm. **(h)** Additional spines in a further magnified view of the boxed region in (g). Scale bar, 5 μm.

Supplementary Figure

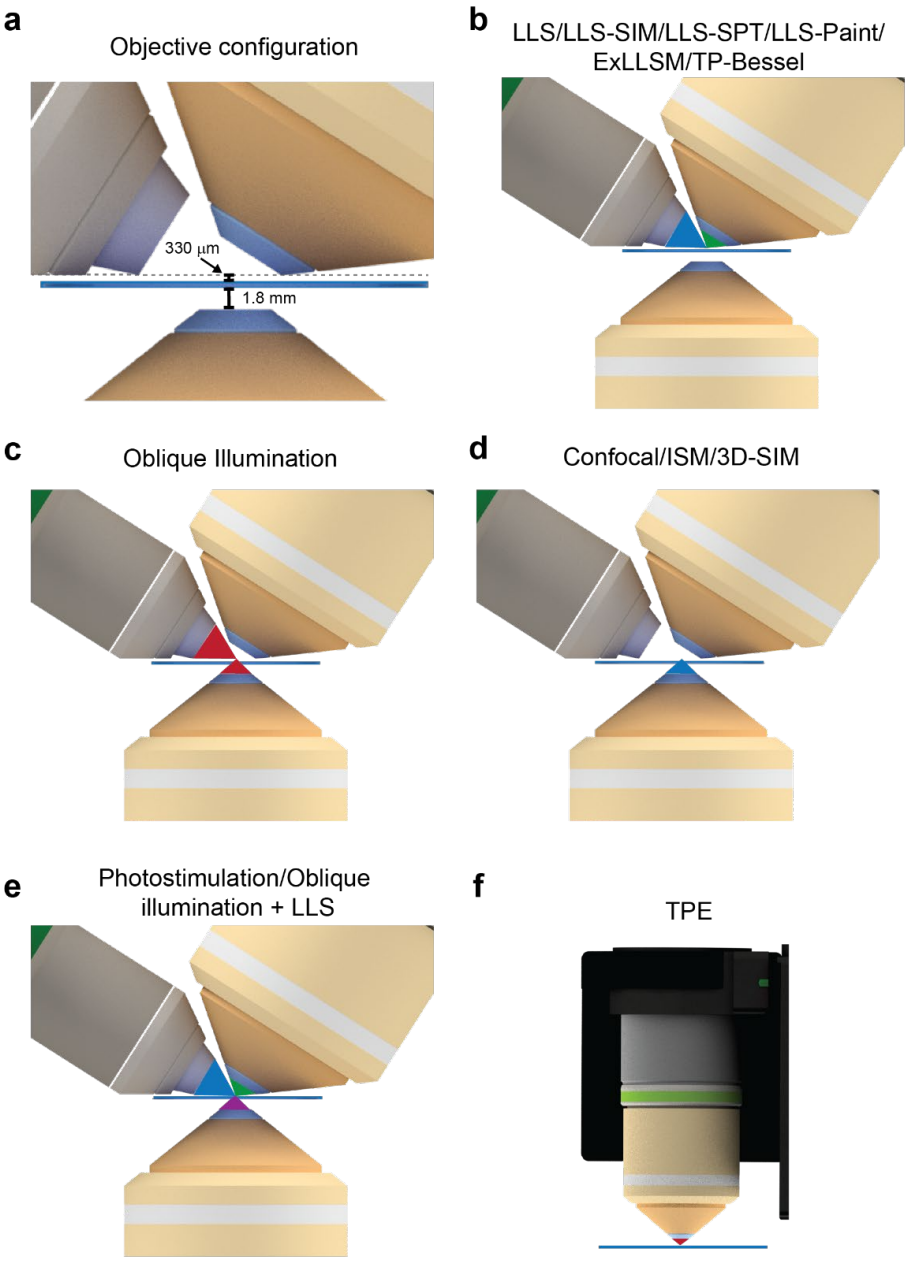

Fig. S1. Objective configurations for each imaging modality. (a) Spatial arrangement of the three co-focal objectives of MOSAIC, showing the 330 µm working distance between the sample coverslip and the corners of the light sheet excitation (left) and detection (right) objectives, as well as the 1.8 mm working distance for the inverted objective. **(b-f)** Light cones indicating the objectives used for each modality: (b) Lattice light sheet (LLS) microscopy and modalities derived from it, including structured illumination (LLS-SIM), single-particle tracking (LLS-SPT), PAINT (LLS-PAINT), expansion (ExLLSM), and two-photon Bessel light sheet microscopy (TP-Bessel); (c) Oblique illumination (OI); (d) Confocal, image scanning, and 3D structured illumination microscopy (3D-SIM); (e) Photostimulation combined with OI and/or LLSM; (f) Upright two-photon microscopy at a dedicated station for mouse imaging.

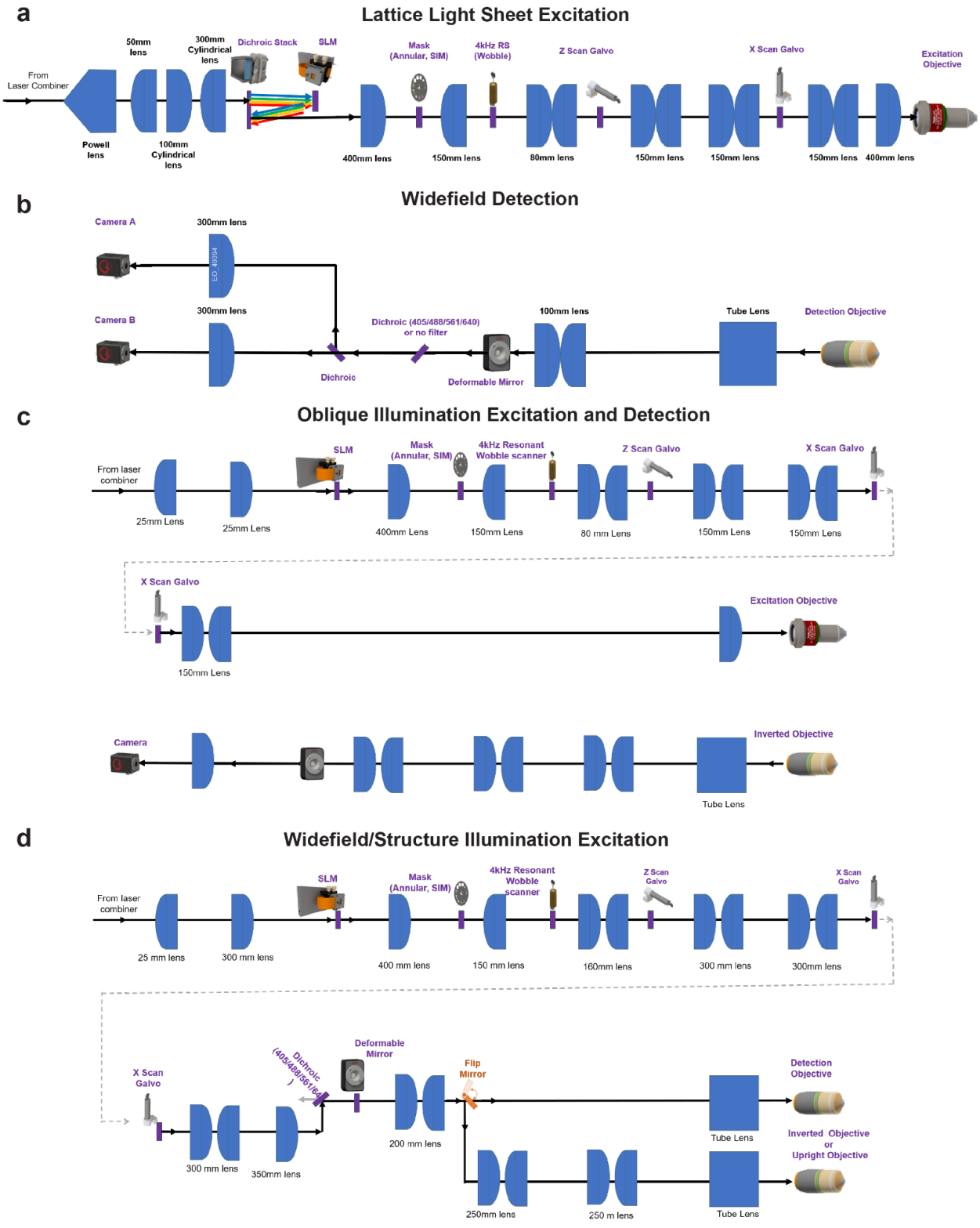

Fig. S2. Optical paths: Part 1. (a) Lattice light sheet excitation, **(b)** Widefield detection, **(c)** Oblique illumination excitation and detection, and **(d)** Widefield/structured illumination excitation.

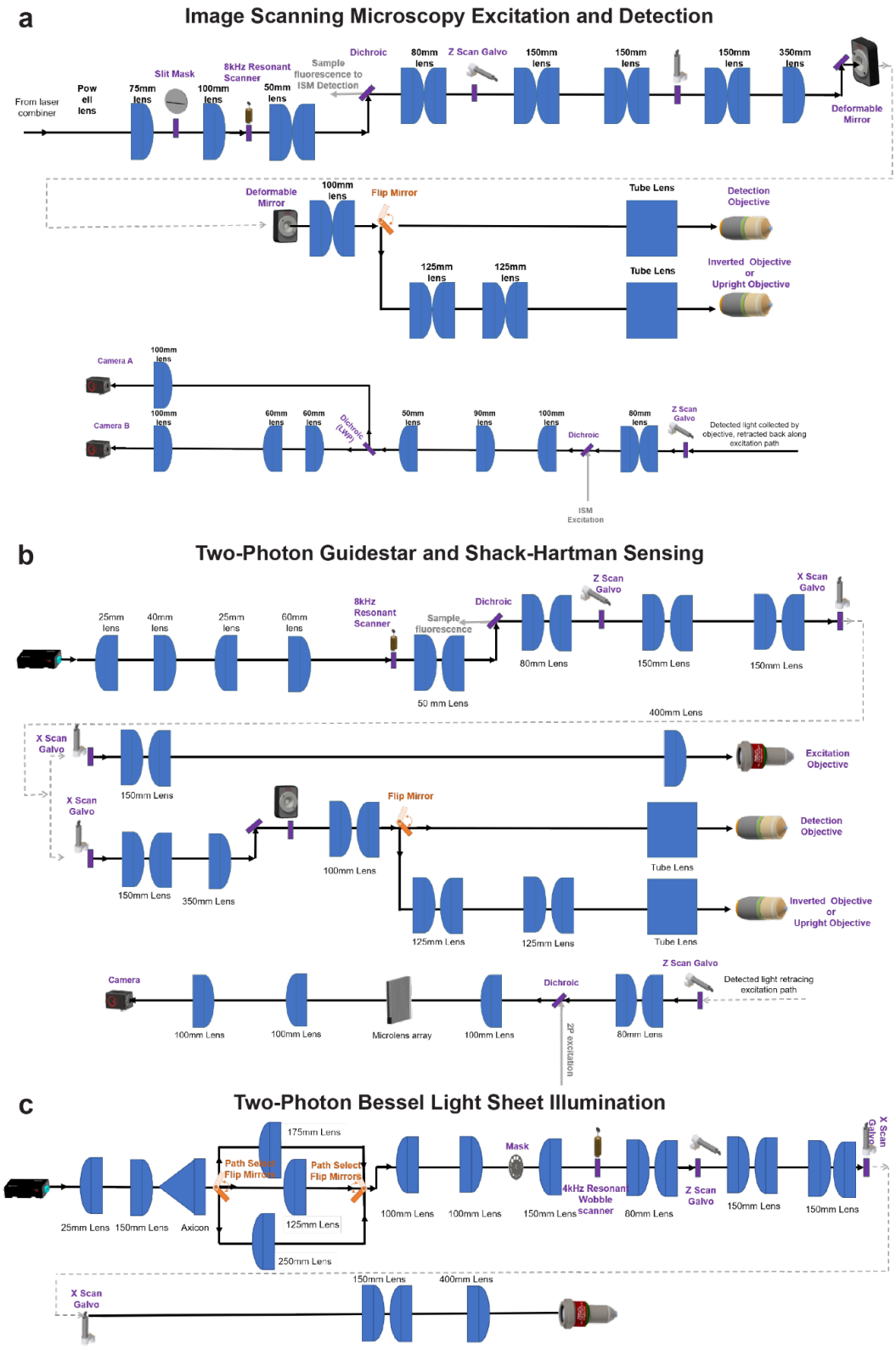

Fig. S3. Optical paths: Part 2. (a) Image scanning microscopy, **(b)** Two-photon guidestar and Shack-Hartman sensing, and **(c)** Two-photon Bessel light sheet microscopy.

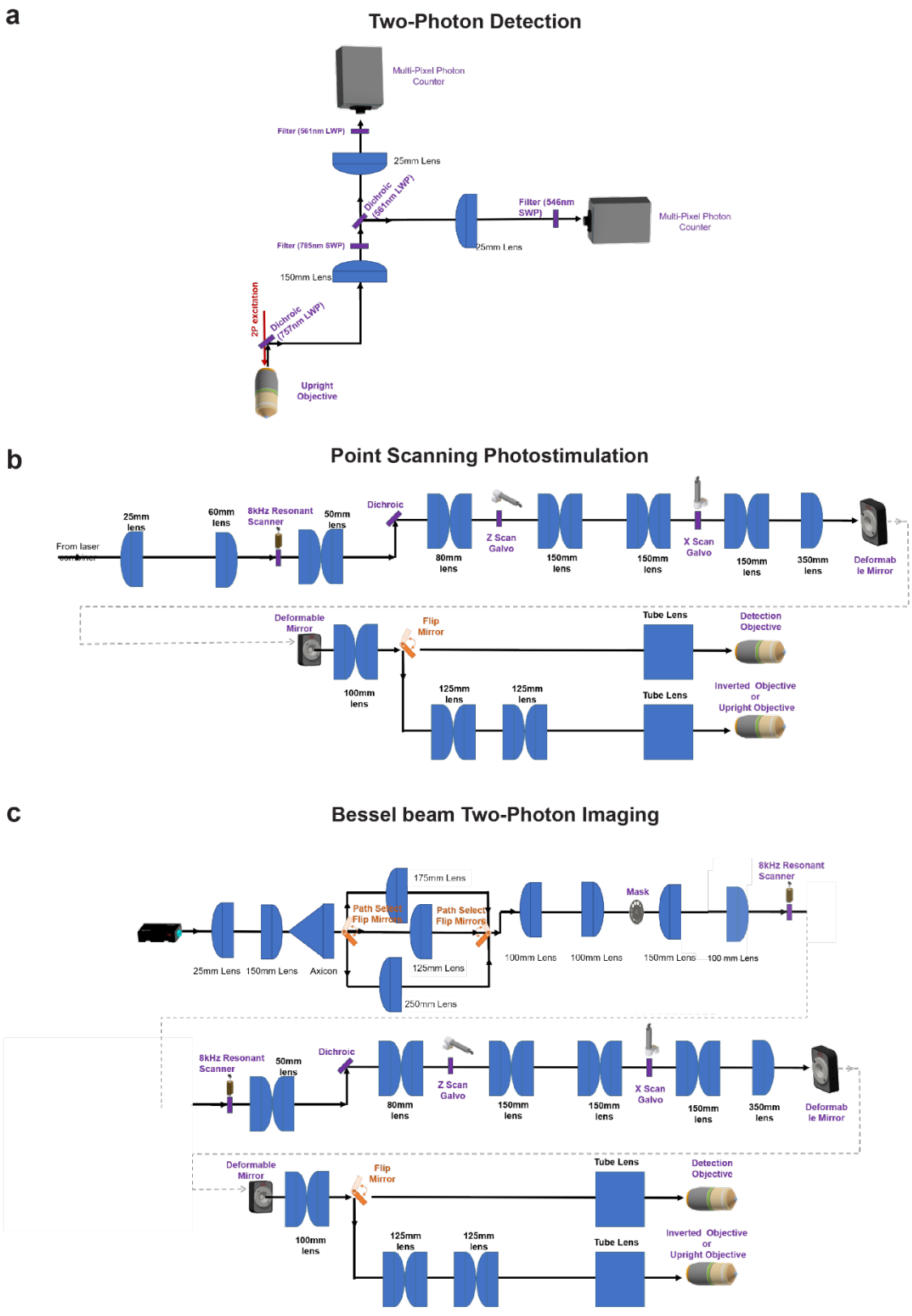

Fig. S4. Optical paths: Part 3. (a) Two-photon point scanning detection, **(b)** Point scanning photostimulation, and **(c)** Bessel beam two-photon scanning.

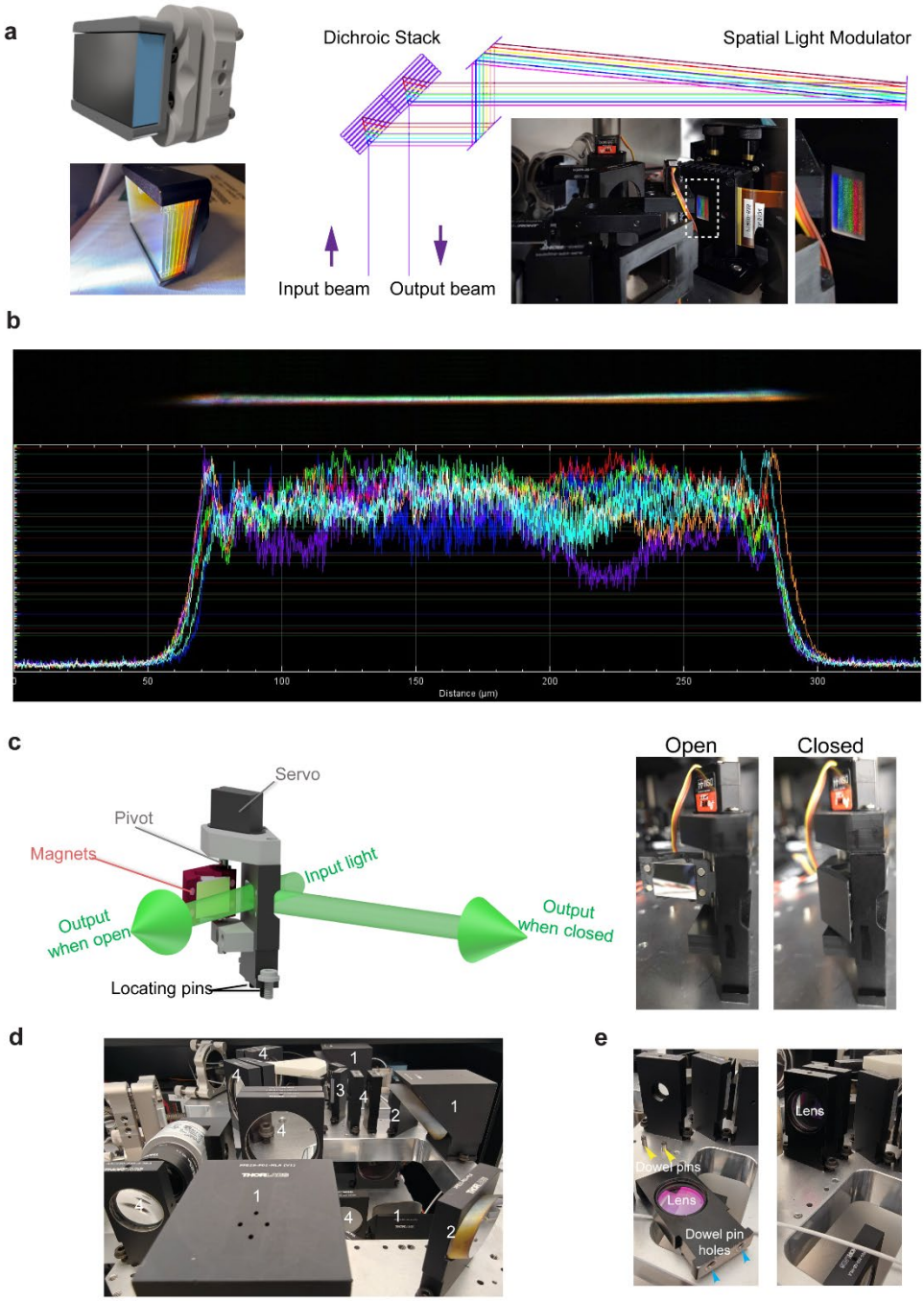

Fig. S5. Novel optical elements used in MOSAIC. (a) Custom dichroic mirror stack consisting of six parallel air gapped dichroic mirrors and one reflective mirror. The stack spectrally separates a co-aligned multicolor input beam, directing each wavelength to a distinct region on a spatial light modulator (SLM) for customized lattice light sheet pattern generation and modification. The reflected beams are recombined by the stack into a single multicolor light sheet of cross-sectional intensity shown in **(b)**. **(c)** Flip mirror mechanism to toggle between orthogonal optical paths. Right: flip mirror in its open (pass through mode) and closed (reflection mode) positions. **(d)** Examples of installed pre-centered optics. 1: vertical 90° elliptical mirror; 2: horizontal 90° elliptical mirror; 3: horizontal square mirror; 4: lens and lens doublet. **(e)** Dowel pins (yellow arrows), and holes (blue arrows) help with precision installation of pre-centered optics.

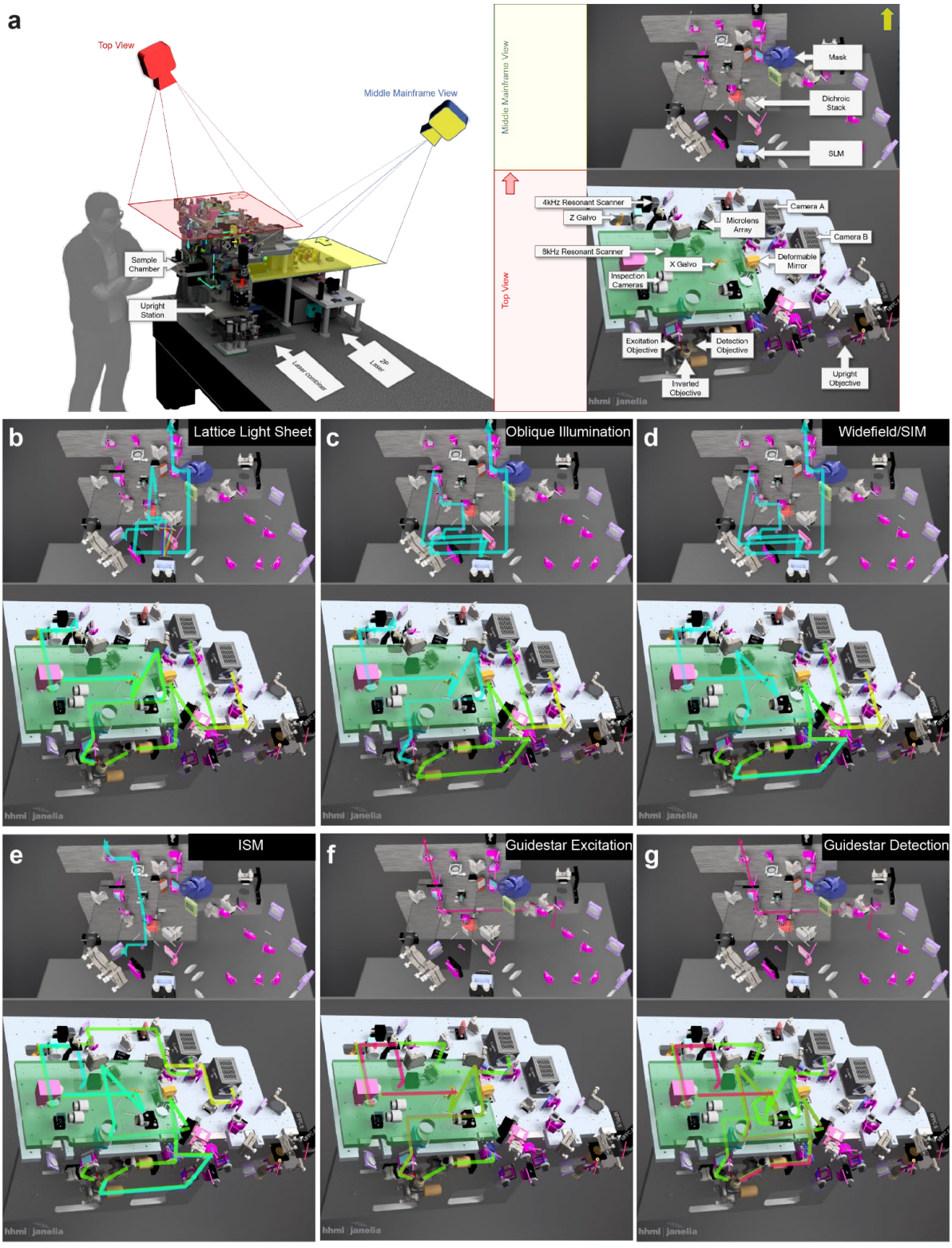

Fig. S6. 3D model with beam paths used by different modalities: Part 1. (a) Left: Overall MOSAIC architecture, with view directions defined for subsequent panels. Right: Major MOSAIC components as seen from these two views. **(b-g)** Optical pathways as seen from the two views for the MOSAIC modes given at upper right of each panel.

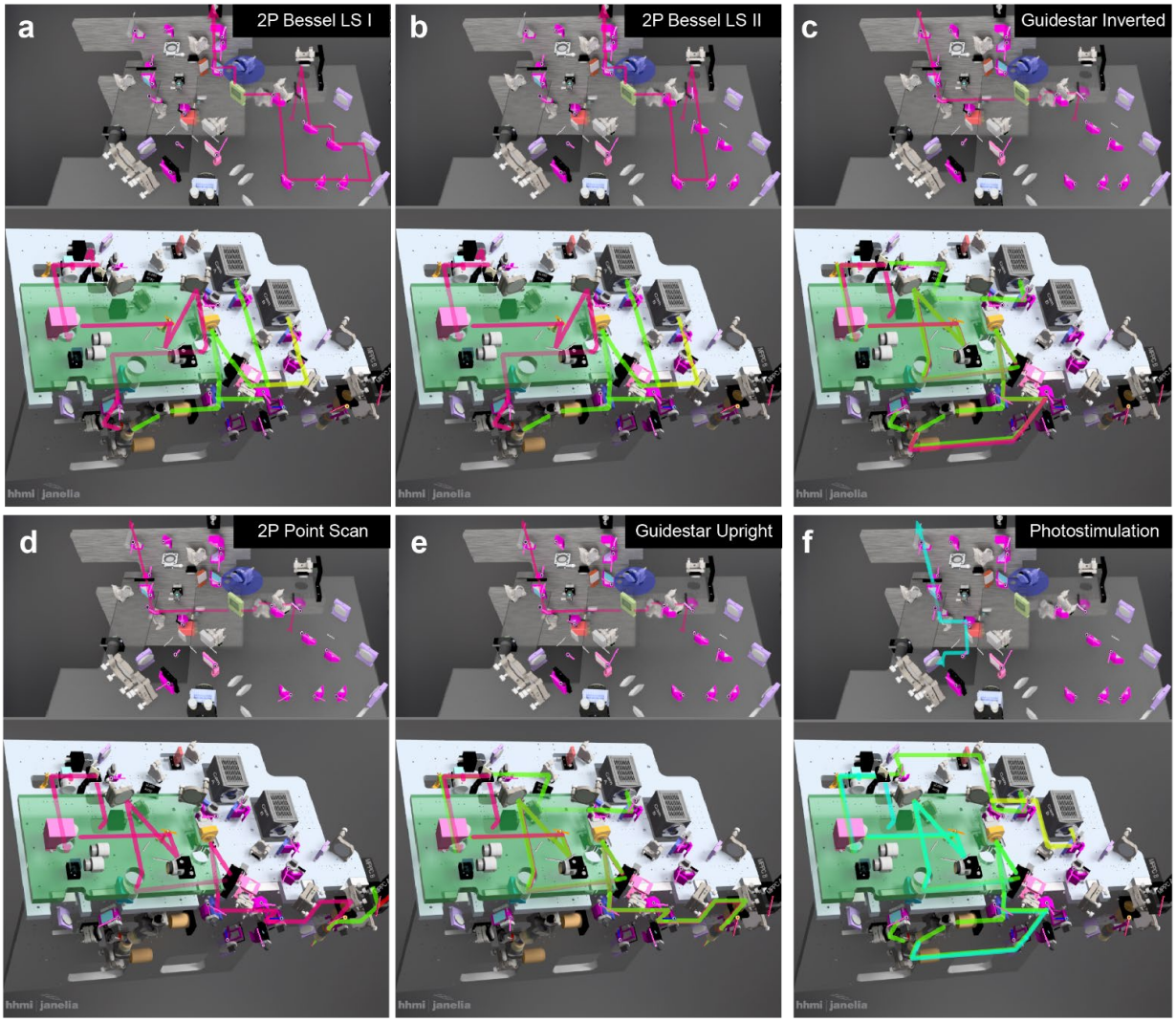

Fig. S7. 3D model with beam paths used by different modalities: Part 2. Optical pathways for six more MOSAIC modes as described at upper right of each panel, as seen from the two views in Fig. S6a.

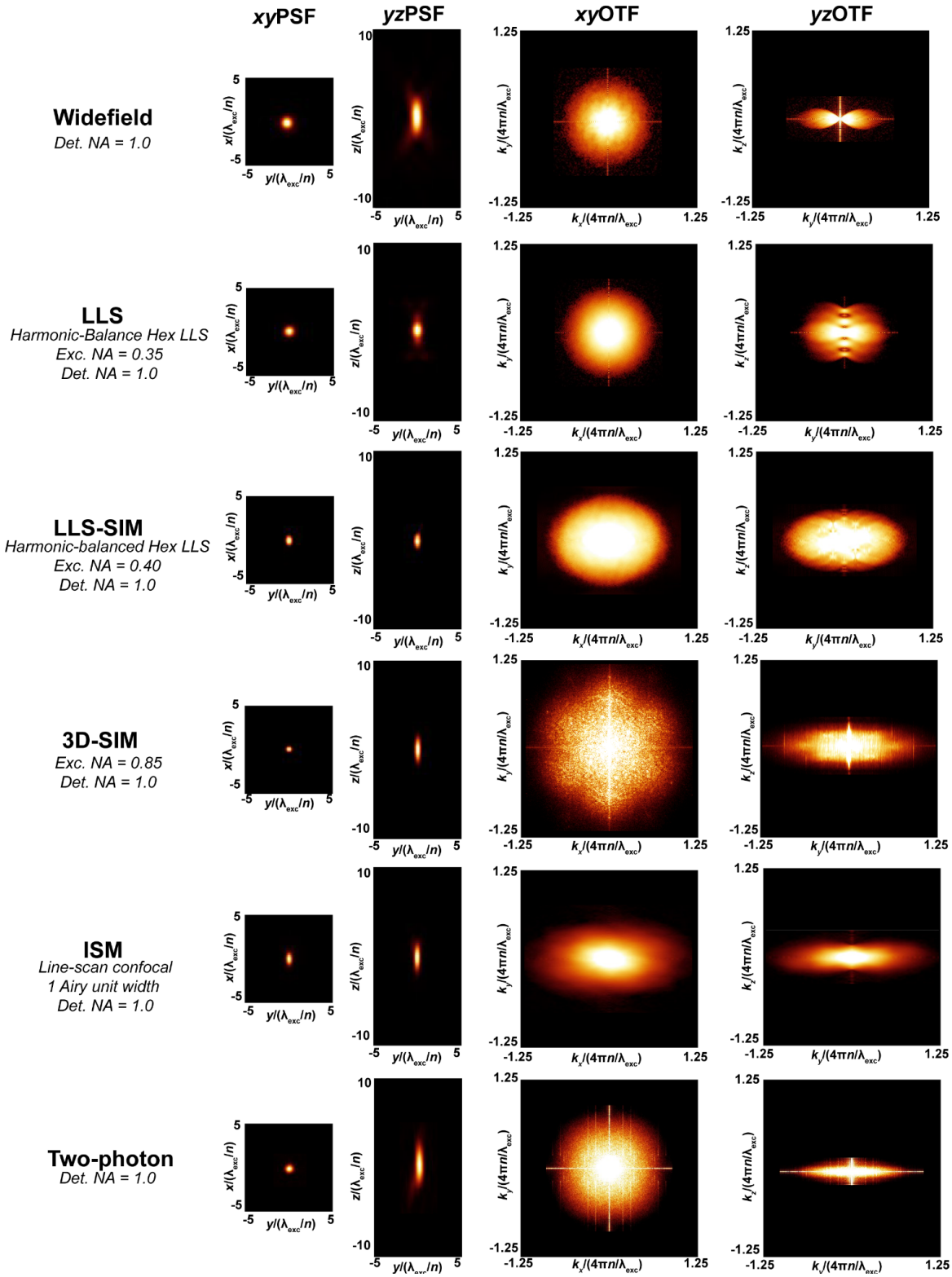

Fig. S8. Experimental PSFs and OTFs for different MOSAIC modes. Gamma = 0.5 was applied to the OTF plots.

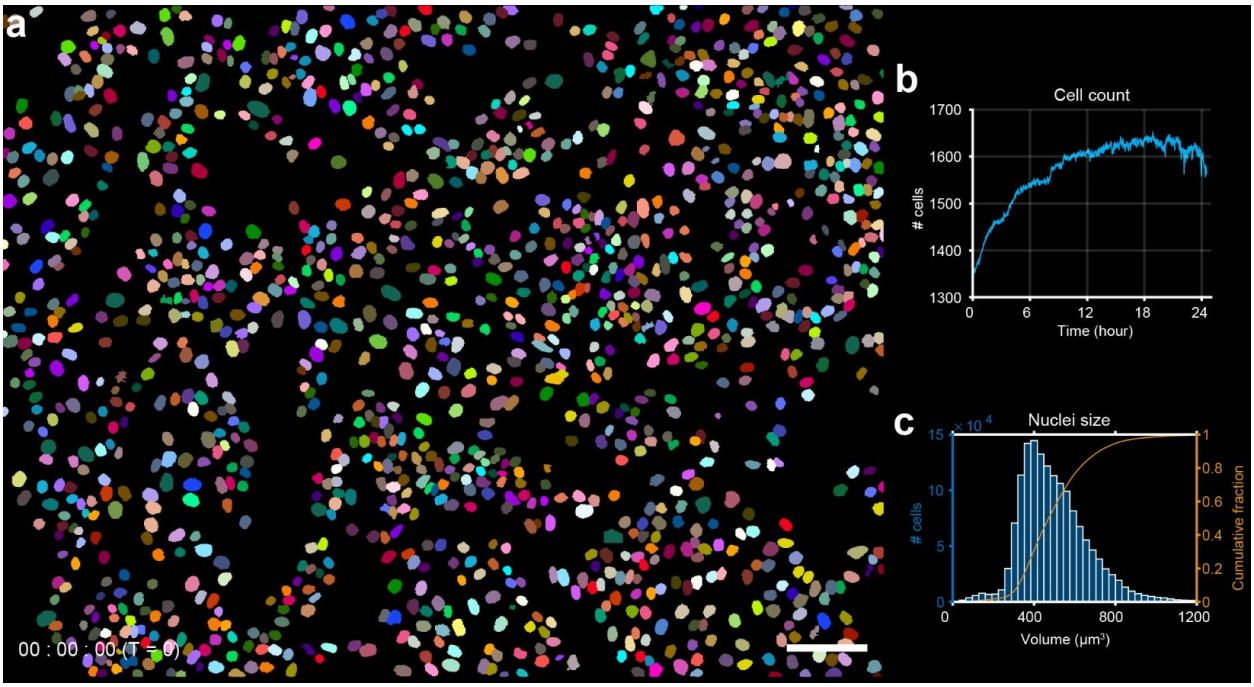

Fig. S9. Analysis of nuclear dynamics from long-term imaging of LLC-PK1 cells. (a) MIP of segmented nuclei, randomly colored, at the start of a 24-hour imaging experiment (t=0). Scale bar; 100 μm. **(b)** Cell population growth, as measured by number of segmented nuclei, over the 24-hours. **(c)** Histogram (left axis) and corresponding cumulative distribution function (right axis) for all nuclear volumes measured across all time points. From Movie S2.

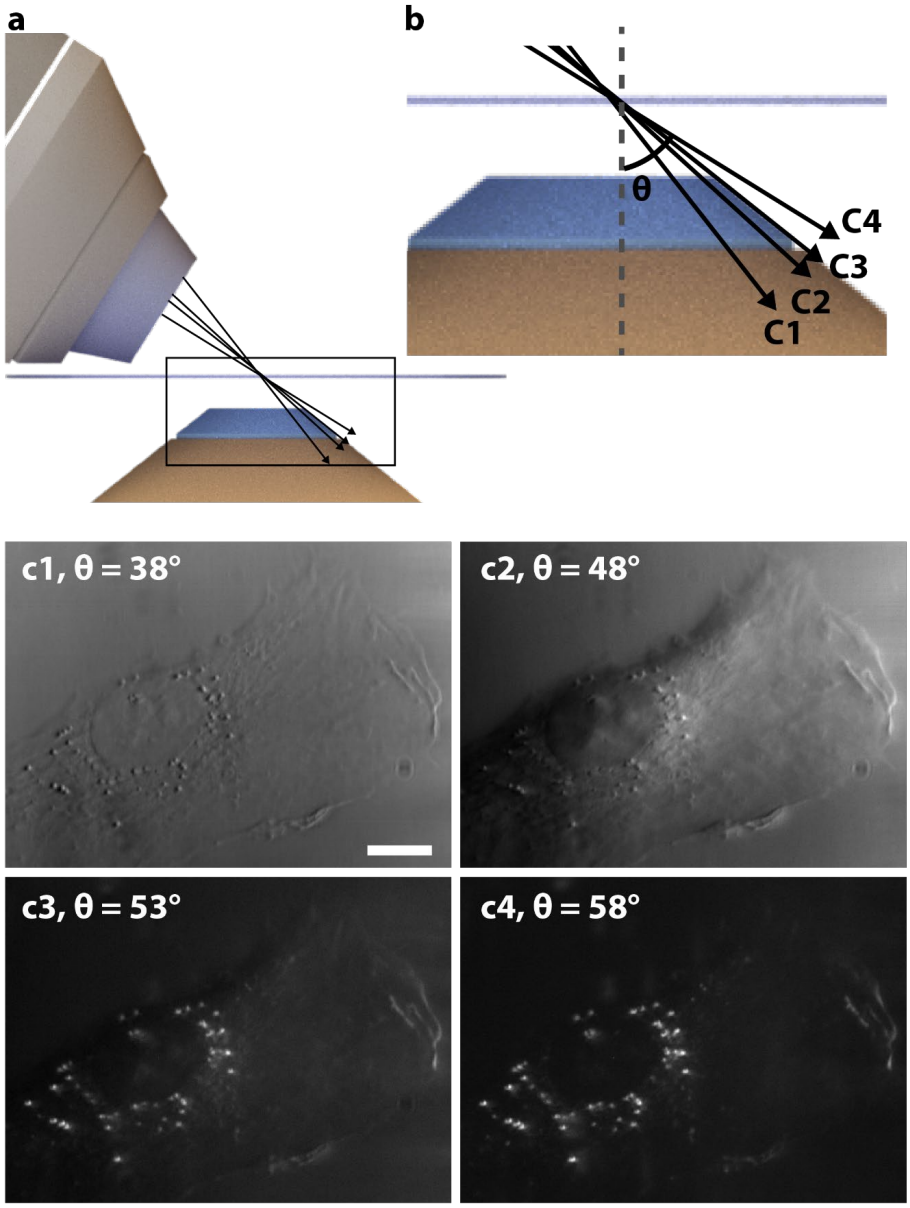

Fig. S10. Oblique illumination contrast vs. illumination angle. (a) Excitation objective provides illumination oblique at a single angle to the axis of the inverted objective used for imaging. **(b)** Enlarged view showing four angles (θ) ranging from all ballistic light collected (c1) to all ballistic light rejected (c4). Corresponding images of a cell show contrast ranging from brightfield (c1, θ = 38°), to DIC-mimicking (c2, θ = 48°), to progressively darker field (c3, θ = 53°, c4, θ = 58°). Scale bar, 5 μm.

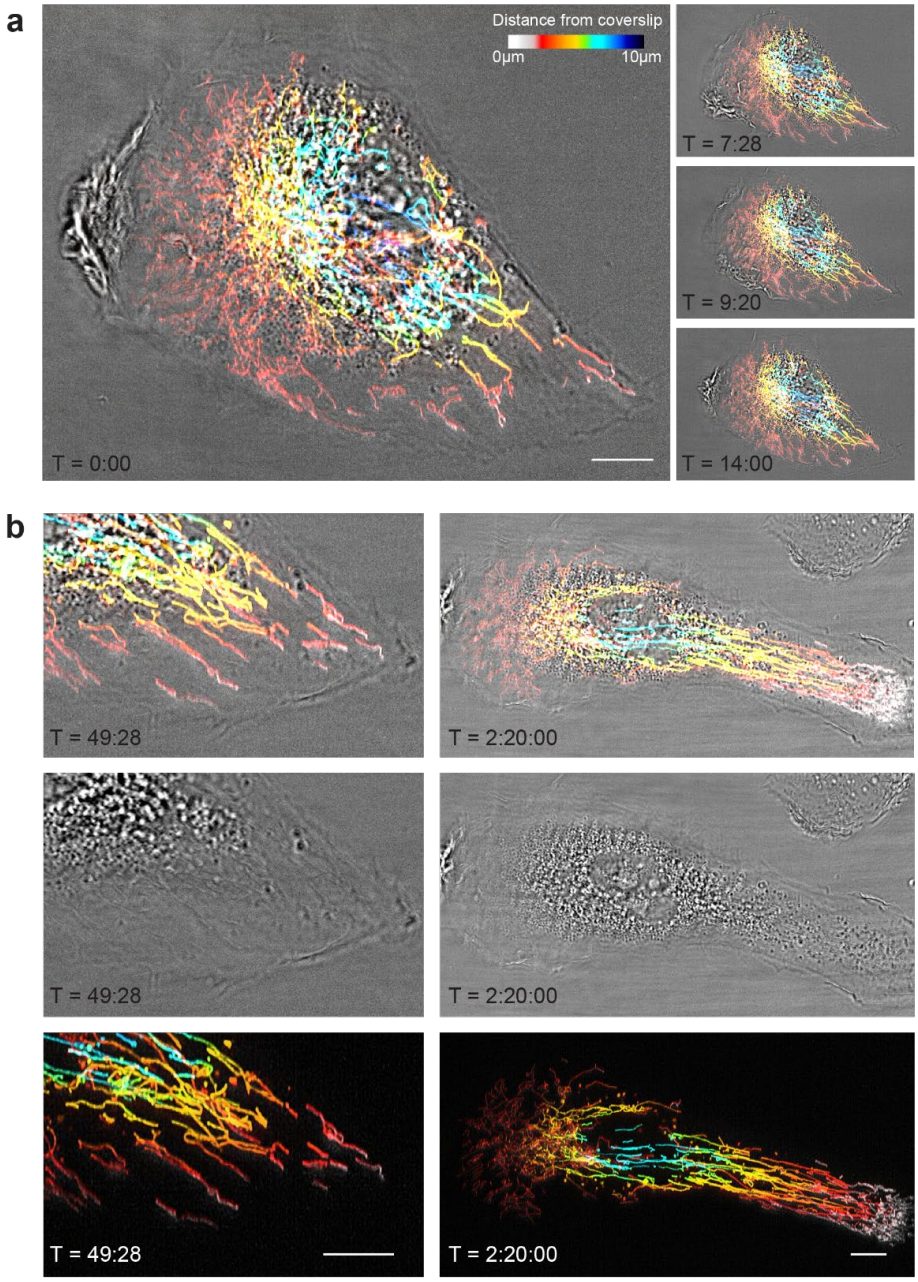

Fig. S11. Correlative LLS and OI imaging of a migrating hTERT-RPE1 cell. (a) Overlay of correlative imaging highlights both mitochondria (COX8a-StayGold imaged with LLS, color coded by height) and overall cell morphology (OI). Scale bar, 5 µm. **(b)** Overlay (top), OI (middle), and LLS fluorescence (bottom) at two time points highlight the leading edge during migration and the exclusion of mitochondria from the cellular periphery. Scale bar, 5 µm. See Movie S4.

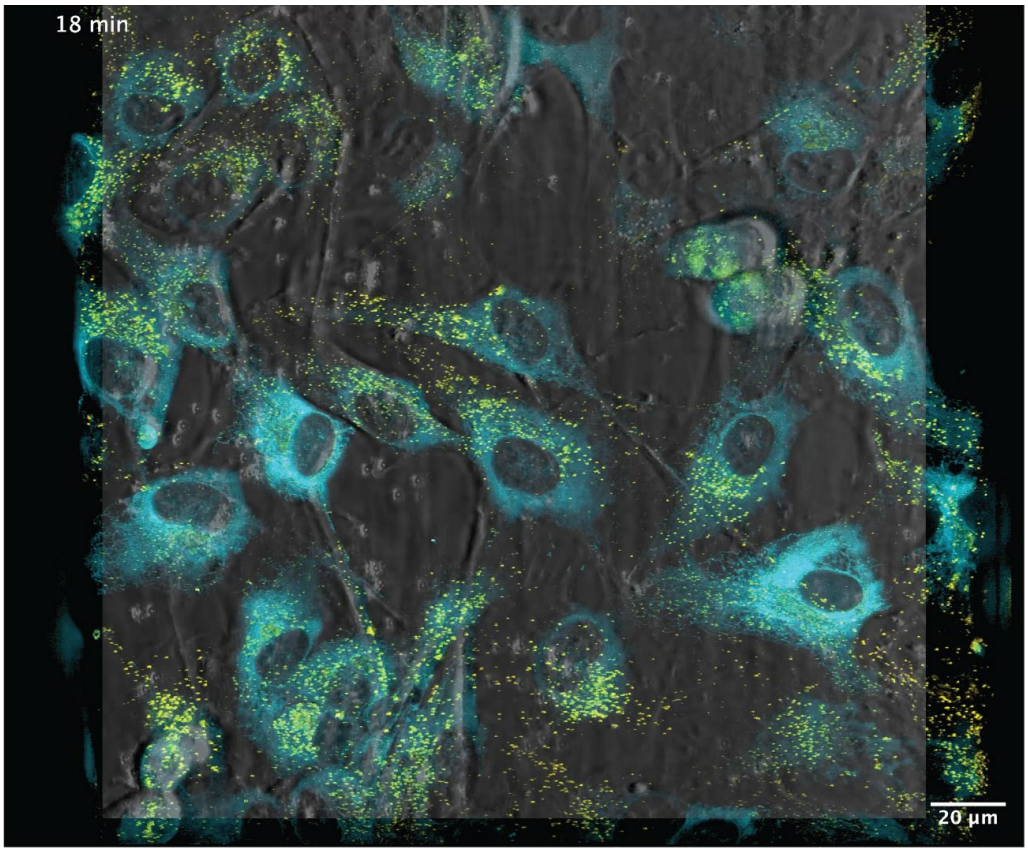

Fig. S12. Large FOV correlative LLS and OI imaging. Overlay of LLS and OI imaging of hTERT-RPE1 cells co-expressing ER (calreticulin-StayGold, cyan) and a membrane-bound Golgi glycoprotein (β4Gal-T1-HaloTag/JFX549, light yellow) over a 226 x 226 x 10 μm^3 volume. Scale bar, 20 µm. See Movie S4.

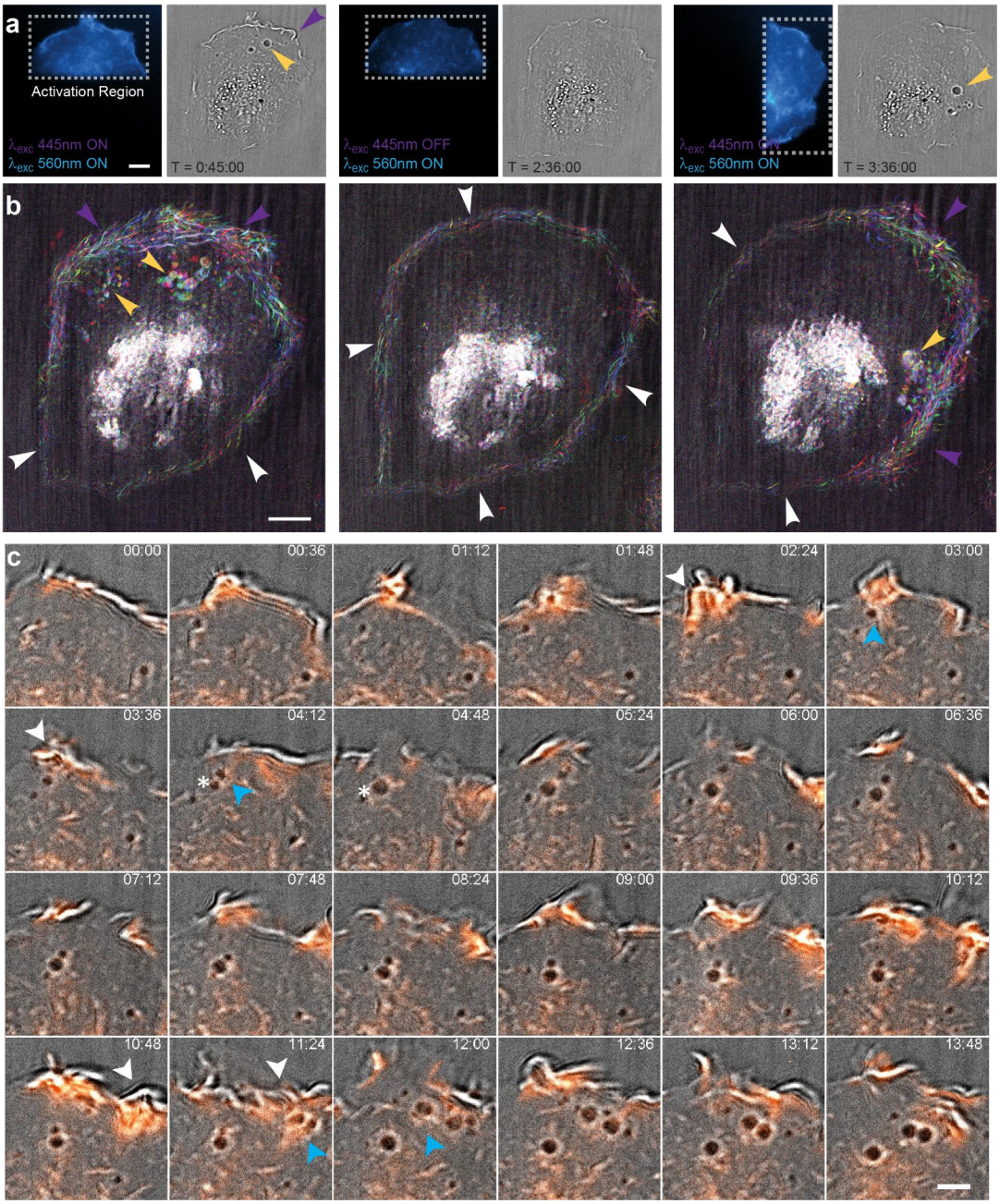

Fig. S13. Optogenetic induced macropinocytosis with correlative oblique illumination. (a) Localized optogenetic activation of PA-Rac1-mCherry (blue, left panel in each example) induces the formation of macropinosomes (yellow arrows) after membrane ruffling (purple arrow) as seen by OI. Scale bar, 10 μm. **(b)** Color-coded time projections highlight induced ruffling (purple arrows) and macropinosome formation (yellow arrows) within the photoactivated areas in (a). White arrows indicate background ruffling in non-activated regions. Scale bar, 10 μm. **(c)** Time series of macropinosome formation using interleaved photoactivation, fluorescence (orange), and OI (gray) modalities. White arrows indicate membrane ruffles which collapse to form macropinosomes indicated by blue arrows. Asterisk indicates a site of vesicle fusion. Scale bar, 5 μm. See Movie S5.

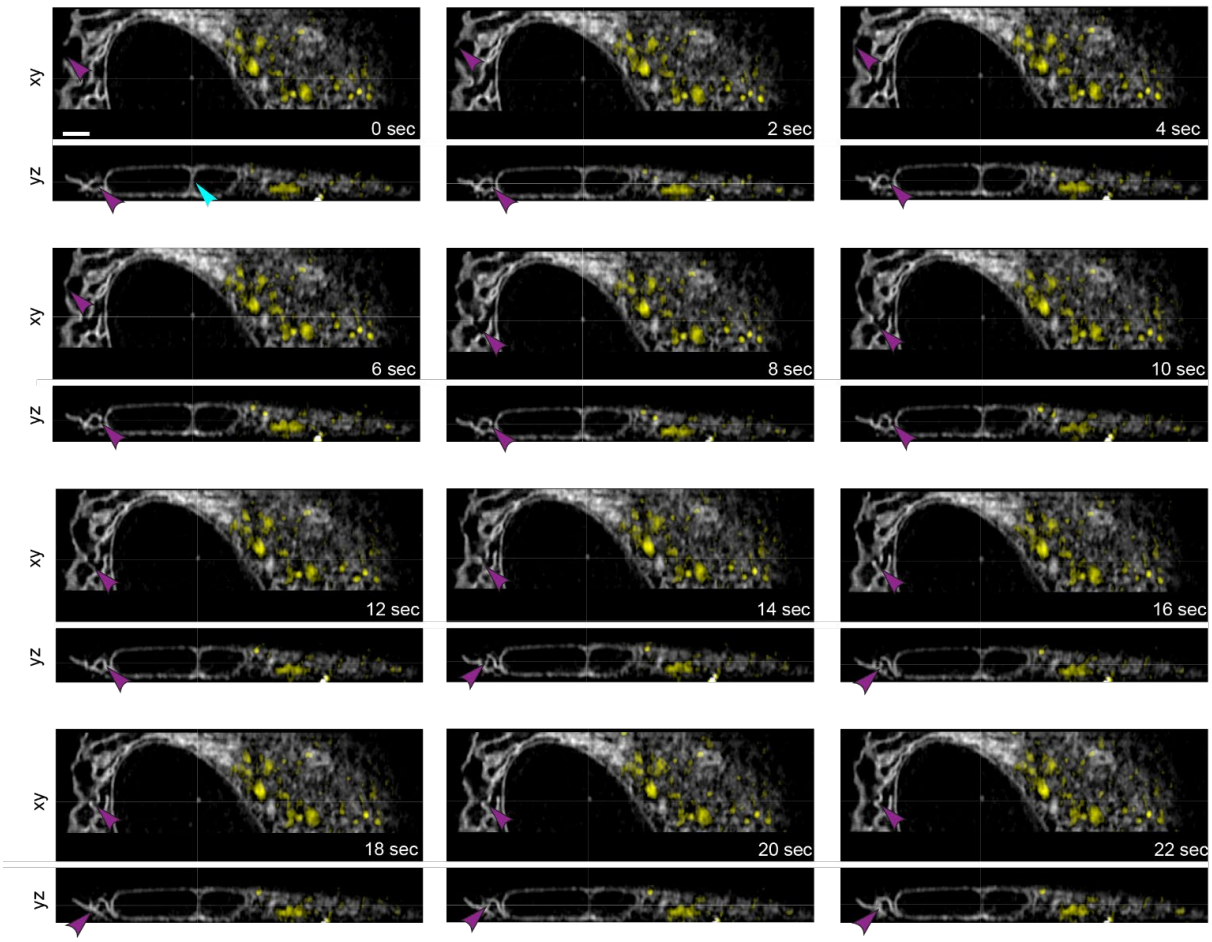

Fig. S14. Rapid 4D SR imaging of subcellular dynamics. Time-lapse movie of a live hTERT-RPE1 cell expressing ER (calreticulin-StayGold, gray) and Golgi (β4Gal-T1-HaloTag/JFX549, yellow) markers imaged every 2 seconds by LLS-SIM. Magenta arrows highlight dynamic ER remodeling events. Cyan arrows highlight an ER tunnel passing through the cell nucleus. Images show xy and yz orthoslices. Scale bar, 4 μm. See Movie S6.

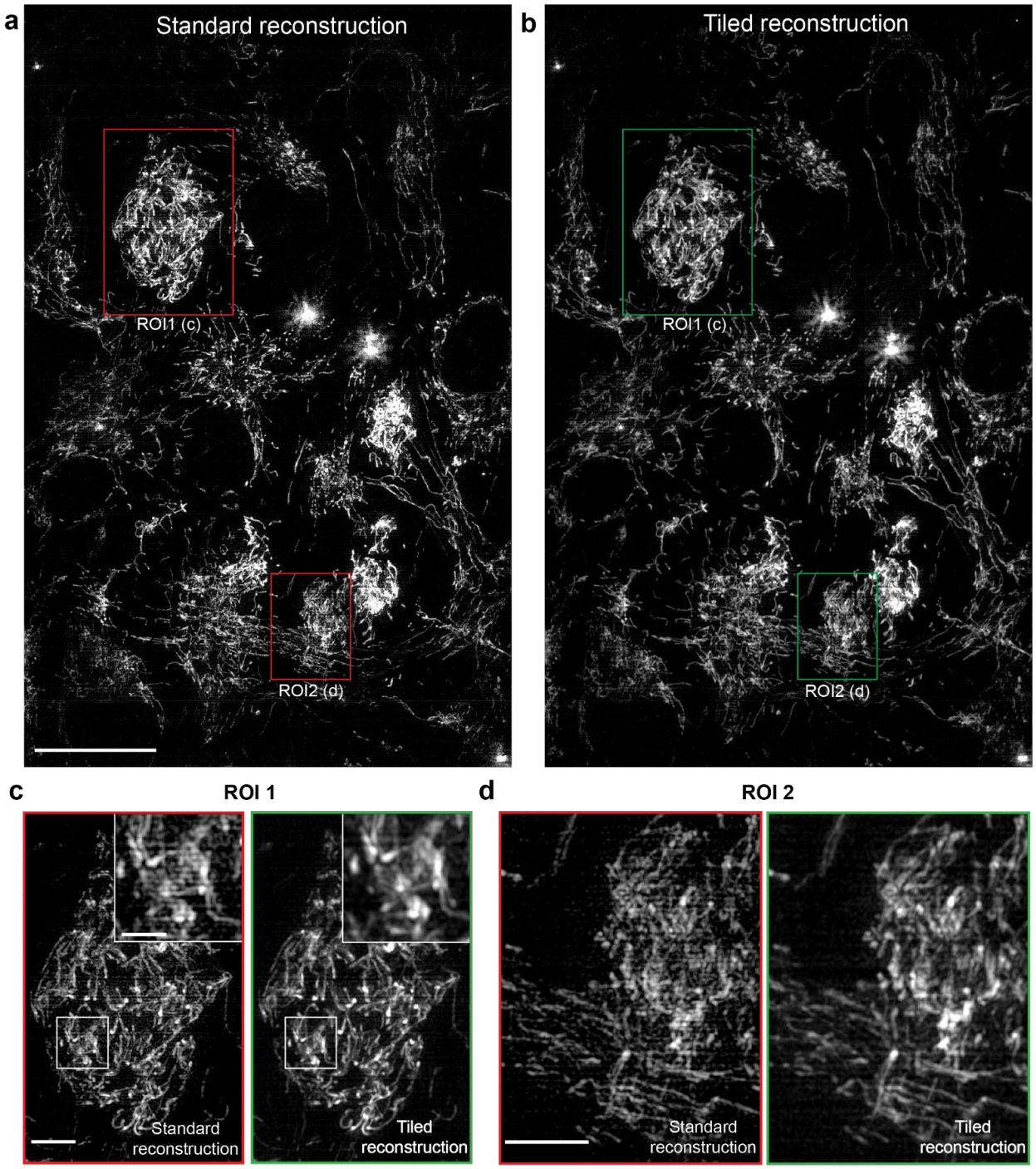

Fig. S15. Tiled SIM reconstruction reduces artifacts. (a) xy MIP from a single 3D-SIM reconstruction covering a large FOV of live hTERT-RPE1 cells expressing the mitochondria marker COX8a-StayGold. **(b)** xy MIP from a tiled 3D-SIM reconstruction of the same volume using a 128 x 128 pixel tiles across 40 z planes, each reconstructed independently, followed by stitching based on a 32 pixel overlap between adjacent tiles. Scale bar, 25 μm. **(c)** Comparison in ROI1 reveals residual grating artifacts for the standard reconstruction (left and left inset) not apparent with the tiled approach. Scale bars, 5 μm and 2 μm (inset). **(d)** Similar comparison for ROI2. See Movie S7.

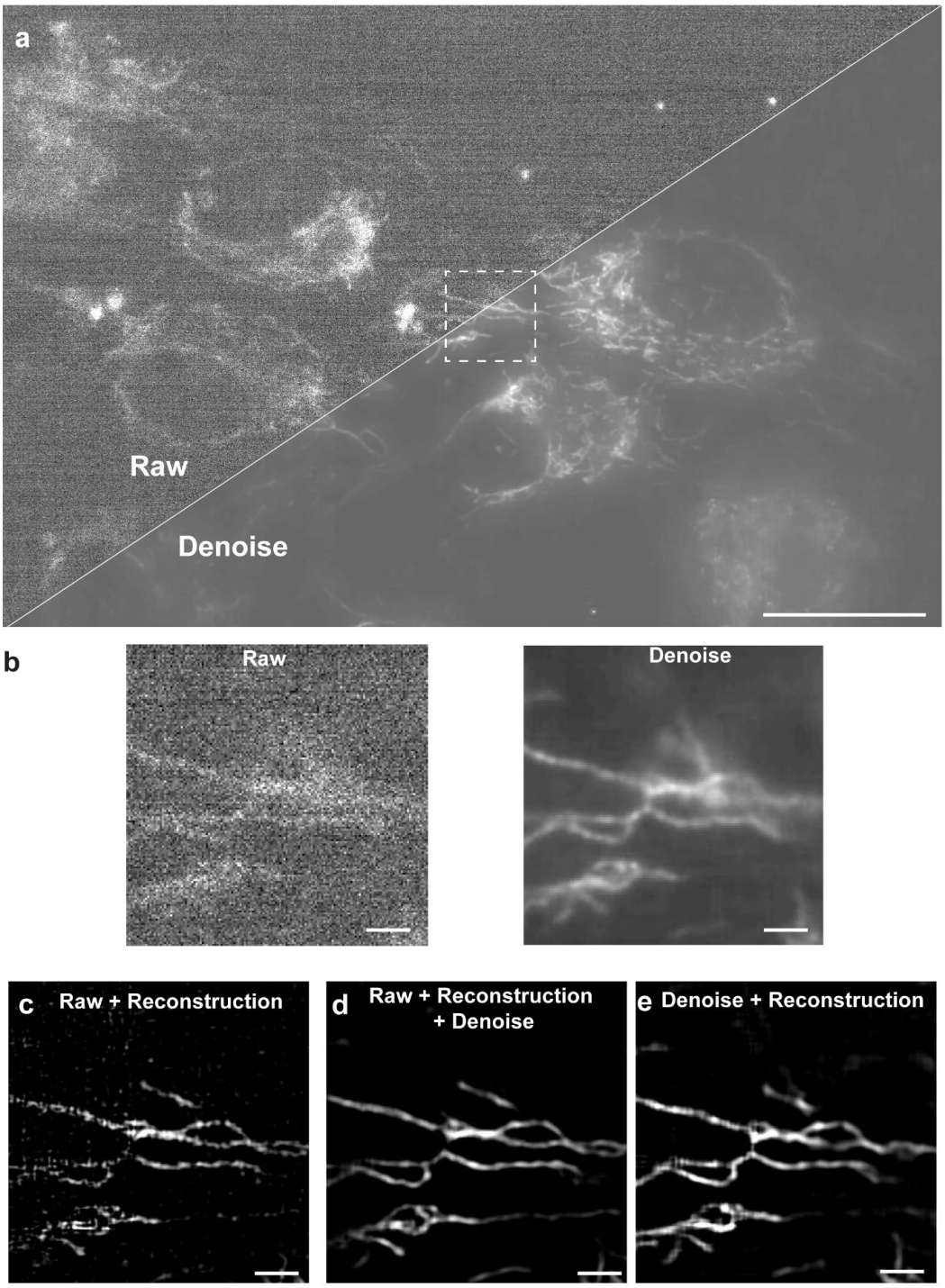

Fig. S16. Denoising strategies for reconstructing low SNR 3D-SIM data. (a) xy MIP of a 3D-SIM single raw image of live hTERT-RPE1 cells expressing mitochondria marker (COX8a-StayGold) without and with denoising[20] applied. Scale bar, 25 μm. **(b)** Zoomed view of the boxed region in (a), showing reduction of noise at right. **(c-e)** 3D SIM reconstruction of the region in (b) under three scenarios: (c) reconstruction with raw data; (d) denoising before reconstruction; and (e) denoising after reconstruction. Option (e) is preferred to prevent loss of high spatial frequencies when denoising before reconstruction. Scale bar for (b-e), 2 μm.

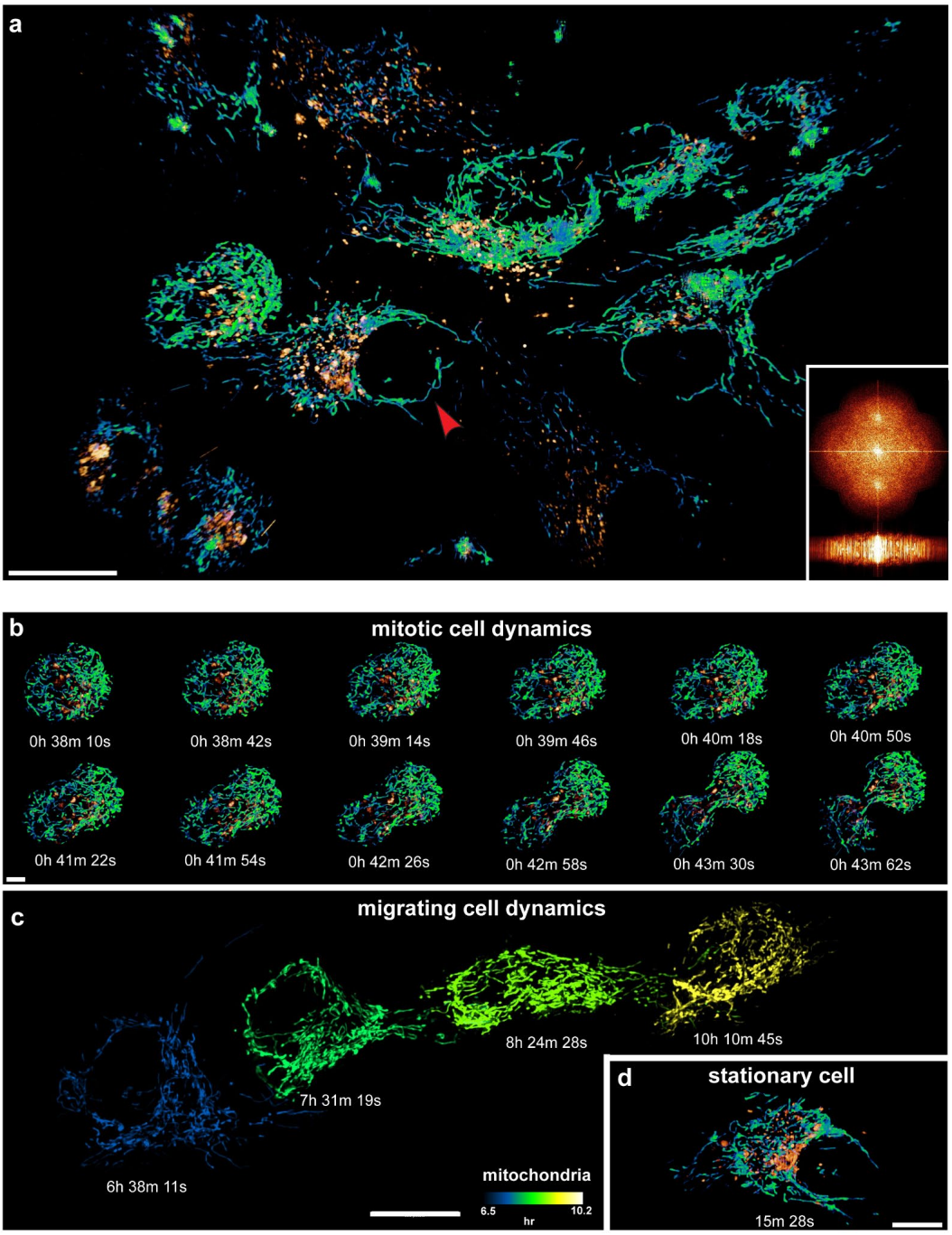

Fig. S17. Extended live-cell 3D-SIM time lapse imaging using optimized acquisition and denoising. Long-term (11 hours, 1200 time points) dual-color 3D-SIM imaging achieved by: i) using two rather three grating illumination orientations (0°and 90°) per z-plane; and ii) reduced laser power / exposure time, made possible by post-acquisition denoising. **(a)** xy MIP at one time point showing live hTERT-RPE1 cells co-expressing mitochondrial (COX8a-StayGold, green-blue) and Golgi (β4Gal-T1-HaloTag-JFX549, orange) markers. Inset: xy/yz OTFs from the mitochondria channel shows extension of the support. Scale bar, 20 μm. **(b)** A full cell division cycle recorded over 160 sec at 32 sec intervals. Scale bar, 5 μm. **(c)** Cell migration over ~3.5 hours. Scale bar, 15 μm. **(d)** A stationary cell, marked by a red arrowhead in (a). Scale bar, 10 μm. See Movie S7.

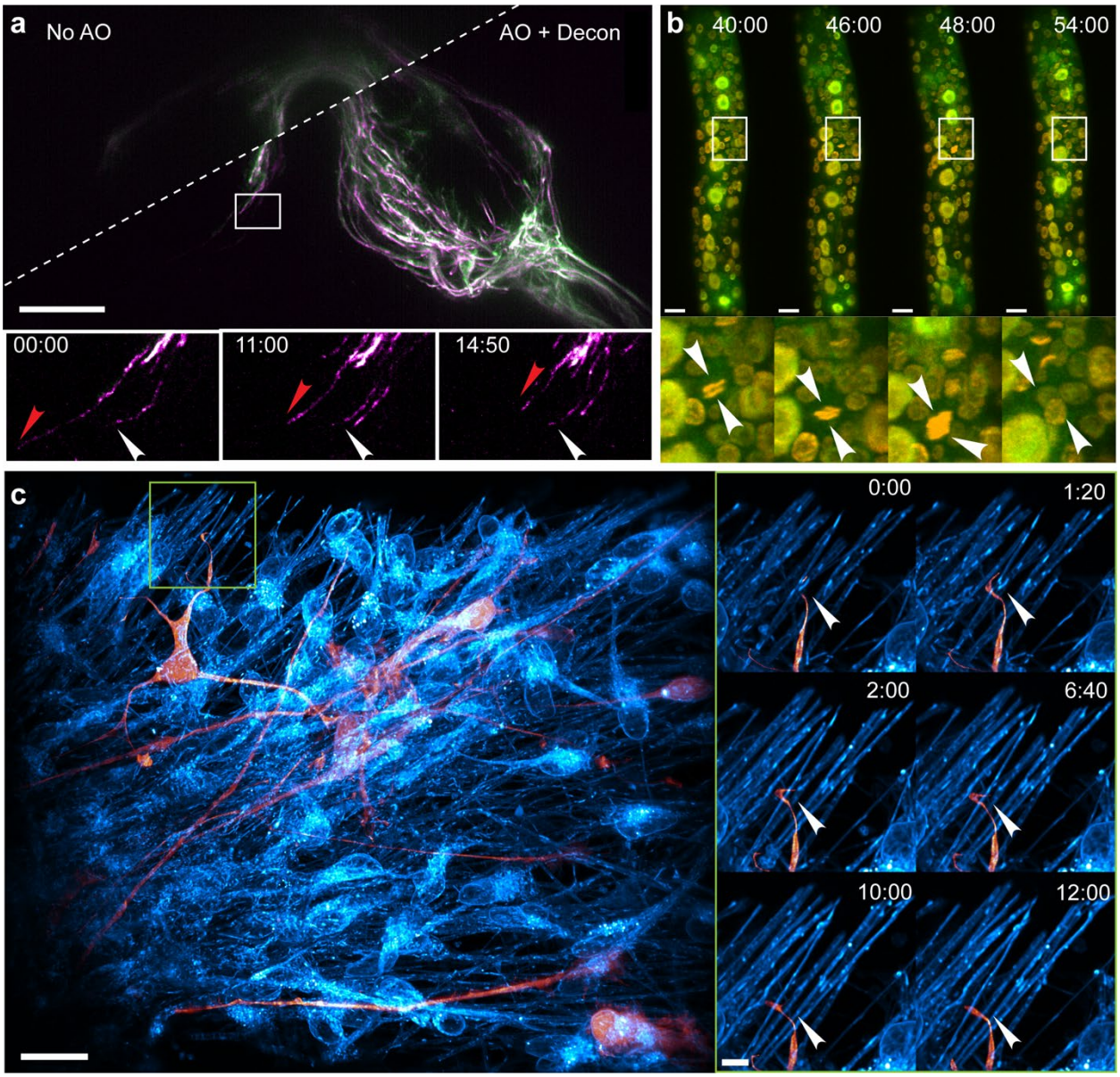

Fig. S18. Application of AO-LLSM to other model organisms. (a) *Drosophila* olfactory receptor neuron axons in the antenna lobe during the target selection process, showing axons expressing membrane marker (mCD8-GFP, magenta) and microtubule marker (Halo7-EB1, green) before (top left) and after AO (bottom right). Inset: Zoom-in view of the white box showing the microtubule-rich exploring branches dynamics after AO correction. White and red arrows highlighting dynamically extending and retracting branches, respectively. Scale bar, 20 μm. **(b)** Top: Time series showing an L3 stage *C. elegans* larva co-expressing a CDK1/2 activity sensor (green) and histone (orange). Bottom: Division (white arrows) of a single somatic gonad cell -- the CDK1/2 activity sensor is excluded from the nucleus during mitosis (40, 46, and 48 mins) but re-localizes in the daughter cells afterwards (54 mins). Scale bar, 10 μm. **(c)** Left: Neuronal and mitochondrial dynamics (Movie S13) in human iPSC-derived brain organoids with global mitochondria label mitotracker (cyan) and cytoplasmic-mGFP (orange) expressed in ~20% of all cells. Scale bar, 20 μm. Right: a Neuronal projection in the boxed region dynamically extending to probe its environment. Scale bar, 5 μm. Time stamps correspond to minutes:seconds.

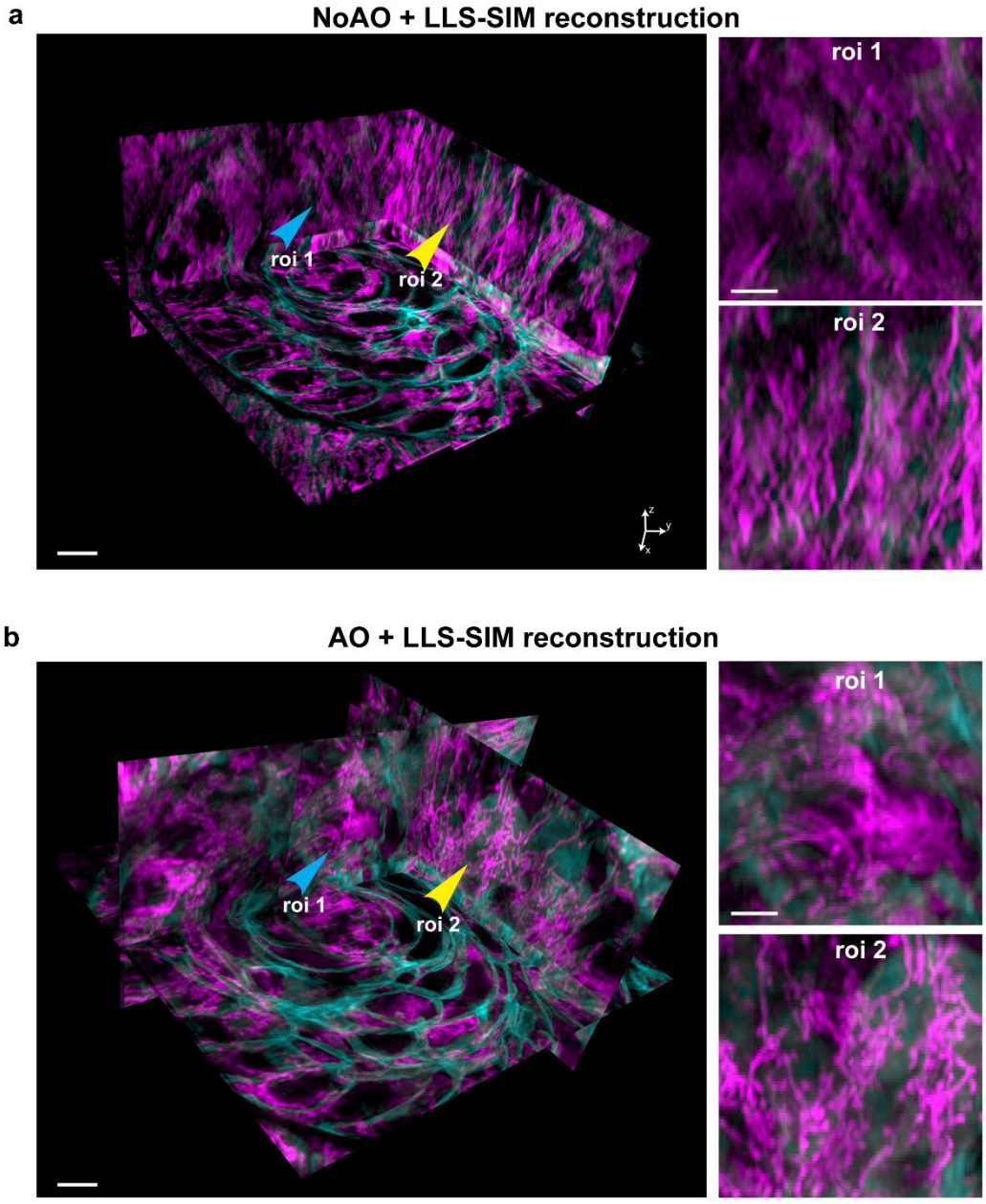

Fig. S19. AO correction is essential for accurate LLS-SIM reconstruction in multicellular environments. LLS-SIM reconstruction of mitochondria (magneta) and plasma membranes (cyan) without **(a)** and with **(b)** AO in the zebrafish eye, in the same region as Fig. 5b. Axial features (cyan and yellow arrows) are particularly distorted before correction. Scale bar, 5 μm (orthoslice view) and 2 μm (zoomed view).

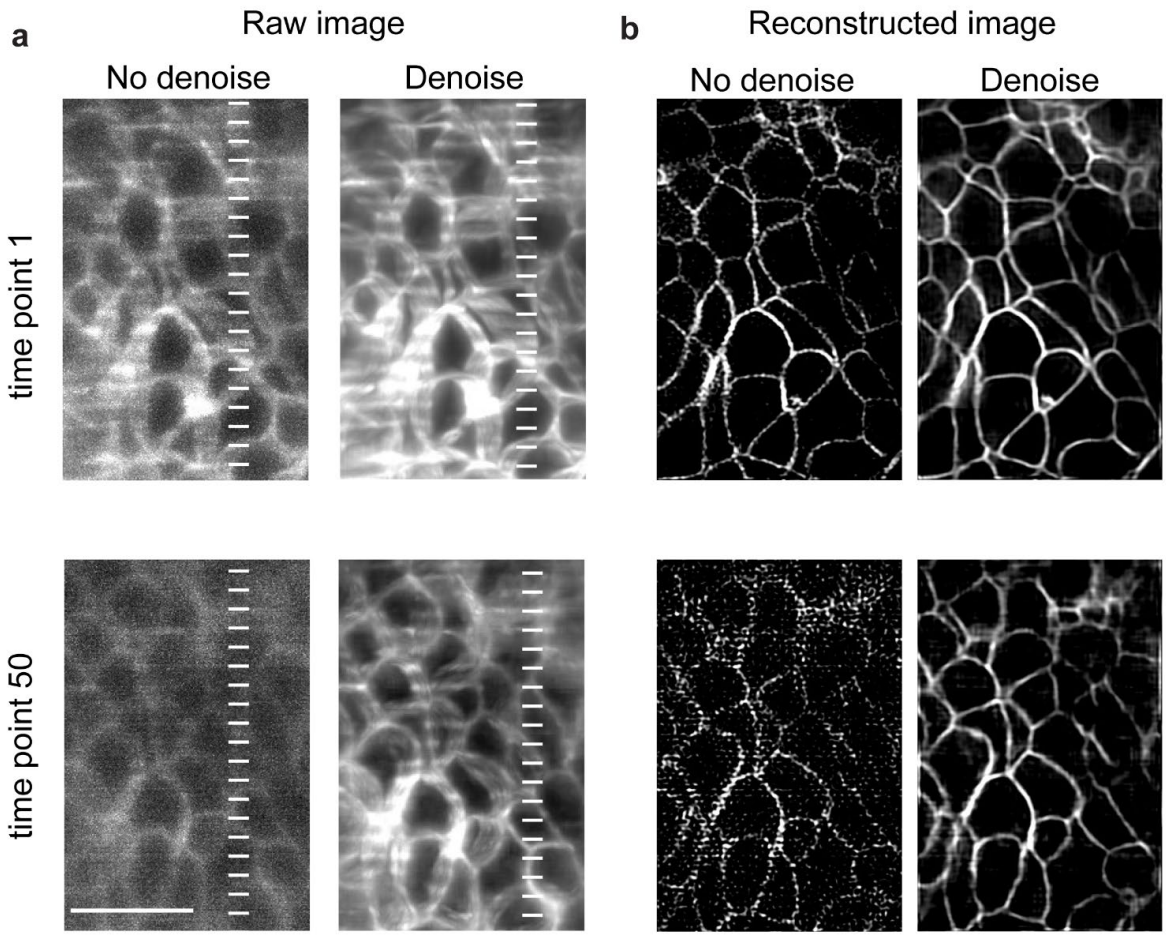

Fig. S20. Denoising improves reconstruction of low SNR time-lapse AO-LLS-SIM data. (a) 5 μm MIP slab of a single low SNR raw volume at a fixed phase of LLS-SIM excitation, before and after denoising. **(b)** Corresponding LLS-SIM reconstructions. Denoising extends the photon budget for the imaging and becomes critical for accurate reconstruction at later time points. Scale bar, 10 μm.

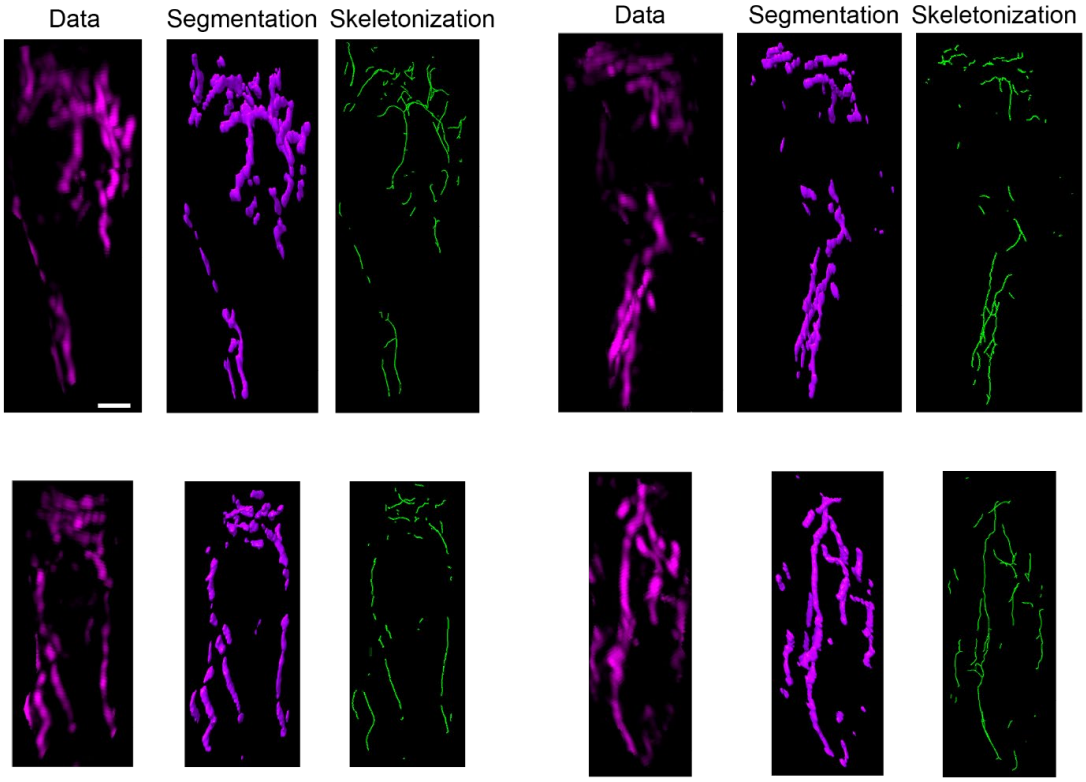

Fig. S21. Processing steps for analyzing mitochondrial network morphology. Four examples that illustrate the analysis pipeline applied to mitochondria within a single cell segmented from zebrafish tissue. Left: Raw fluorescence imaging data (magenta). Middle: 3D segmentation identifying mitochondrial voxels. Right: Skeletonization representing the mitochondrial medial axis (green). Scale bar, 2 μm.

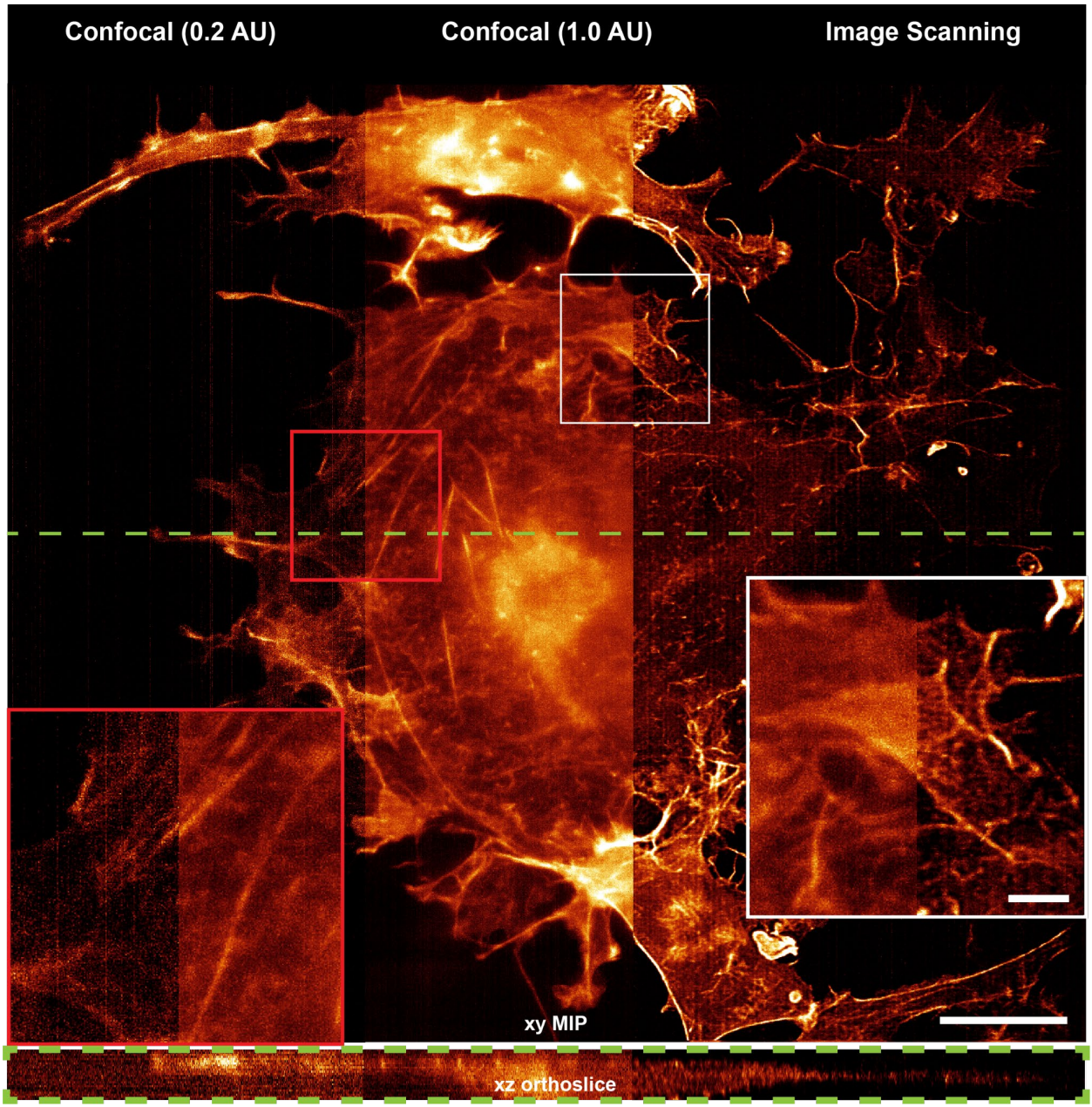

Fig. S22. Comparison of linescan confocal and image scanning microscopy (ISM). 3D imaging of COS7 cells expressing the actin marker LifeAct-mCherry shows ISM resolution comparable to linescan confocal imaging with a tightly closed collection slit (0.2 Airy Unit, AU width) while maintaining the higher SNR typical of a larger slit (1.0 AU). Only the actin channel is shown here. See Movie S15 for two-color (actin and microtubule) imaging. Scale bar, 10 μm.

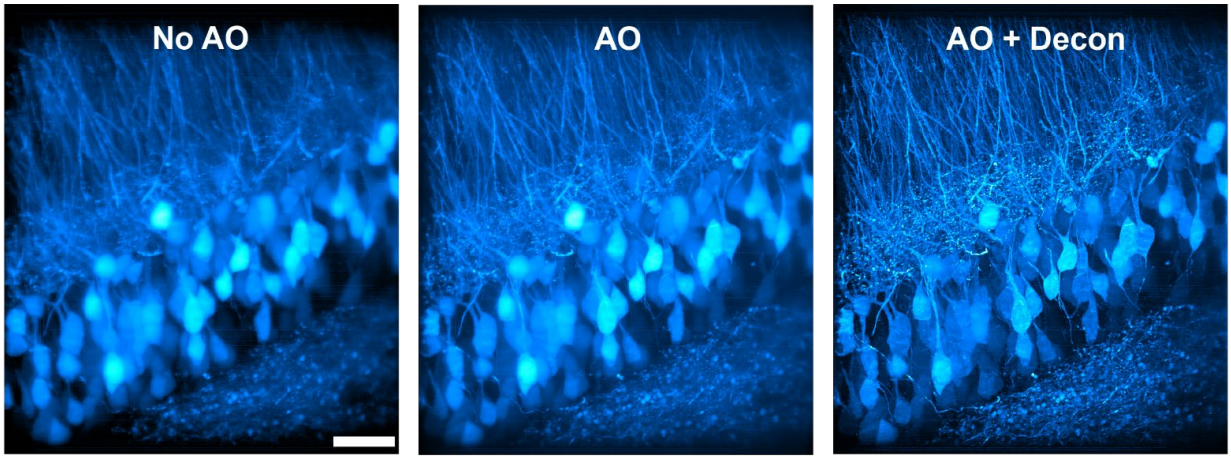

Fig. S23. **AO improvement for two-photon Bessel light sheet imaging in thick brain slices**. Comparison of images from a 300-μm thick acute brain slice (3-month-old Thy1-GFP-M mouse) acquired using a two-photon Bessel light sheet (NA = 0.55/0.58) without AO correction (left), with AO correction (middle), and with AO correction plus deconvolution (right). Scale bar, 20 μm.

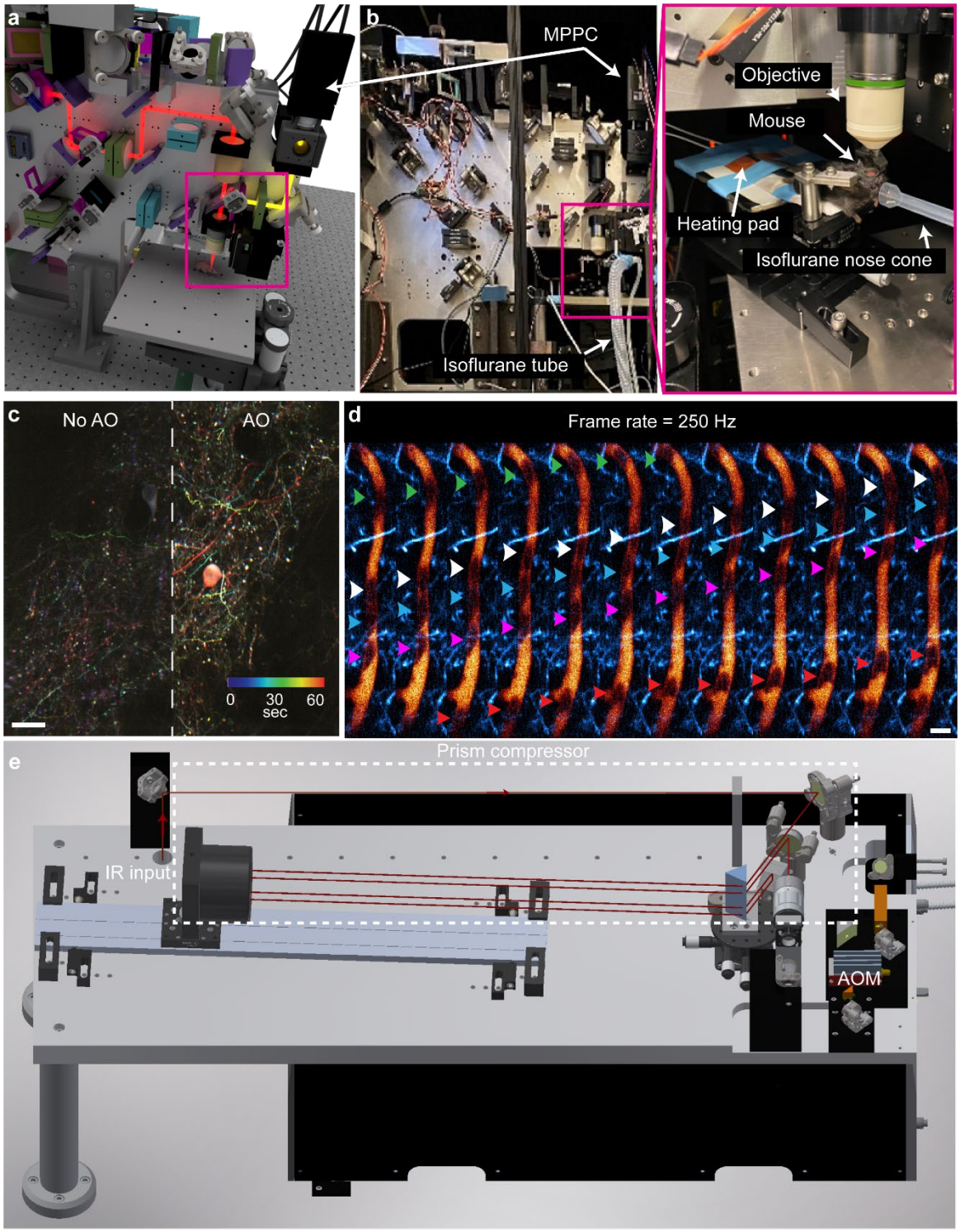

Fig. S24. AO-TPM enables deep functional imaging in live mice. (a) 3D model of the upright MOSAIC work area for *in vivo* AO-TPM in mice. **(b)** Corresponding photograph with magnified view of a mouse in place for imaging. **(c)** Improved SNR for detection of GCaMP7s transients with (right) and without (left) AO correction. Scale bar, 20 μm. **(d)** Erythrocyte transport in a capillary imaged at 250 Hz using resonant scanning AO-TPM. Scale bar, 5 μm. **(e)** 3D model shows the TP femtosecond laser beam path, including the prism compressor for group velocity dispersion compensation and the acousto-optic modulator for output power control.

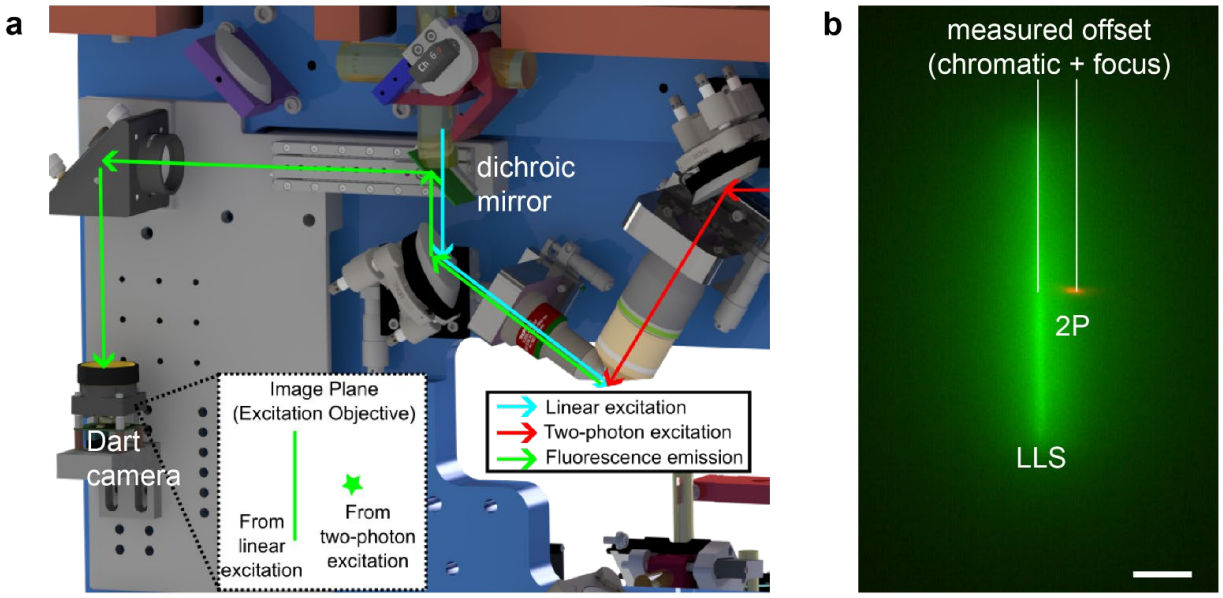

Fig. S25. Autofocus (AF) module for continuous axial alignment of light sheet to detection focal plane. (a) 3D model and optical path of the AF module design integrated into MOSAIC. **(b)** Image from the AF detection camera showing overlaid fluorescence signals generated simultaneously by the LLS (green) from the excitation objective and TPE focus (red) from the detection one. Scale bar, 10 μm.

Movie Captions

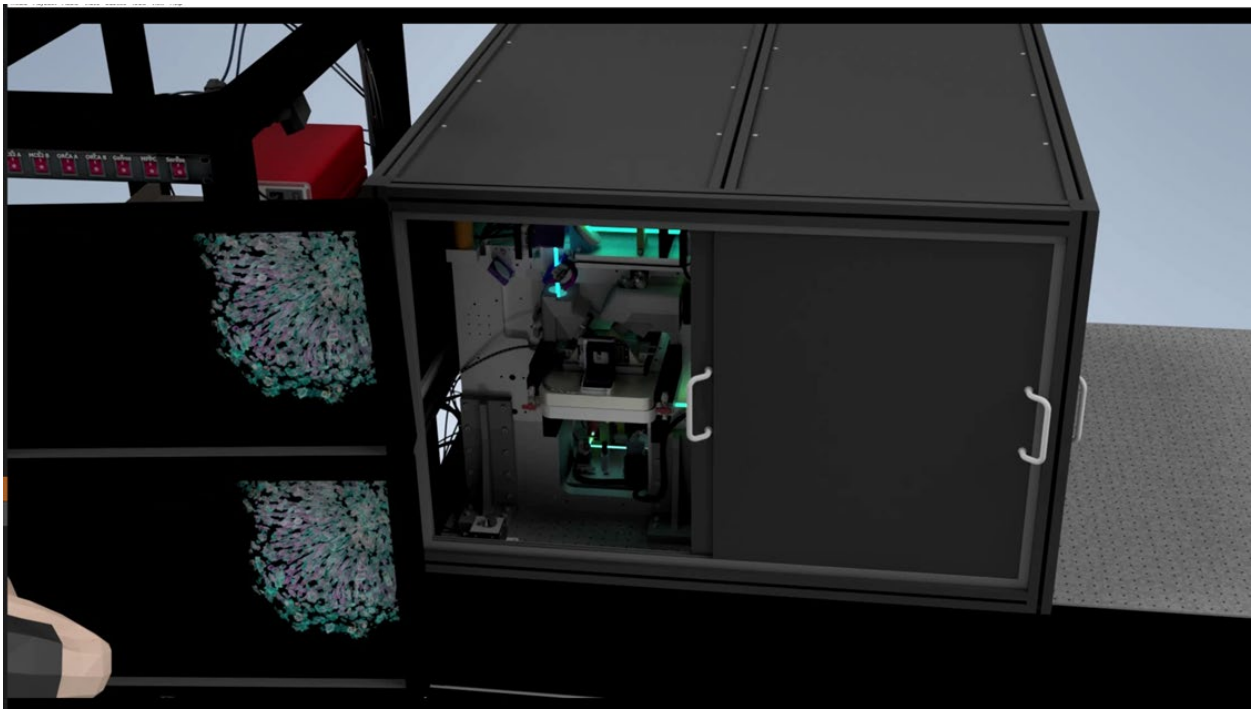

Movie S1. **3D CAD model of the MOSAIC system.** The animation shows the main microscope assembly, enclosure (case), optical table, electronics, and control/acquisition workstation.

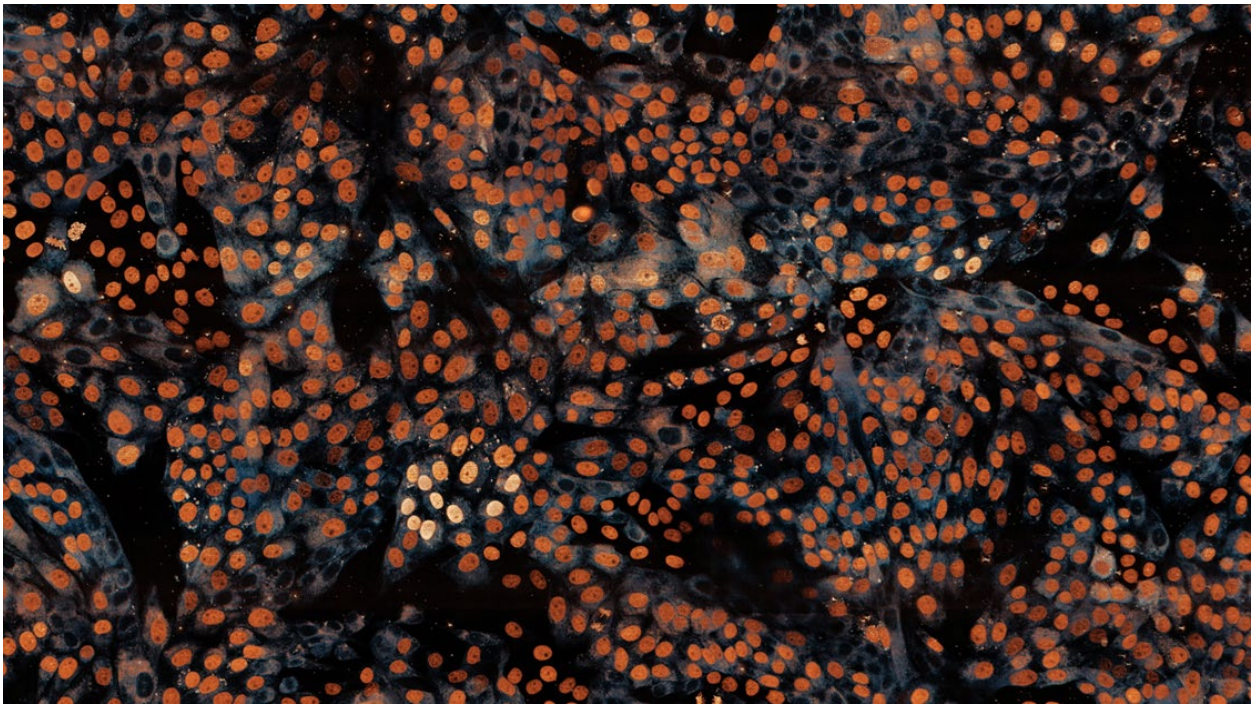

Movie S2. **Long-term, large FOV 3D live imaging of LLC-PK1 cells via LLSM.** Time-lapse sequence acquired over 24 hours (989 time points at 90 sec intervals). Visualization shows endoplasmic reticulum (Calnexin-mEmerald, gray) and nuclei (H2B-mCherry, orange). The imaged volume at each time point is 1000 x 750 x 10 μm^3.

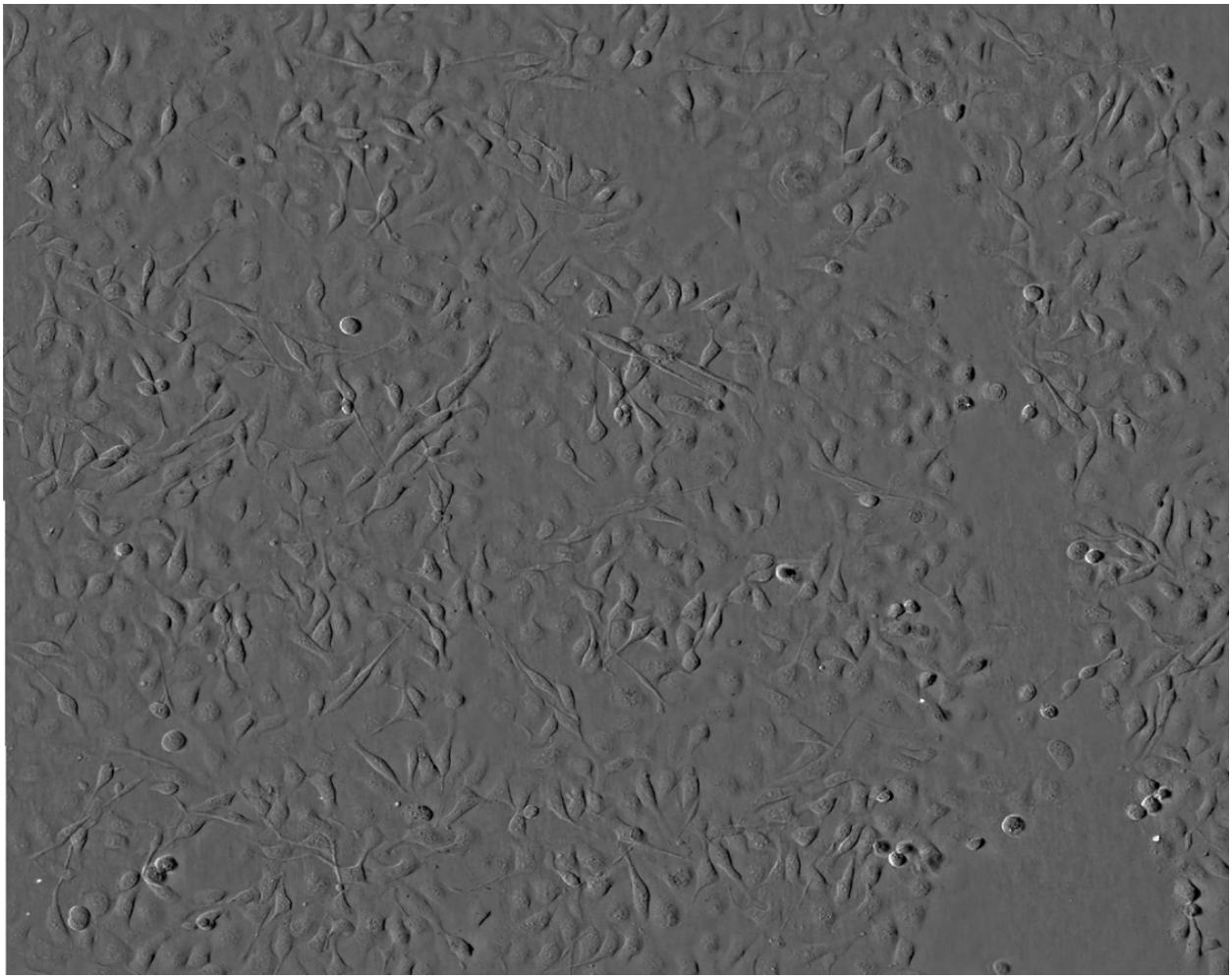

Movie S3. **Monitoring large-scale HeLa cell dynamics using label-free oblique illumination.** Time lapse movie covering a 1218 x 725 μm^2 FOV consisting of 1000 frames at 1 sec intervals (t~16.7 minutes total).

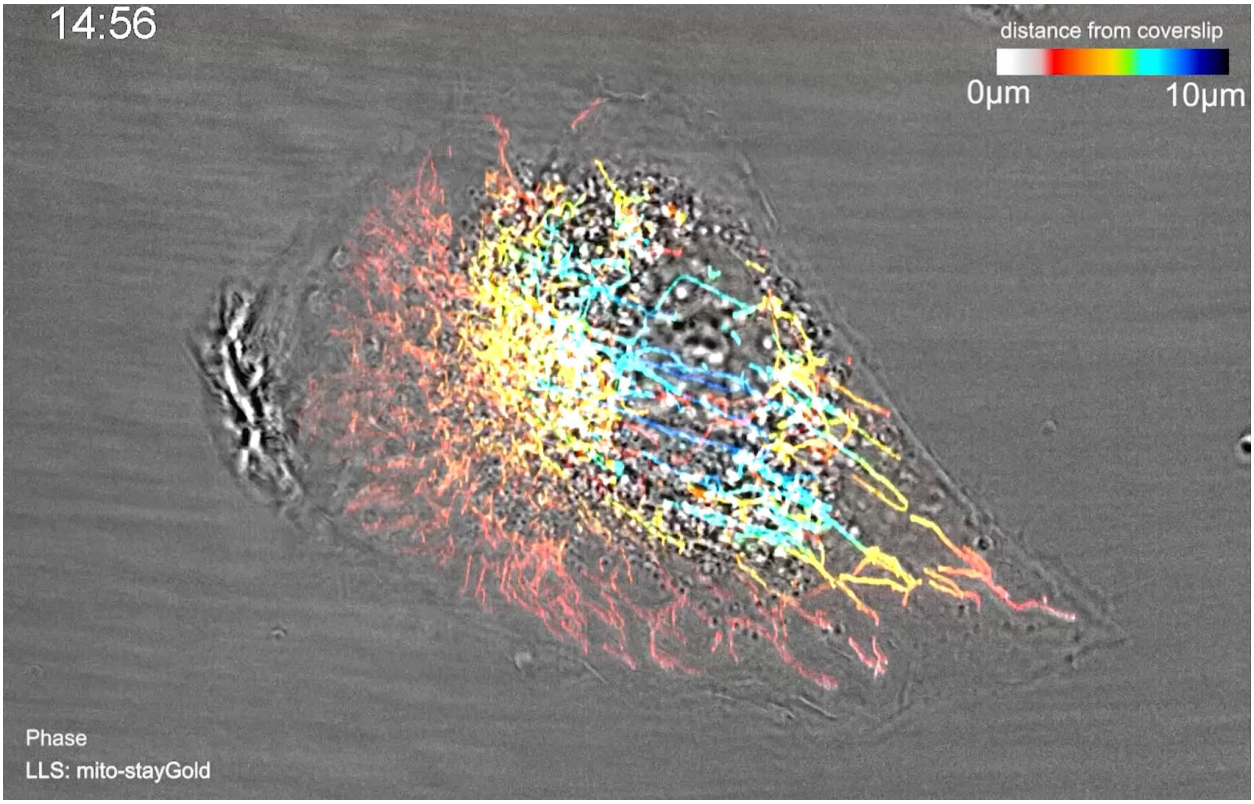

Movie S4. Correlative LLS fluorescence and label-free OI imaging of live hTERT-RPE1 cells. Part 1: Mitochondrial redistribution during migration of a single cell over 2.2 hours (145 time points, 56 sec intervals). Mitochondria (COX8a-StayGold via LLS) color-coded by height and correlated with cell morphology via OI (gray). Part 2: ER (cyan) and Golgi (yellow) dynamics across a large cell population covering 226 x 226 x 10 μm^3 over 9 hours (2000 time points at 16.3 sec intervals), with OI (gray) for label free context.

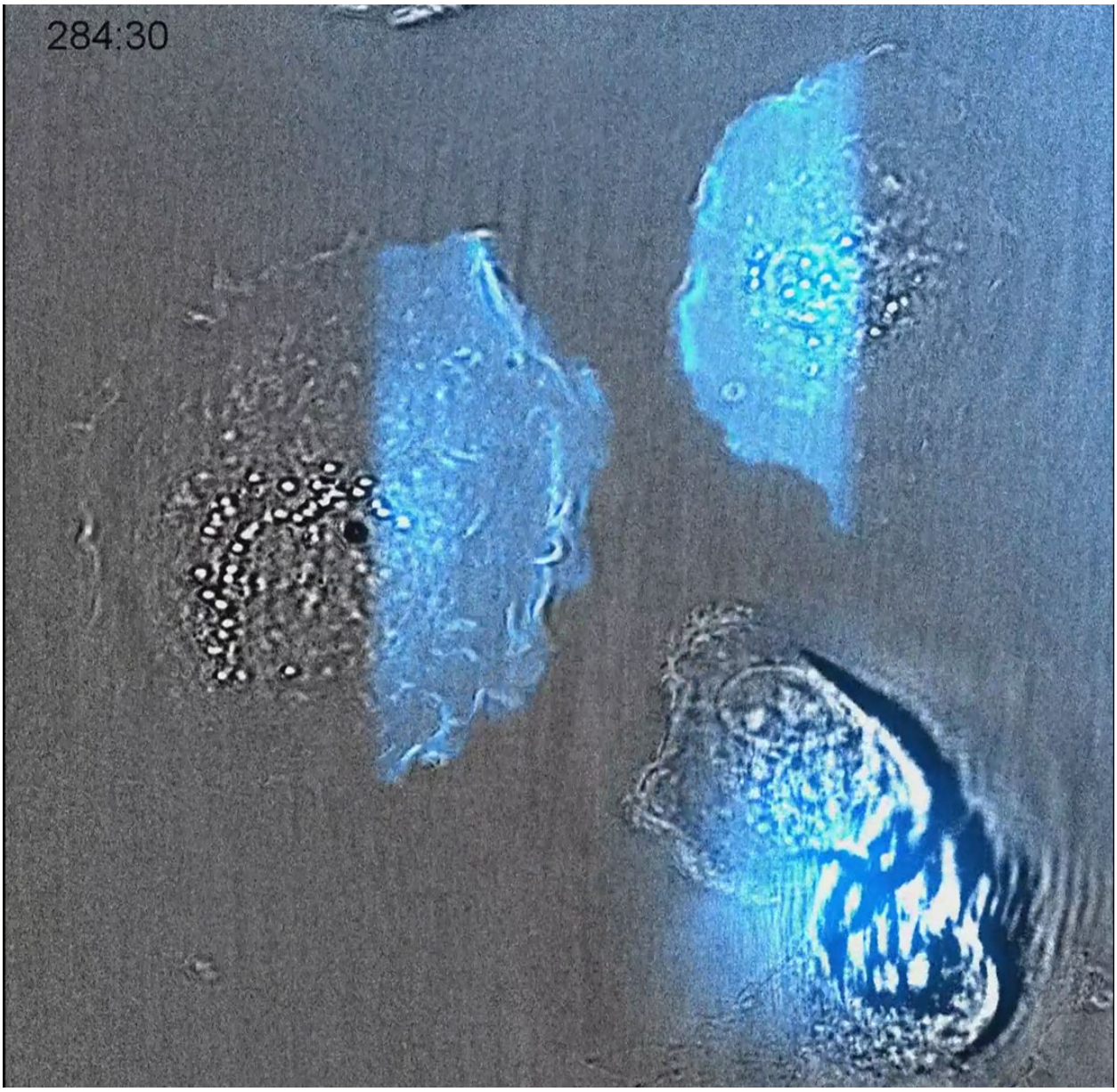

Movie S5. **Visualizing optogenetically induced macropinocytosis with correlative oblique illumination.** Membrane ruffling and macropinocytosis induced in hTert-RPE1 cells expressing PA-Rac1-mCherry by point scanning excitation at 445 nm. Activation triggers dynamic membrane ruffling and the formation of macropinosomes.

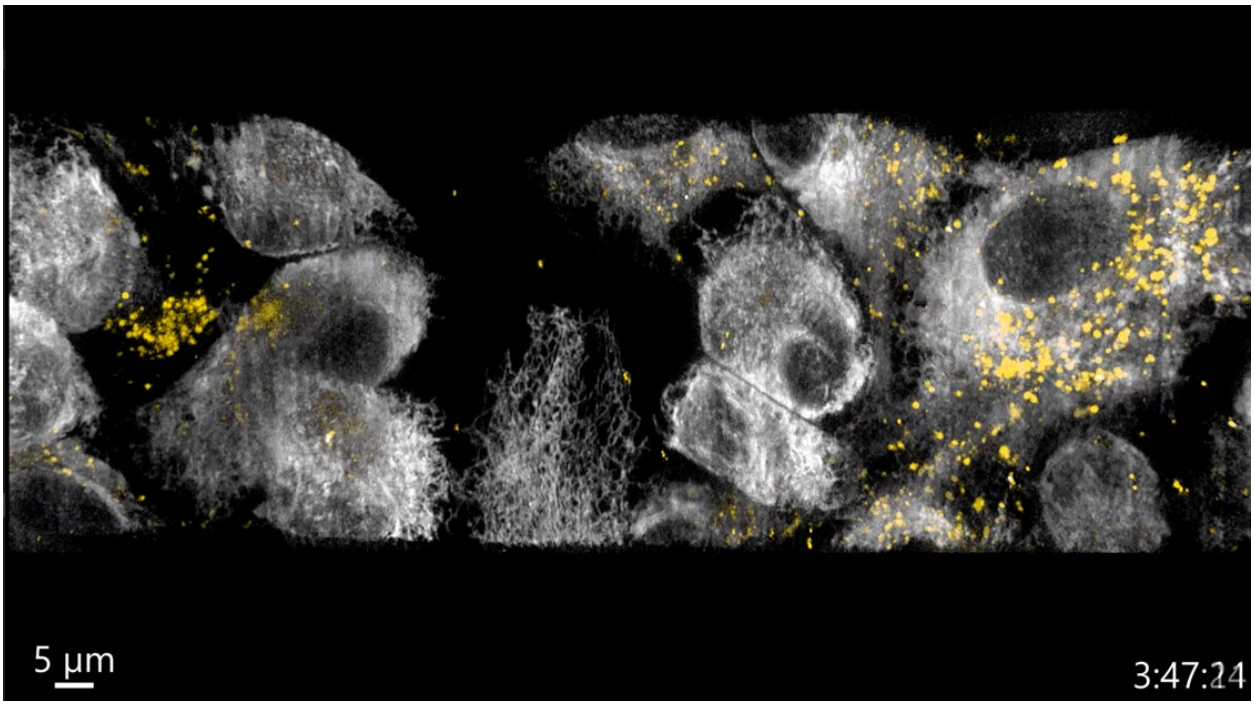

Movie S6. **3D LLS-SIM imaging of cultured hTERT-RPE1 cells.** Live hTERT-RPE1 cells expressing ER (calreticulin-StayGold, gray) and Golgi (β4Gal-HaloTag9-JFX549, yellow) markers imaged via 3D LLS-SIM. Part A: Overall dynamics across a 188 x 50 x 10 μm^3 FOV over ~4.17 hours (1500 time points, 10 sec intervals). Part B: Faster dynamics focused on two cells imaged over ~50 minutes (1500 time points, 2 sec intervals).

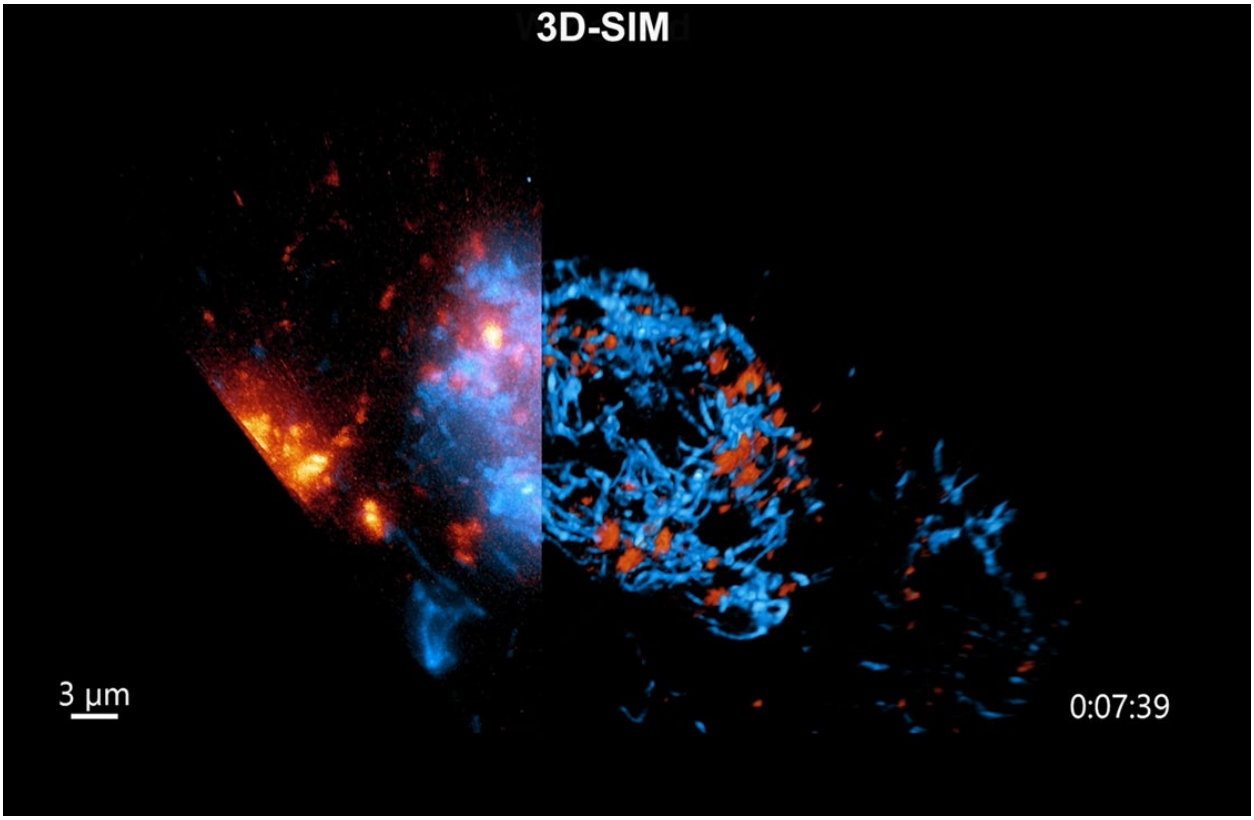

Movie S7. **Time-lapse 3D-SIM imaging of live hTERT-RPE1 cells.** Part A: Cells expressing mitochondria (COX8a-StayGold, cyan) and Golgi (β4Gal-HaloTag9-JFX549, yellow) markers imaged across a ~160x100x10 µm^3 volume for 156 time points at 56 sec intervals (~2.4 hrs). Part B: Faster and significantly longer 3D SIM imaging (1500 time points, 32 sec intervals, ~13 hours) enabled by denoising and the use of two rather than the customary three directions for the illumination patterns.

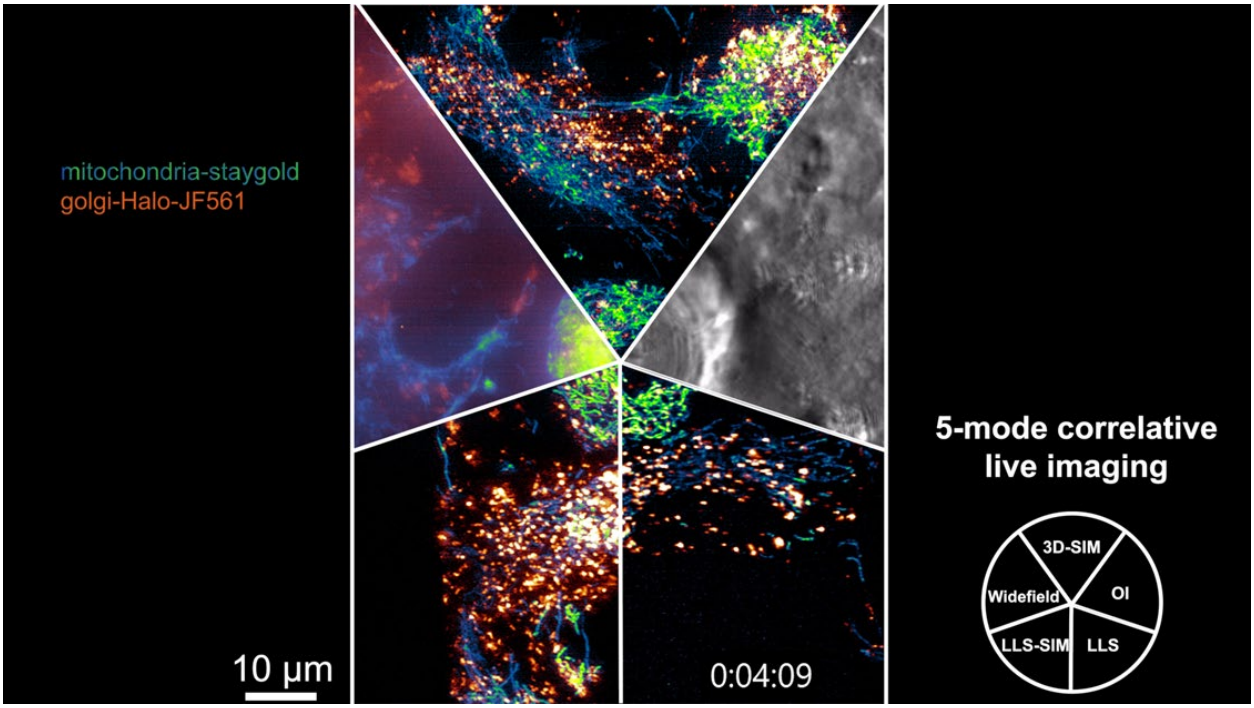

Movie S8. **Multi-modal correlative imaging of organelle dynamics during cell division.** A dividing hTERT-RPE1 cell expressing markers for mitochondria (COX8a-StayGold, green-blue) and Golgi (β4Gal-T1–HaloTag9-JFX549, orange) imaged by five distinct correlative techniques as shown. The movie cycles through widefield, 3D-SIM, oblique illumination (OI), lattice light sheet (LLS), and LLS-SIM views, offering complementary perspectives on organelle partitioning and cell morphology throughout mitosis.

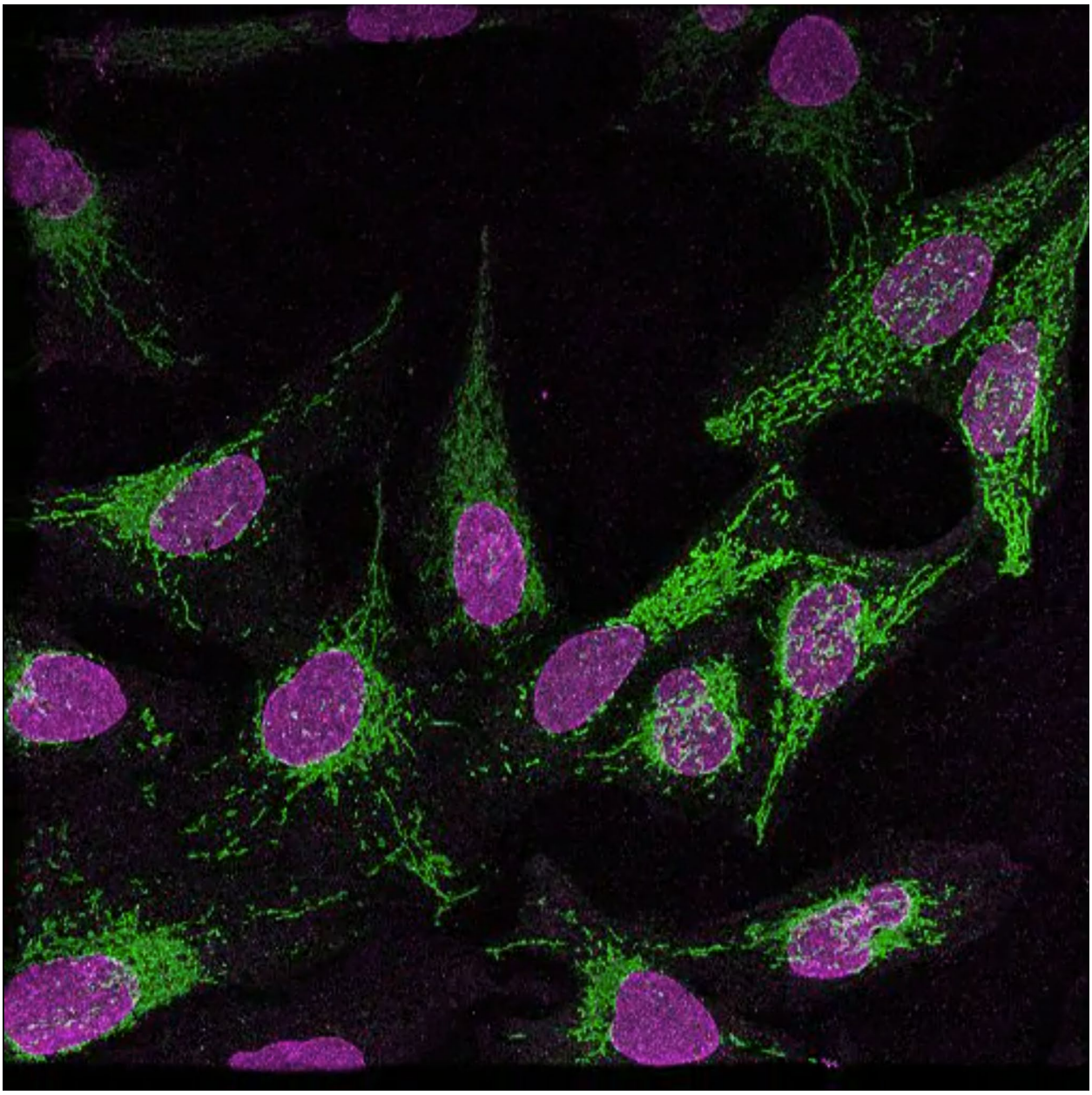

Movie S9. **Two-color 3D LLSM-PAINT imaging of cellular architecture.** Simultaneous imaging of the nuclear envelope (Lamin A/C, green) and mitochondrial outer membrane (TOMM20, magenta) over a 180 x 200 x 17 μm³ volume of cultured U2OS cells.

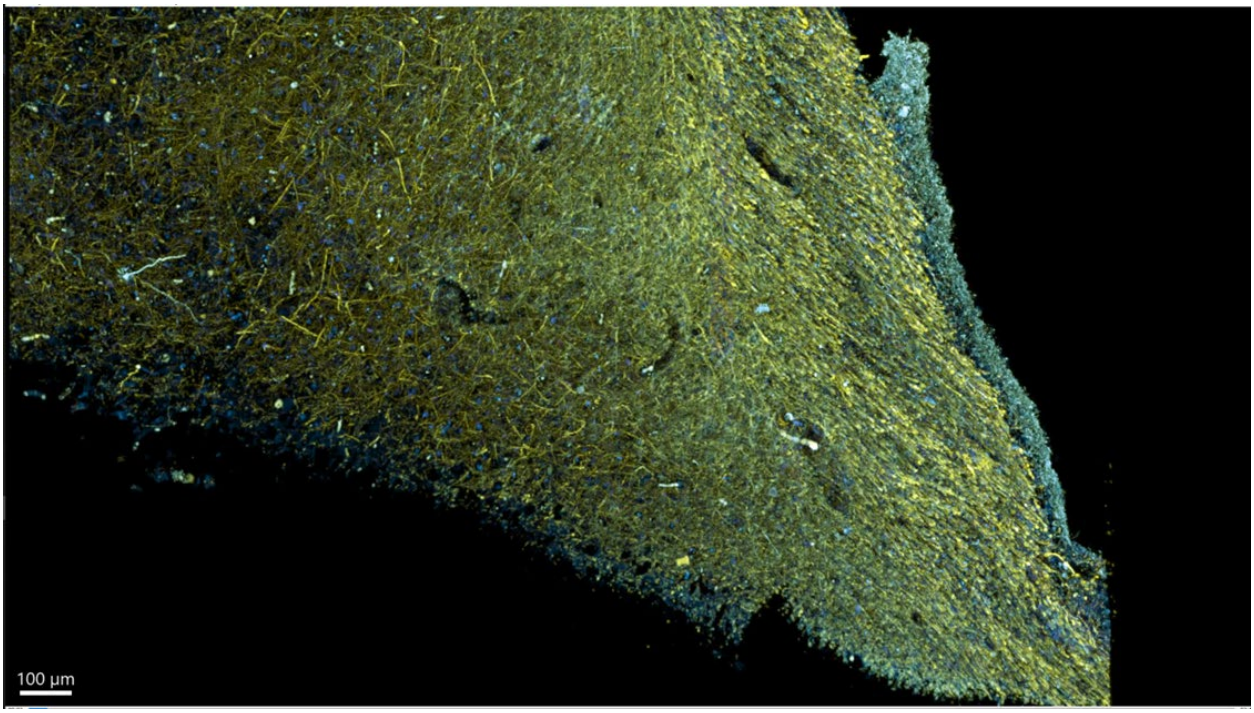

Movie S10. **ExLLSM volume rendering of human hippocampal tissue from an Alzheimer's disease donor.** Fly through within a ~2000 x 2375 x 98 µm^3 (pre-expansion) tissue section at 4x expansion. Immunostaining of axons (neurofilament200, cyan) and myelin sheaths (MBP, yellow) highlight structural abnormalities across the large volume.

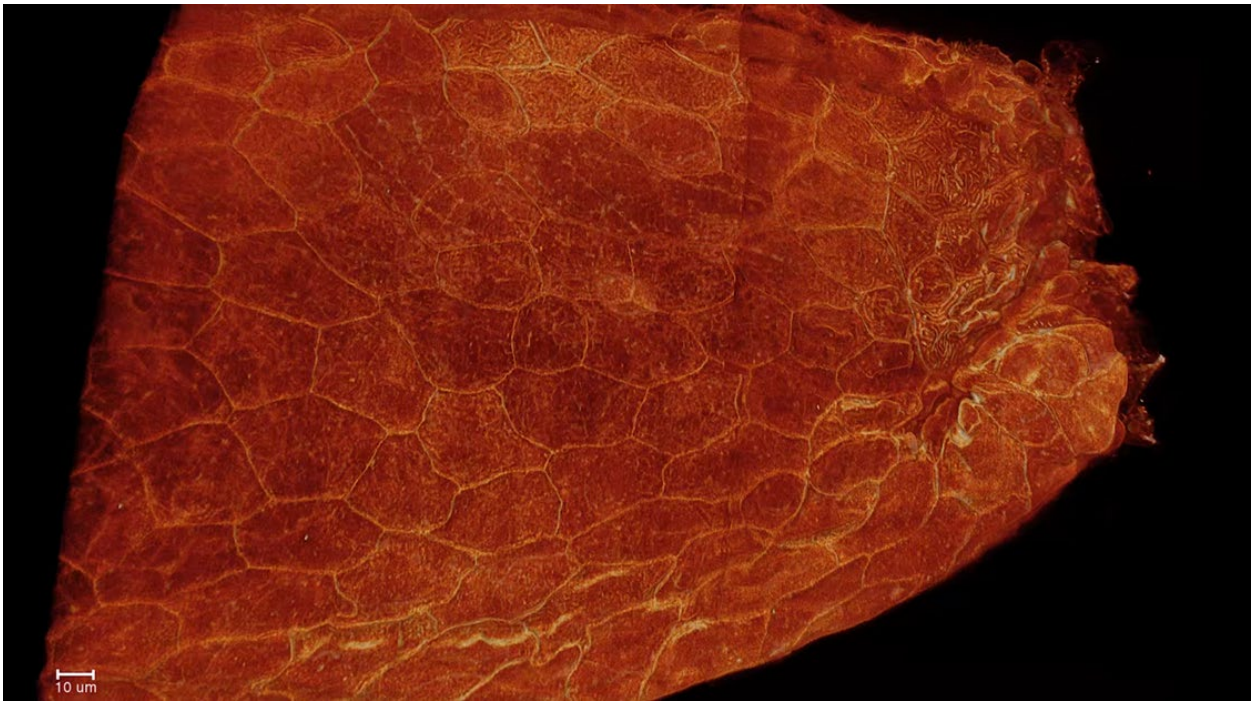

Movie S11. Long-term AO-LLSM imaging of zebrafish tail fin regeneration. Time-lapse imaging of a regenerating zebrafish tail fin, starting immediately post amputation, in a 48 hpf embryo. The movie spans 12.5 hours (250 time points at ~3 min intervals) and shows all plasma membranes (orange) and nuclei (cyan) within a 240 x 180 x 60 μm^3 volume stitched from 2 x 2 AO corrective tiles. The AO-corrected, denoised, and enhanced data reveal diverse behaviors at the cellular, subcellular, and tissue levels, including migration, cell division, cell fusion, microvesicle secretion, anchoring fibril dynamics, and both epidermal and vascular remodeling.

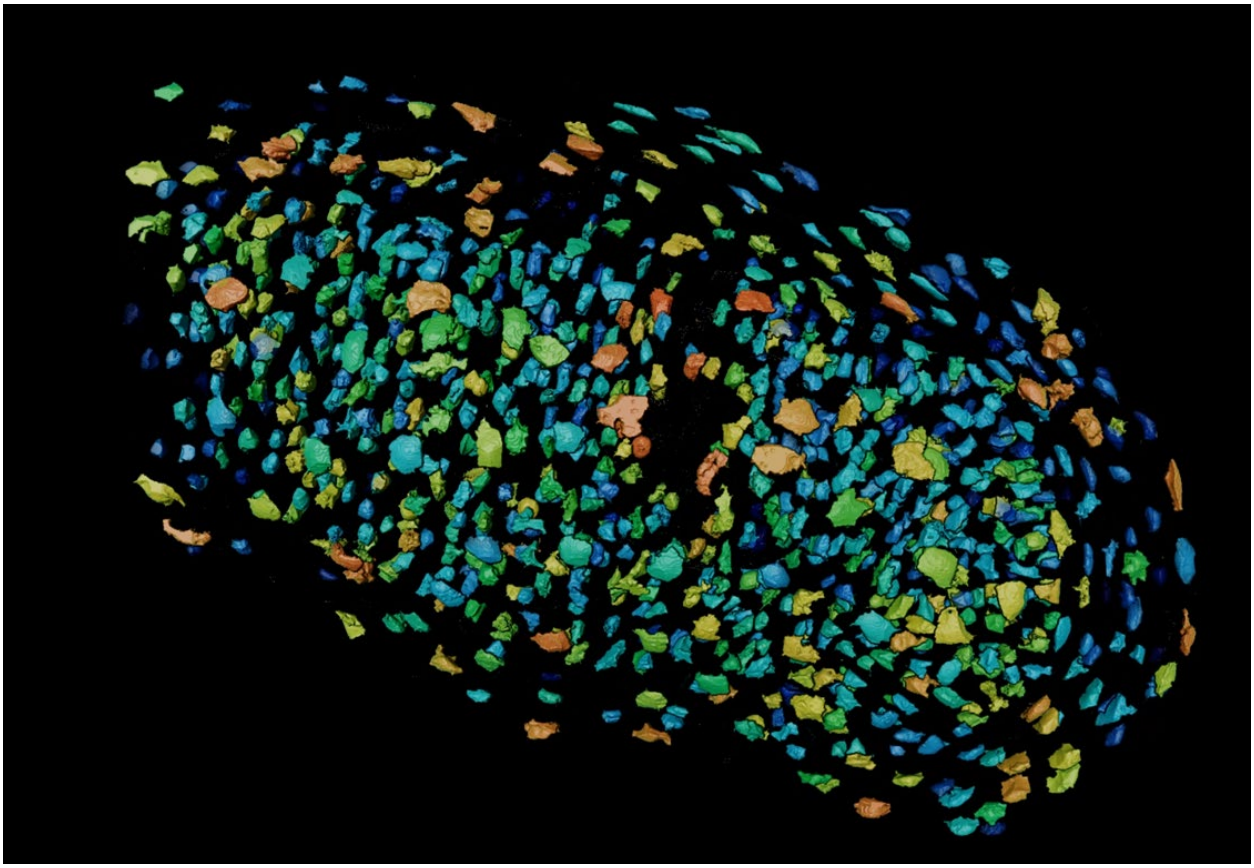

Movie S12. Cell cycle state across a zebrafish tailbud. AO-LLSM time-lapse imaging of an 18 hpf zebrafish tailbud expressing membrane, histone, and DHB/CDK activity biosensor markers. The cytoplasmic-to-nuclear ratio of the biosensor (low=G1/S, high=G2) indicates cell cycle state (as noted in Fig. 4e). In this example, the largest fraction of cells in G2 reside near the periphery. (blue/green=G1/S, yellow/red=G2).

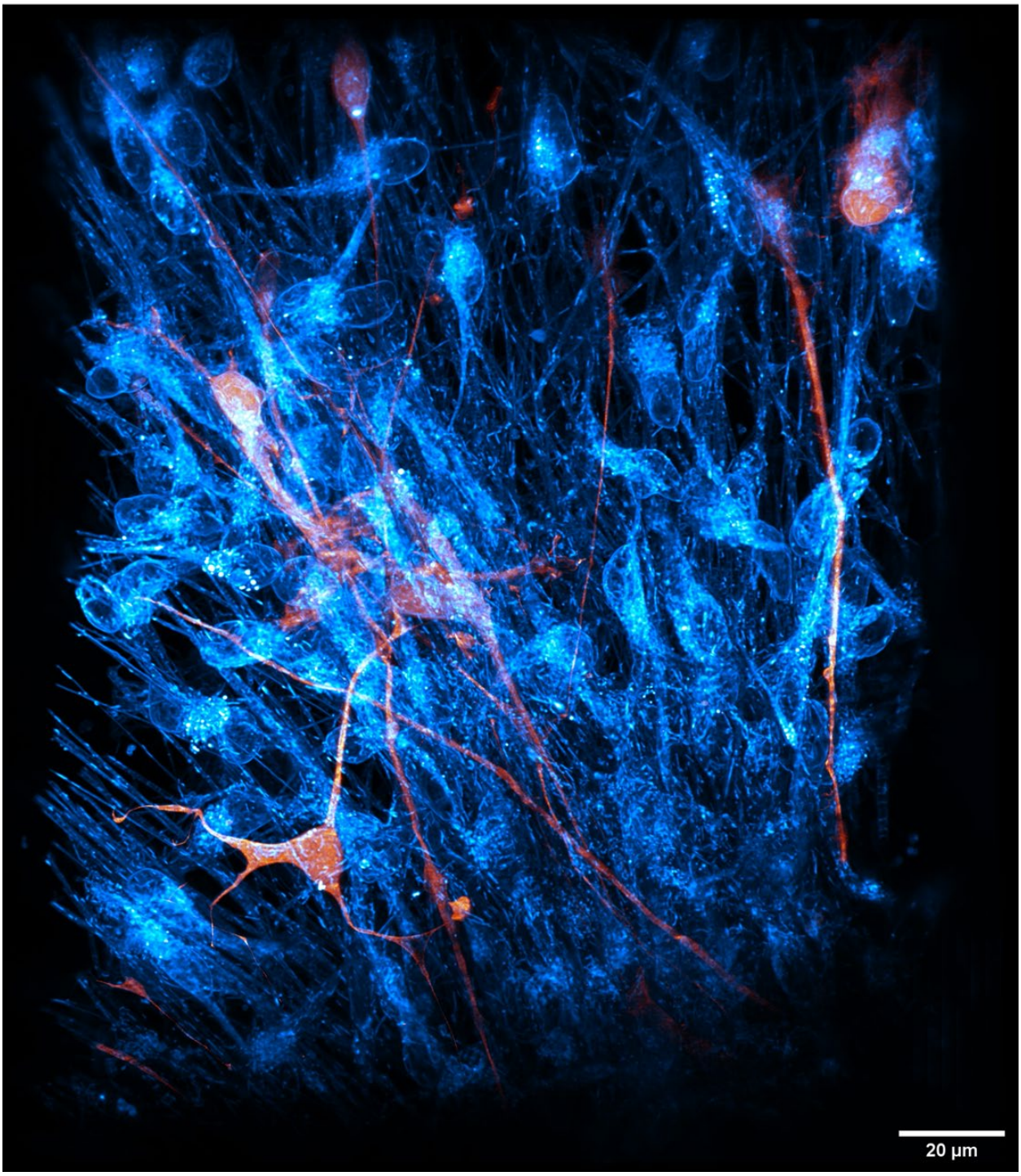

Movie S13. **Neuronal and mitochondrial dynamics in a human iPSC-derived brain organoid.** AOLLSM reveals mitochondial transport (Mitotracker, cyan) and neurite dynamics (sparse cytosolic mGFP, orange) in a living human brain organoid.

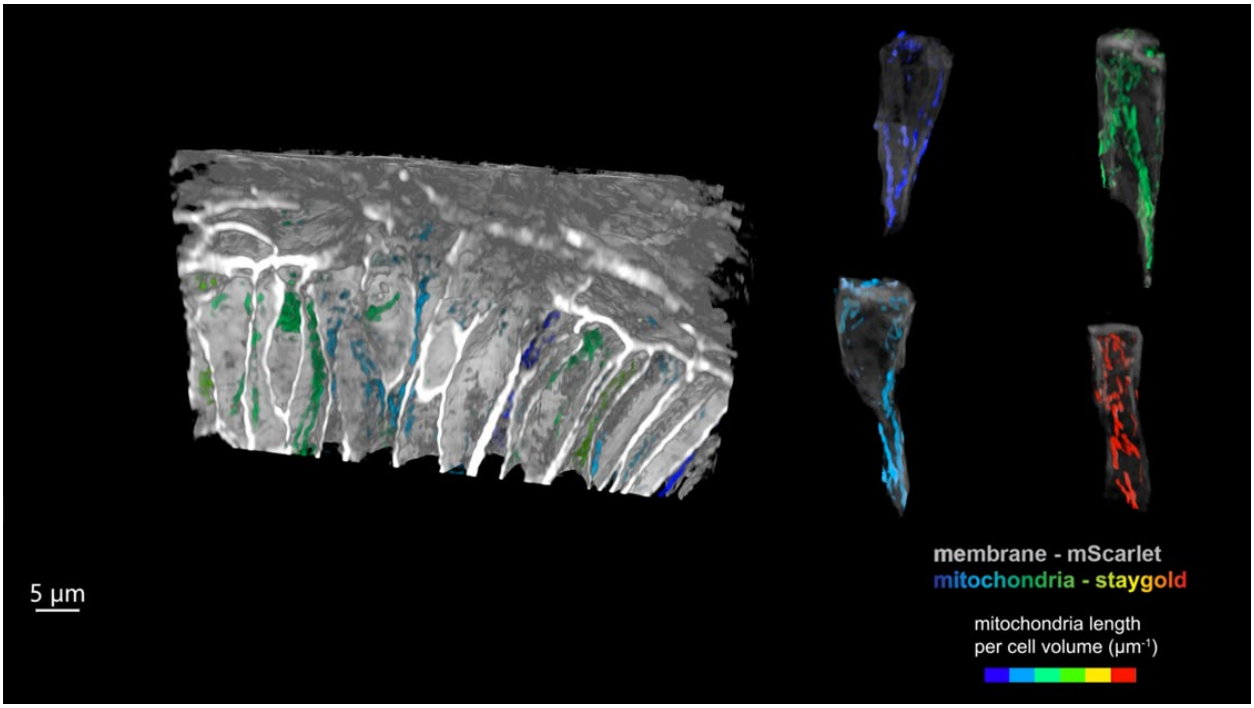

Movie S14. AO-LLS-SIM reveals mitochondrial morphologies and dynamics in the developing zebrafish. Imaging a 14 hpf zebrafish expressing mitochondrial (Cox8a-StayGold) and plasma membrane (Lynk-mChilada) markers. Part 1: A 61 x 57 x 40 µm^3 volume imaged without and with AO correction. Part 2: Dynamics of membrane (gray) and mitochondria (pseudocolor) over a 56 x 56 x 40 µm³ volume for 60 time points at 93 sec intervals.

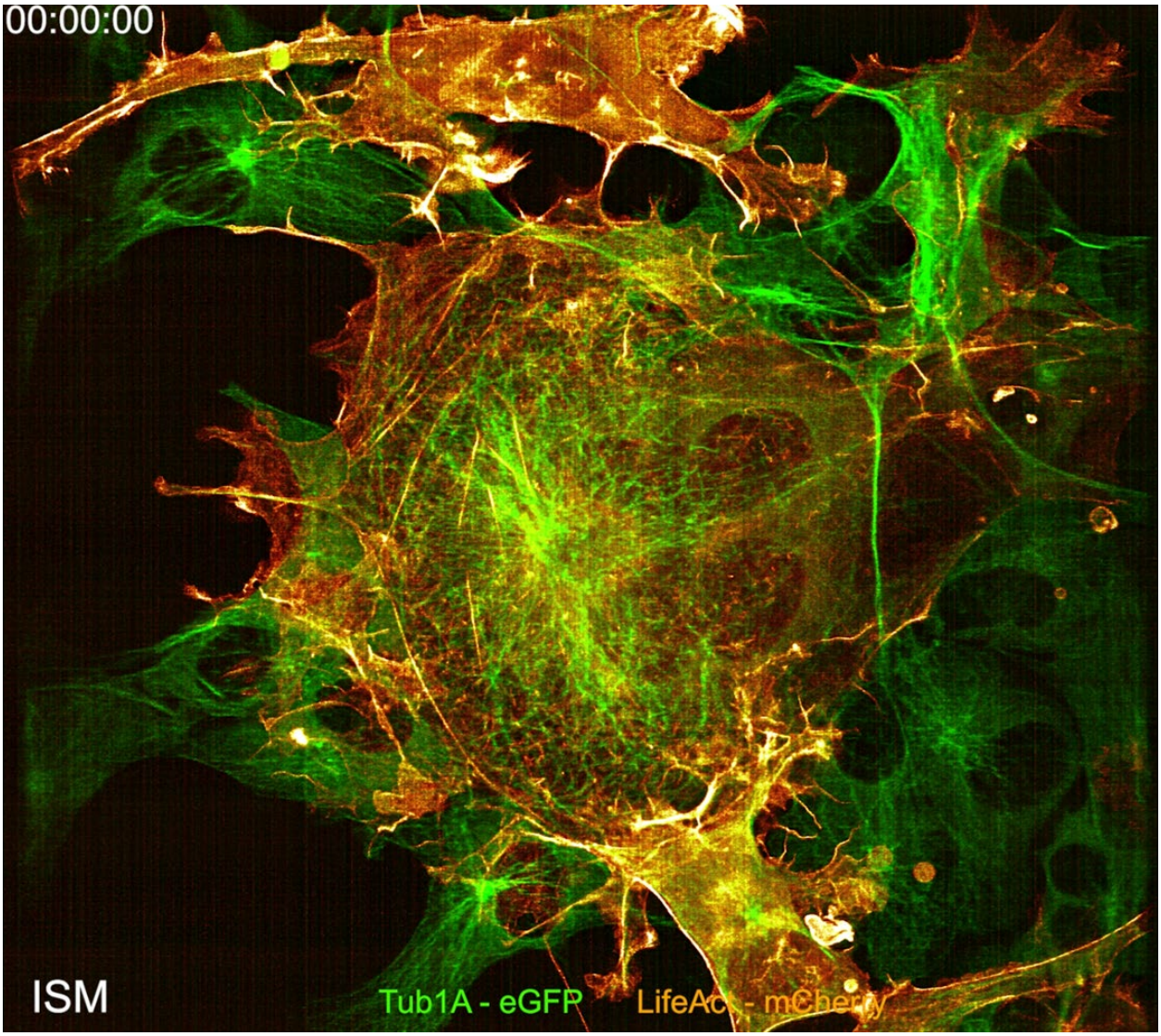

Movie S15. **Linescan ISM imaging of cytoskeletal dynamics in a COS 7 Cell.** Microtubules (Tub1A-eGFP) and F-actin (LifeAct-mCherry) for 9 frames at ~4 sec intervals.

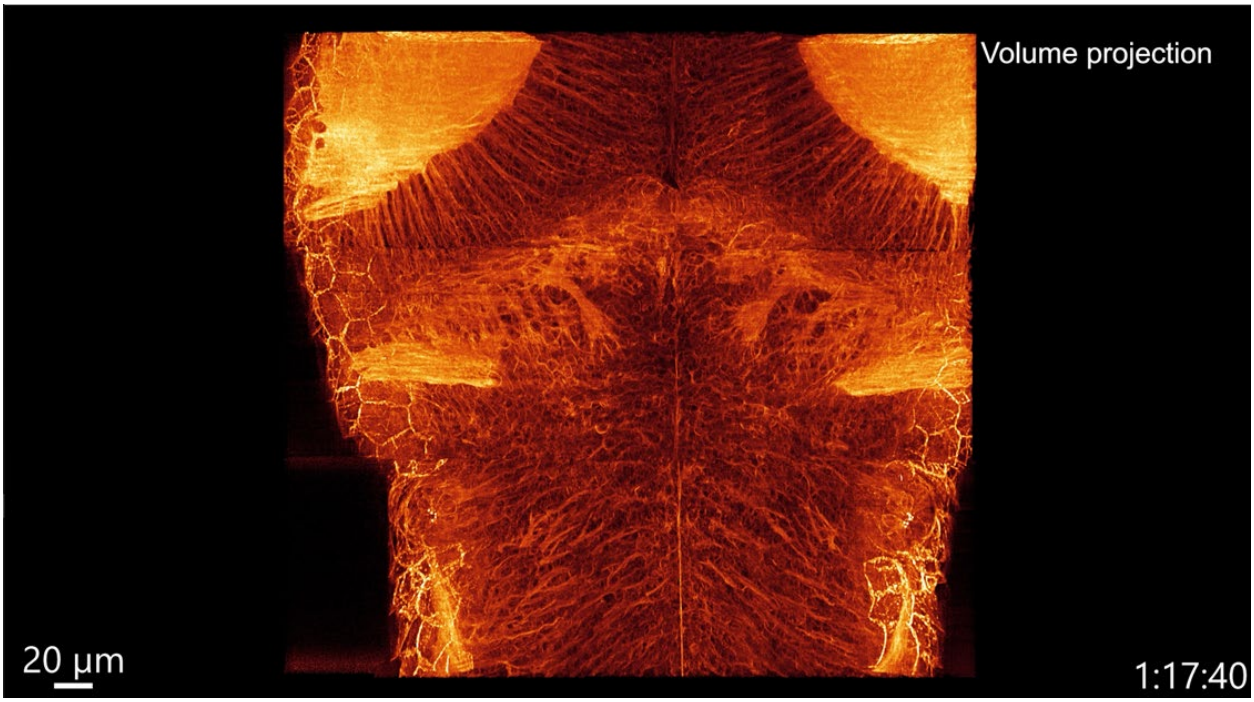

Movie S16. AO-ISM imaging of development in a 7 dpf membrane-labeled zebrafish. Part 1: Comparison with and without AO correction across a 336 x 319 x 84 μm^3 volume. Part 2: Time-lapse AO-ISM movies of development for 13 time points at 32 min intervals (~6.9 hrs total): i) xy MIP from an entire 354 x 332 x 16.3 μm^3 image volume; ii) successive xy MIPs from 0.5 µm thick slabs cut from this volume centered at z = 7, 10 and 13 µm, respectively. Part 3: Development of paired neuromast organs.

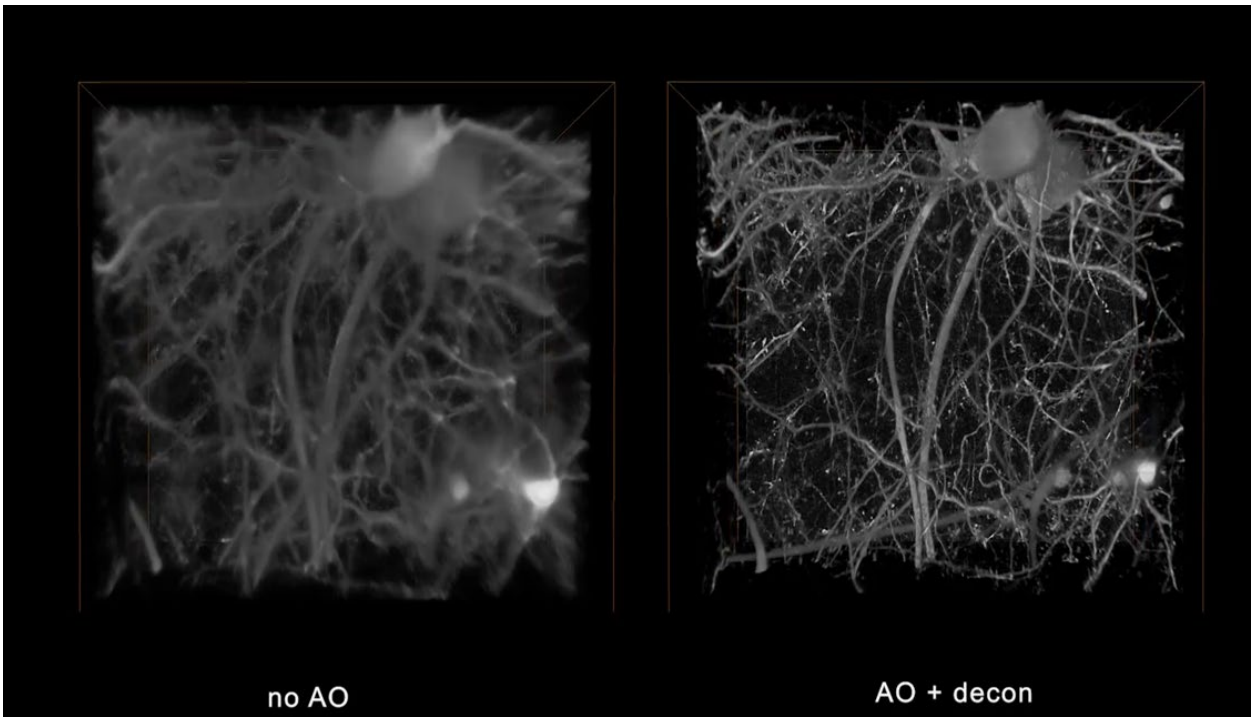

Movie S17. In vivo adaptive optical two photon microscopy of neuronal structure. Comparisons with and without AO throughout a 100 x 100 x 400 μm³ volume starting at a depth of 60 μm in the cortex of a Thy1-YFP-H mouse.

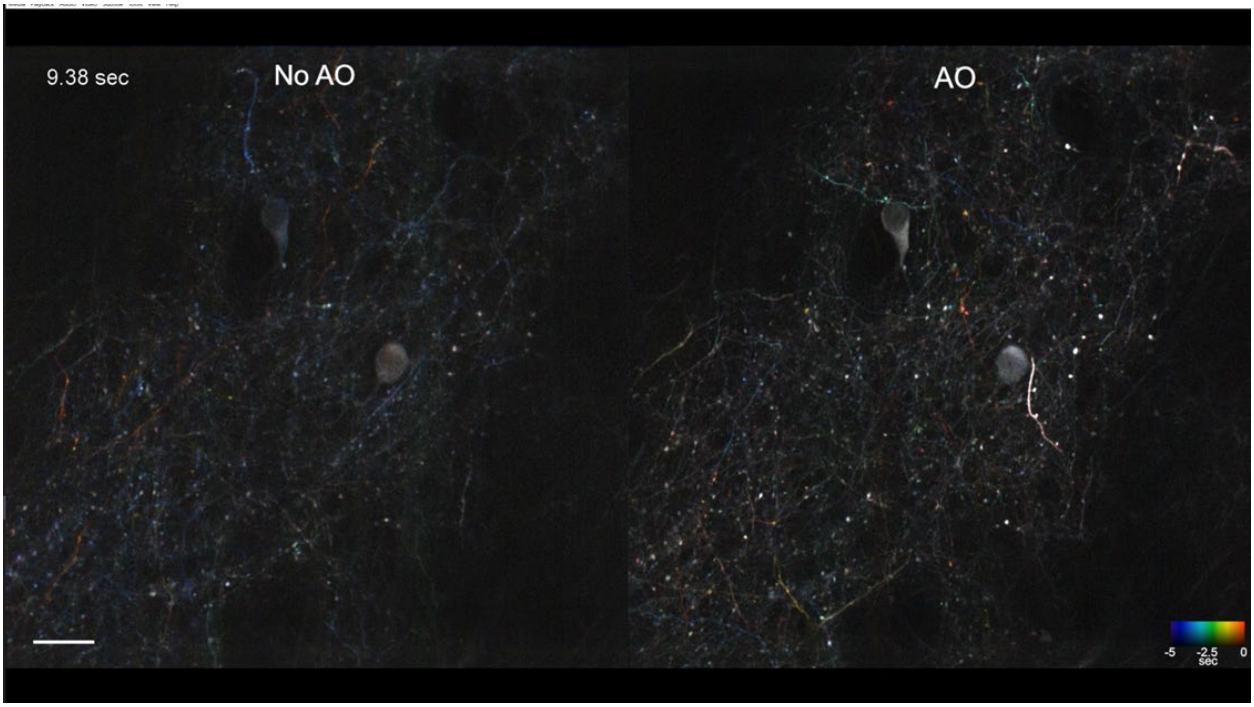

Movie S18. Functional imaging of calcium transients with and without AO correction in the mouse cortex. Two photon imaging of neural activity in a mouse expressing GCaMP7s. Most recent activity is coded by color.

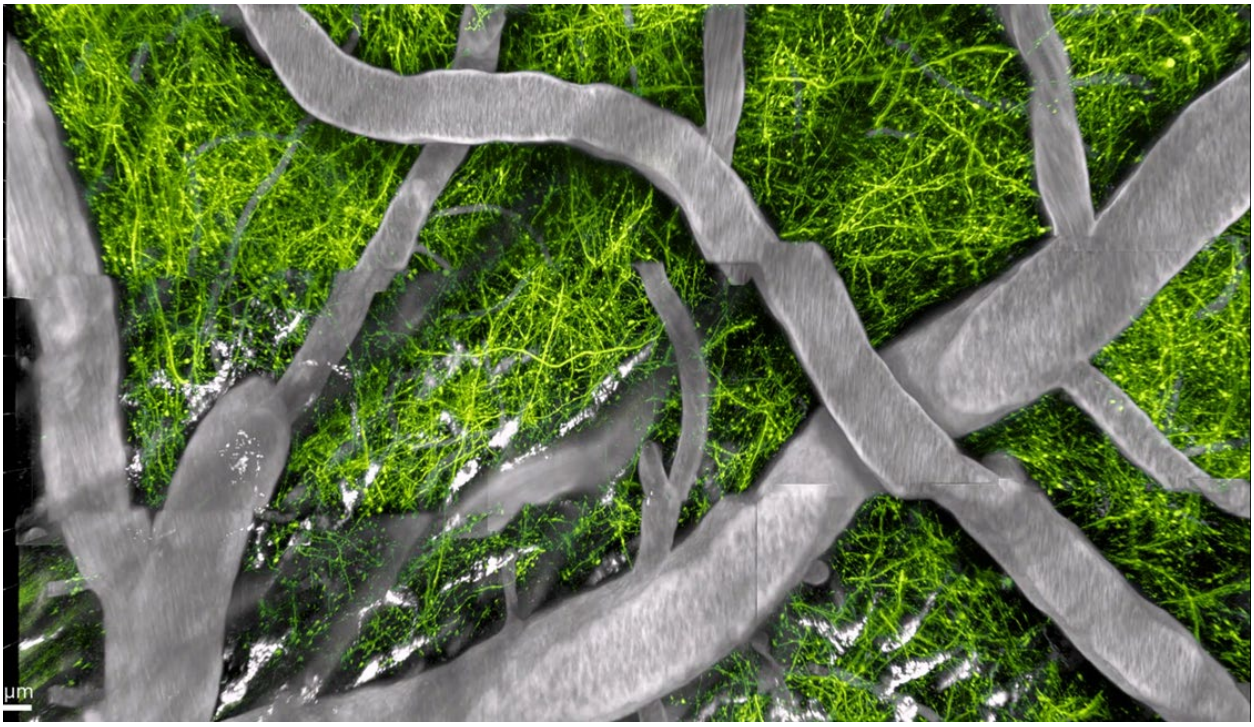

Movie S19. Tiled two-color AO-TPM resolves dendritic spines near vasculature *in vivo*. A 500 x 500 x 100 µm³ cortical volume in a live Thy1-YFP-H mouse, with vasculature labeled by Texas Red dextran (gray).

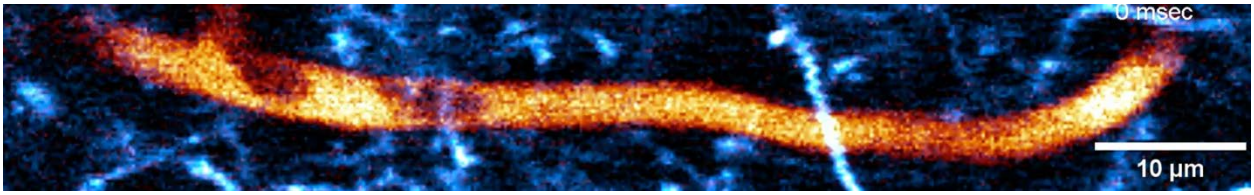

Movie S20. Two-color AO-TPM captures erythrocyte flow in capillaries at 250 Hz. A 83 x 12.8 µm^2 FOV in a live Thy1-YFP-H mouse, with the vasculature labeled with Texas Red dextran (orange), and the erythrocytes appear as negative (unstained) regions within the plasma.